Novel Intercalation Compounds of Molybdenum Diselenide

A Thesis

Submitted to the Graduate Faculty

In Partial Fulfillment of the Requirements

For the Degree of

Master of Science

In the Department of Chemistry

Faculty of Science

University of Prince Edward Island

© Hao Xu

Charlottetown, P.E.I.

May, 2008

Your file Votre référence
ISBN: 978-0-494-49856-9
Our file Notre référence
ISBN: 978-0-494-49856-9

SIGNATURE PAGES

ii-iii

REMOVED

Abstract:

Host-guest intercalation chemistry is an emerging research field with implications in the development of novel materials for a wide variety of real-world applications. As such, the intercalation chemistry of the two dimensional layered molybdenum diselenide ($MoSe_2$) has been explored. $MoSe_2$ has been intercalated with a variety of guest species such as solid polymer electrolytes, electronically conductive polymers, and small molecules. This was achieved by first treating the $MoSe_2$ with an excess of n-BuLi to form the lithiated phase of $MoSe_2$ ($Li_{0.7}MoSe_2$). The $Li_{0.7}MoSe_2$ exfoliates readily in water or N-methylformamide (NMF) to yield single layers of $MoSe_2$. Addition of solutions or suspensions of guest species to the single layers result in the formation of novel sandwiched compounds. These guest species include solid polymer electrolytes (SPE) such as poly(ethylene oxide) (PEO), poly(vinyl pyrrolidone) (PVP), methyl cellulose (MCel), poly[oxymethylene-(oxyethylene)] (POMOE), and poly[bis-(methoxyethoxyethoxy)phosphazene] (MEEP), electronically conductive polymers such as polyaniline (PANI), poly(N-methylaniline) (PMA), poly(2-ethylaniline) (PEA) and poly(2-propylaniline) (PPA), and small molecules such as glycine, ferrocene and 7,7,14,14-Tetramethyl-1,4,8,11-tetrazacyclotetradeca -4,11-dine (TTCD).

Analysis of the materials has been done by Powder X-ray Diffractometry (XRD), Fourier Transform Infra Red Spectroscopy (FTIR), Thermogravimetric Analysis (TGA), and Differential Scanning Calorimetry (DSC) where applicable. In the XRD spectra, the dramatic increase of the interlayer spacing values of the resulting

compounds suggest that all of the guest species mentioned above have been intercalated into the $MoSe_2$ layers. Thermal stabilities and stoichiometries of SPE/$MoSe_2$ were determined by TGA. The guest-host interactions of the polymer/$MoSe_2$ intercalates have been studied by FT-IR and DSC; the red shifts in the FT-IR spectra and the glass transition temperature (T_g) shifts of polymers in DSC reveal that the mechanical motions of the polymers were confined by the $MoSe_2$ layered host. In addition, the blue shifts in the FT-IR spectra suggest that redox reactions may occur between the guests and the host. Electronic conductivities were measured using the four-probe van der Pauw technique. Compared to the conductivity of 2H $MoSe_2$ the increase in conductivity of 'restacked $MoSe_2$' indicates the conversion from the semiconductor (2H form) to the conductor (1T form). Among the electronically conductive polymer/$MoSe_2$ intercalates, PMA/$MoSe_2$ intercalate showed better results in conductivities compared to PANI/$MoSe_2$, PEA/$MoSe_2$, and PPA/$MoSe_2$ intercalates. Ionic conductivities of MEEP, $(MEEP)_4LiCF_3SO_3$ and $(MEEP)_4LiCF_3SO_3$/$MoSe_2$ intercalate were investigated through alternating current (AC) impedance spectroscopy.

Acknowledgements

I would like to thank Dr. Rabin Bissessur, my supervisor, for providing me a platform in his lab to do this master's research in materials chemistry and to show people that I am also a piece of useful and friendly 'material'.

I should express thanks for other faculty members in my supervisory committee: Dr. Brian Wagner, Dr. Robert Haines and Dr. Michael Shaver. I learnt a lot from them on how to figure out the problems in the research.

I really appreciate Dr. Nola Etkin that she taught me a lot of knowledge closely related to my research. Dr. Douglas Dahn's hands-on work for my research and tutoring me in interpreting my data really deserve a great acknowledgement from me. I should also acknowledge Dr. Barry Linkletter who permitted me to sit in his class to have a good review in biochemistry and a good practice in listening of academic English.

My special gratefulness should be expressed to Mrs. Dawna Lund, Mrs. Sharon Martin and Miss Jill MacDonald. Dawna Lund not only taught me a lot on the instruments but also friendly reminded me to work safely and efficiently in the lab. I cannot forget that in a key part of my research, Jill MacDonald gave me a hand on the indicators. Sharon Martin's efficient work really helped me a lot daily. Their positive attitude for work really impressed me.

All of my classmates and lab mates either form Dr. Bissessur's group or from other Faculty's group should also be acknowledged by me. Without their unselfish

help, my research would not have gone so smoothly. I will never ever forget the friendship we have built in the last two years and a half.

In the end, I should not forget to thank Canada which is a great country. Her great credit is a key reason why she is so attractive for those who are from overseas.

Table of Contents

List of Abbreviations

AC	Alternating Current
DSC	Differential Scanning Calorimetry
FT-IR	Fourier Transform Infra Red
LiOTf	lithium triflate ($LiCF_3SO_3$)
MCel	methyl cellulose
MEEP	poly[bis-methoxyethoxyethoxy)phosphazene]
NMF	N-methylformamide
NMR	Nuclear Magnetic Resonance
PANI	poly(aniline)
PEA	poly(2-ethylaniline)
PEG	poly(ethylene glycol)
PEO	poly(ethylene oxide)
PMA	poly(N-methylaniline)
POMOE	poly[oxymethylene-(oxyethylene)]
PPA	poly(2-propylaniline)
PVP	poly(vinyl pyrrolidone)
SPE	solid polymer electrolyte
$\mathbf{T_f}$	freezing temperature
$\mathbf{T_g}$	glass transition temperature
TGA	Thermogravimetric Analysis
$\mathbf{T_m}$	melting temperature
THF	Tetrahydrofuran
TTCD	7,7,14,14-Tetramethyl-1,4,8,11-tetrazacyclotetradeca-4,11-diene
XRD	X-ray Diffractometry

List of Figures

List of Tables

List of Equations

Chapter 1: Introduction

1.1 Intercalation Chemistry

In chemistry, "intercalation" is the process of embedding a guest species (G) into a host lattice (H), yielding a product which is generally nonstoichiometric.[1] The reaction equation may be delineated as: [2]

$$x\,G + \square_x[H] \rightarrow G_x[H] \qquad 1.1$$

Compared with conventional solid state reactions, an intercalation reaction is carried out at, or close to, room temperature. The result is that the main structural characteristics of the host are maintained as well as main physical properties of the host material. This is a key difference between the products of an intercalation reaction and the non-stoichiometric phases coming from high temperature reactions. The latter often present a structural change of the host lattice, which is supposed to reach a stable state thermodynamically.[1]

In solid state intercalation chemistry, there are three types of host materials: 3-D framework hosts with a vacancy extending in three dimensions inside the lattice, 2-D layered hosts with a two dimensional free space between the host layers, and 1-D chain hosts which are one dimensional tubes.[1] 3-D framework hosts include some transition metal oxides/chalcogenides such as ReO_3 and Mo_6S_8.[3-6] 2-D layered hosts contain some transition metal oxides, chalcogenides and oxy-halides such as MoO_3,[7-8] TiS_2 [9-10] and FeOCl.[11] In addition, phosphate-based materials such as $VOPO_4$[12] and phosphorous trichalcogenides such as $MgPS_3$[13-14] are also 2-D layered hosts. 1-D

chain hosts include some transition metal trichalcogenides/trihalides, such as TiS_3[10] and $RuBr_3$.[15] All of the host structures mentioned above have a strongly covalently bonded network of atoms with unoccupied lattice sites for accommodating guest species. Empty, low-lying electronic states should be available in the host structures, so that electrons can be transferred from the guest species.[1]

Compared with two-dimensional layered structures, three-dimensional and one-dimensional host materials have many disadvantages. 3-D framework structures may limit the size and prevent the movements of guest species, because the net structure extends in three dimensions along with the free space, while 1-D chain structures are typically unstable[1] due to the angles of the bonds within the 1-D structural matrix and their higher internal energy. However, the 2-D layered structures are more stable than 1-D structures and are much more flexible than 3-D frameworks due to the two-dimensional vacant lattice sites connected by the low-energy pathway between the layers.[1] Therefore, many more guest species can be inserted into the 2-D layered structures.[16, 17]

Among the 2-D layered structures, transition metal oxides and chalcogenides are studied intensively and extensively. Numerous compounds such as simple monoatomic cationic species, molecular ions, neutral molecules and polymers can be inserted into the transition metal chalcogenides/oxides.[1, 18]

1.2 Applications of intercalation chemistry

1.2.1 Lithium ion battery

One of the most important applications of the intercalation chemistry of transition metal oxidies/chalcogenides is as lithium ion battery materials. The basic structure of a lithium ion battery is depicted in Figure 1.1. There are four functional components in lithium ion batteries: the cathode, the anode, the electrolyte, and the lithium salt. During the charging cycle, the anode is negatively charged by the external electrical power and the lithium ions are driven out from the cathode. The lithium ions then travel through the electrolyte to the anode, which serves to maintain charge balance. During the discharge cycle, the electrons flow through an external circuit from the anode to the cathode and do work to a load (electrical apparatus). To balance the negative charges in the cathode, the lithium ions flow through the electrolytes and are inserted into the layered cathode.[19]

Figure 1.1 Charge and recharge mechanism of a Lithium Ion Battery[19]

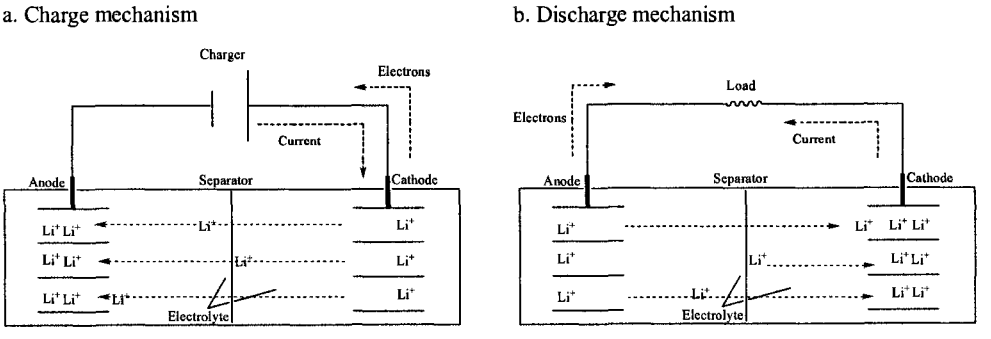

1.2.1.1 Cathode Materials

Layered transition metal chalcogenides/oxides and their intercalates can be used for cathode materials. The key requirements for cathode materials are as follows:[20] The cathode material should have an easily reducible/oxidizable component, so that the reaction between the cathode and lithium is reversible, with a high free energy change and rapid kinetics for insertion and removal of lithium ions. At the same time, the material should not degrade during the discharging and charging cycle. In addition, low cost and low toxic materials should be good candidates for cathode materials. For example, layered structures such as $LiTiS_2$, $LiVSe_2$, $LiCoO_2$, $LiNiO_2$, and $LiNi_yMn_yCo_{1-2y}O_2$ have been used as cathode materials.[20] However, the motivation for reducing environmental hazards and cutting down the expensive cost of materials, as well as the request for high power density batteries make the exploration of new cathode materials an active field of research.

When electronically conductive polymers are positively doped and inserted into layered structures, hybrid cathode materials are created (Figure 1.2). These hybrid materials inherit the advantages arising from both the layered structure and the polymer and create new opportunities in battery material research.[21-24] For example, the redox ability of the polymer can basically increase the charge capacity of the layered structures. The other benefit is that the polymers will create pillars between the pristine layers and helps to transport lithium ions between the layers.[21] An example of such a hybrid material is depicted in Figure 1.2.

Figure 1.2 Schematic representation of PANI/MoS_2 hybrid cathode material [22]

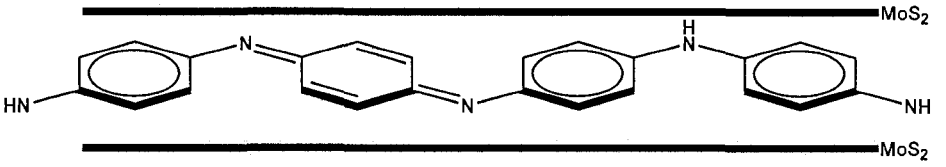

Electronically conductive polymers such as poly(aniline), poly(pyrrole) and poly(nitroxylstyrene) by themselves have also been shown to be viable cathode materials based on their reversible redox behaviour.[25-27] To be electronically conductive, a polymer must behave like a metal or semiconductor, *i.e.* its electrons should be free to move. The first requirement for this is that the polymer contains conjugated double bonds.[28] The typical structures of such conjugated polymers are illustrated in Figure 1.3.

Figure 1.3 Typical structures of conjugated polymers [25, 29]

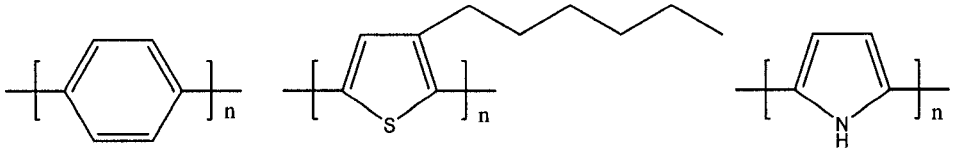

(1) poly-(para-phenylene) (2) poly(3-hexythiophene) (3) poly(pyrrole)

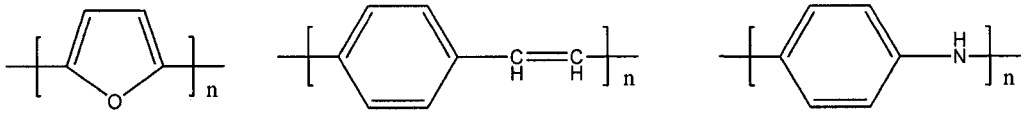

(4) poly(furan) (5) poly(phenylenevinylene) (6) poly(aniline)

However, it is not enough for a polymer to just possess conjugated double bonds. To become electronically conductive, the polymer has to be doped, either by removal or addition of electrons to the material.[28] For example, electronic conductivity of

polyaniline increases 10^{13} fold after doping and the doped form has a conductivity of 10^3 S/cm.[25] Based on the work of 'rediscovering' those conjugated polymers, Alan MacDiarmid, Alan Heeger and Hideki Shirakawa shared the Nobel Prize in chemistry in the year 2000.

The reason why doping can increase the electronic conductivity can be explained by using band theory. In band theory, a simple diatomic molecule (H_2) is considered to originate from two identical atoms which have only one electron available for bonding. The same energy level of these two electrons in the atoms will split into two new molecular levels: the bonding level and the antibonding level after the formation of a bond. The bonding level is occupied by the two electrons and the antibonding level is empty. (Figure 1.4) If electrons are excited by sufficient energy either from heat or light, they will undergo a transition to the antibonding level. In the medium-sized molecules, the formation of the bond obeys the same principle. When more bonds are built, more bonding levels will stack together and so will the antibonding levels. If the molecule surpasses a certain size, the bonding orbitals will be closer to each other until a continuous band appears, which is called the valence band. The antibonding orbitals follow the same principle and form the antibonding band which is also called the conduction band. When the polymer is doped (either negatively doped or positively doped) new electronic energy levels within the band gap will be formed (Figure 1.5 a). These electronic energy levels are called polarons. The polaron energy levels are lower than the energy level of the conduction band but higher than that of the valence band. Moderate doping (more electrons are added or

removed) will form bipolarons (Figure1.5 b) and heavy doping will build bipolaron bands within the band gap. (Figure1.5 c) These energy bands in the band gap can permit electrons to bounce into the conduction band quite easily, creating conduction pathways.[30]

Figure 1.4 Form of CB, VB and Band Gap by the Band Theory [30]

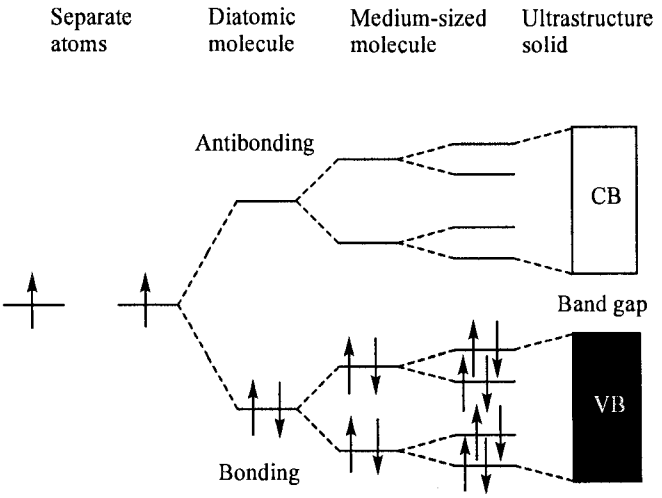

Figure 1.5 Evolution of band structure upon doping [31]

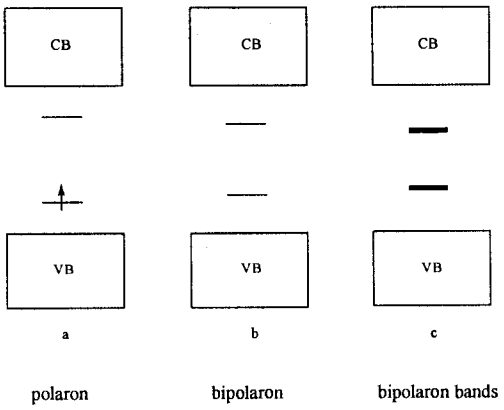

1.2.1.2 Anode Materials

Layered graphite has been used as an anode material for many years due its low cost and low toxicity.[19] Negatively doped poly(nitroxylstyrene) has also been proven to be a good candidate for an anode material due to its "lightweight, tunable redox property, mechanical flexibility, and processing compatibility".[26] 2-D layered structures inserted by n-doped polymers might be another possibility. Most recently, silicon nanowires have been shown to be excellent anode materials for lithium batteries due to their multiple advantages, such as low discharge potential, flat discharge curve and the highest known theoretical charge capacity (4,200 mAh g^{-1}).[32-35] These nanowires are directly planted on the current collector, so that each nanowire is connected with the current collector and efficient 1-D electron transport is achieved. Compared with silicon films or silicon particles which have been explored before, silicon nanowires are more durable. The diameter and length of the nanowires can easily increase and decrease without the sample breaking during many charging and discharging cycles.[32]

1.2.1.3 Electrolyte Materials

Recently, electrolyte materials based on polymers have been a major focus of research due to the many advantages that they can offer, such as high ionic conduction, good electronic insulation, environmental friendliness, mechanical, thermal, and electrochemical stability.[36, 37]

The ionic conduction of a polymer electrolyte is based on the "segmental motion"

of the polymer chain.[37] Segmental motion can be explained in the following way. Lithium salts can be dissolved in the polymer electrolyte which works as a solid solvent.[30] There are some electron donor coordination sites in these polymers and these sites can be weakly linked to the lithium cations, *i.e.* these polymers effectively solvate the lithium ions and separate them from their counterpart (the anions). The delocalized lithium ions work as good charge carriers. When polymers experience thermally activated motions such as bending, twisting, and creeping, the lithium ions will have the opportunity to transfer from a coordination site on one polymer chain to a similar site on another chain (Figure 1.6).[30] To guarantee that the lithium ions are sufficiently mobile to migrate readily toward the appropriate electrode, the polymers must be sufficiently flexible and provide enough 'free volume' to allow the ions to move. In fact, this requires the polymers have "a low glass transition temperature and a low degree of crystallinity".[30] The structures of some solid polymer electrolytes (SPE) are illustrated in Figure 1.7 below.

Figure 1.6 Ion transport via segmental motion [37]

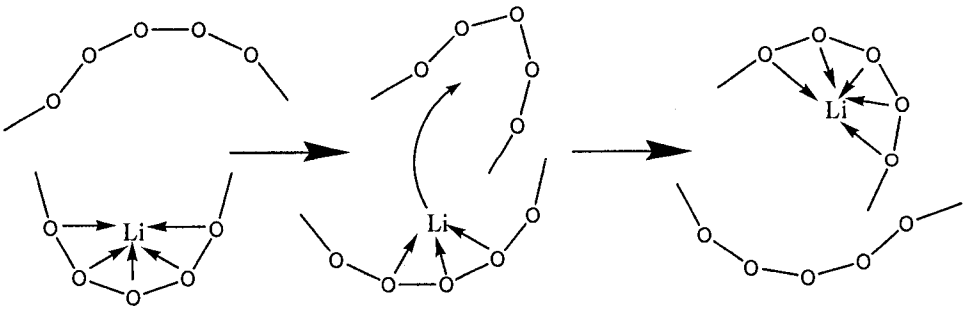

Figure 1.7 Structures of typical ionically conductive polymers [38]

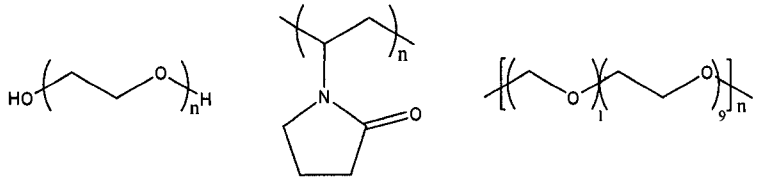

poly(ethylene glycol) (PEG)

poly(vinylpyrrolidone) (PVP)

poly[oxymethylene-(oxyethylene)] (POMOE)

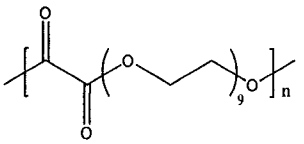

poly[oligo(ethylene glycol)-oxalate] (POEGO)

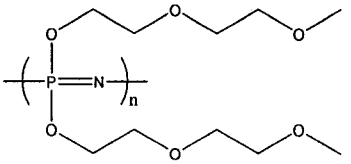

poly[bis-(methoxyethoxyethoxy)phosphazene] (MEEP)

Lithium triflate (LiOTf), which contains bulky anions, is often used as the salt in solid polymer electrolytes due to its low crystal energy. Were this not the case, the lithium cations and anions would not be able to be separated and would remain as ion-pairs, and there would not be sufficient charge carriers (free Li^+) in the system. Along with the increase of the salt concentration, the ionic conductivity will reach a maximum. However, after the peak it starts to decrease due to the large number of "transient crosslinks" formed by the polymer and the ions.[30]

Poly(ethylene glycol), PEG, has been studied intensively as an electrolyte material. However the crystallized component of the polymer is a hinderance for ionic conductivity due to reduced mechanical freedom of polymeric chains.[30, 37] Therefore, two approaches have been created to solve this problem. One is to synthesize highly amorphous polymers such as poly[oxymethylene-(oxyethylene)] (POMOE),[39] poly[oligo(ethyleneglycol)-oxalate] (POEGO) ,[40] and

poly[bis-(methoxyethoxyethoxy)phosphazene] (MEEP).[41] However, these amorphous polymer electrolytes are mechanically unstable, and create leaking problems when assembled in a cell.[42]

The other approach is to produce composite electrolytes. Different methods have been tried, including addition of fine ceramic powders to the polymers to increase mechanical stability.[43] Intercalation of polymers into layered structures may also be a useful method. The early research on polymer electrolyte/layered structure nanocomposites was focused on the PEG system, such as PEG/MoO_3,[44] PEG/TaS_2,[45] PEG/TiS_2,[46] PEG/$NbSe_2$,[47] and PEG/WS_2.[48] These two dimensional layered hosts can suppress the tendency of the polymer to crystallize. Therefore, the ionic conductivity of the resulting material can be improved, in principle.[44] Recently, POMOE, POEGO and MEEP (Figure 1.8) have been also inserted into layered structures.[37, 49-52] These polymers are amorphous, and so they are able to transfer lithium ions very efficiently by "segmental motion".[37] On the other hand, their mechanical stability can be improved when they are entrapped by a layered host.[51]

Figure 1.8 Schematic representation of the lamellar arrangement of $(MEEP)_{0.33}MoS_2$. Reprinted from reference 51 with the author's permission.

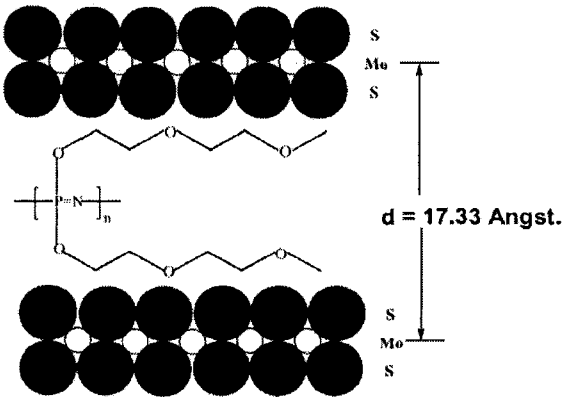

1.2.2 Other applications of intercalation chemistry

1.2.2.1 HDS Catalyst

The catalytic hydrodesulfurization (HDS) of petroleum has been studied for half a century. Pristine MoS_2 and $MoSe_2$ can be used as HDS catalysts.[53] Currently, MoS_2 supported by Cp_2Co^+ in different proportions has shown good catalytic activity for the hydrodesulfurization of thiophene. In this study the electronic structure of the MoS_2 layer was changed by intercalation, and HDS activity was changed by the altered electronic state. Compared with unsupported MoS_2, a greater dispersion, which has a direct impact on reaction rates, has been achieved in the supported catalysts. In fact, the number of active sites has a close relationship with the surface area of MoS_2. The Cp_2Co^+ supported MoS_2 has a much larger surface area than pristine MoS_2, and the activity is increased four-fold, with the maximum activity near a Co/(Co-Mo) ratio of 0.4.[54]

1.2.2.2 Smoke for Military Purpose.

The intercalation of MoS_2 with organic molecules that decompose thermodynamically to release gas for hiding military objects has been explored by D'Anne Emmett Spence at University of Maryland. Based on the function of imbibing electromagnetic waves, smoke made of MoS_2 can prevent military objects from being detected by radar. However, interparticle adhesive forces along the C axis of the anisotropic MoS_2 are strong enough to cause the dispersed MoS_2 particles to restack quickly and disable the function. Insertion of organic compounds into the MoS_2 layered structure will decrease the cohesion forces between the MoS_2 layers and help the MoS_2 particles to fully spread out. For this purpose guest species such as ethyl diazoacetate (EDA), diethyl oxalate (DEO) and meldrum's acid (MA) have been inserted into MoS_2.[55]

1.3 Current research on $MoSe_2$

$MoSe_2$ (molybdenum diselenide) is a layered transition metal dichalcogenide. The two-dimensional sheets are held together by van der Waals interactions.[56] There are several structural differences between the transition metal chalcogenides and oxides, which may cause the physical differences between them. The increased covalency of the chalcogenide atoms will assist transition metal valence (d) orbitals to be involved in covalent bonding. Therefore, the formal charge on the metal centre is reduced, and there is a trendency for forming metal-metal bonds. In addition, the polarizability of the chalcogenide anion (X^{2-}) is higher than that of O^{2-} which helps to build structures

with highly asymmetric X, *i.e.* the geometric limitation can be reduced. The result of these factors is that more low-dimensional structures are found among the chalcogenides than the corresponding oxides and transition metal chalcogenide hosts present a larger scope of intercalation chemistry.[1]

$MoSe_2$ layered structure will undergo a structural change from 2H-type to 1T-type when it is intercalated by lithium due to an electron transfer from lithium to molybdenum.[56-60] The structures of 2H and 1T $MoSe_2$ are illustrated in Figure 1.9[59] and Figure 1.10.[58] 2H-$MoSe_2$ showing semiconductor behavior is hexagonally packed with molybdenum coordinated to six selenium atoms in a trigonal prismatic geometry (D_{3h}).[60] 2H stands for the two Se-Mo-Se molecular layers per unit cell with a hexagonal symmetry.[61] 1T-$MoSe_2$ exhibits metallic behavior because there is no band gap between the valence band and the conduction band.[55, 60] The designation 1T means that there is one $MoSe_2$ layer per unit cell and the layer forms a two-dimensional array of trigonal symmetry (O_h)[56]. The molybdenum is bonded to the selenium in an octahedral geometry.

Figure 1.19 structure of 2H(D_{3h}) and 1T(O_h) $MoSe_2$ (side view)[59]

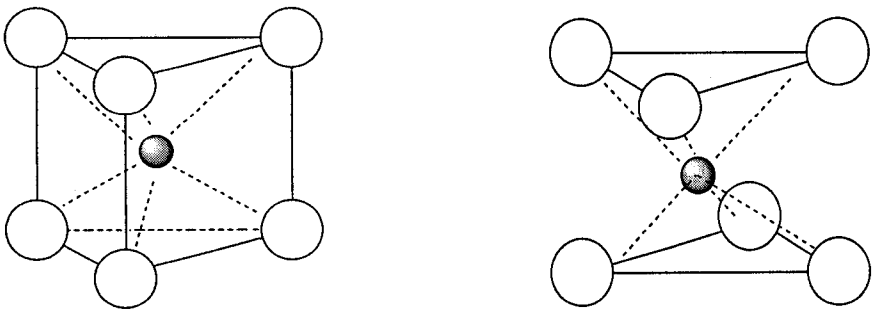

2H type 1T type

Figure 1.10 structure of 2H(D_{3h}) and 1T(O_h) $MoSe_2$ (top view).[55-60]

Reprinted from reference 58 with the author's permission.

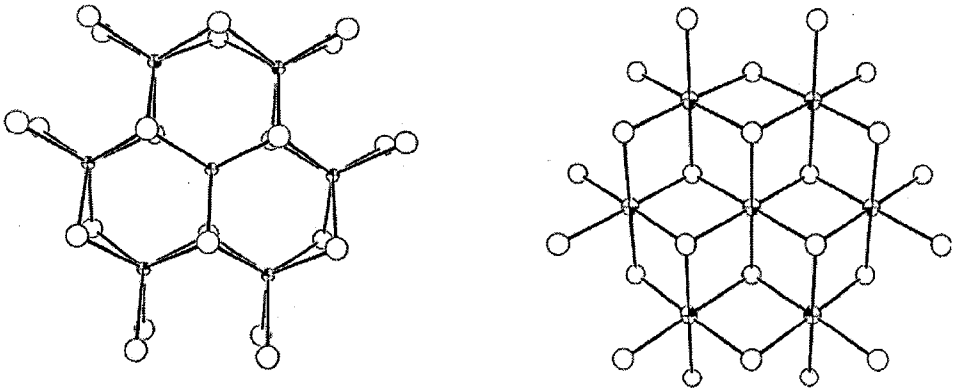

2H type 1T type

Similar to MoS_2, $MoSe_2$ is not able to accommodate large guest molecules due to its low electron affinity.[55-56, 60] However, 2H-$MoSe_2$ reacts with *n*-butyl lithium, which is a strong reducing agent, to achieve a stoichometric product, $LiMoSe_2$,[60] according to Equation 1.2. The d-orbital of molybdenum will accommodate the extra electron coming from *n*-BuLi and the oxidation state is reduced from Mo^{+4} (d^2) to Mo^{+3} (d^3).[55-56, 60] The density of states diagram for $MoSe_2$ (Figure 1.11) should be very similar to that of MoS_2, in principle.[55-57, 59-60] This diagram shows the structural conversion from 2H to 1T form of $MoSe_2$ caused by the addition of one electron. Due to the large band gap of 2H-$MoSe_2$, orbital energy will augment dramatically by adopting one extra electron, creating instability in the trigonal prismatic coordination geometry. However, addition of the electron only causes a slight increase in electronic energy in the 1T polymorph. Therefore, with a d^3 electronic configuration the 1T-form is far more stable than the 2H-form. This is the reason why the structure

change from 2H to 1T occurs.[55] The 1T-$MoSe_2$ will undergo an exfoliation and restacking reaction during which the intercalation of large molecules can be realized, and $MoSe_2$ will remain in the octahedral geometry until the intercalate experiences heating, aging or contacts an oxidation agent.[55-56]

$$MoSe_2 + n\text{-BuLi} \rightarrow LiMoSe_2 + \tfrac{1}{2} C_4H_{10} + \tfrac{1}{2} C_4H_8 \qquad 1.2\ ^{60}$$

Figure 1.11 Comparison of density of states diagram for (a) 2H-$MoSe_2$ and (b) 1T-$MoSe_2$ [55-57, 59]

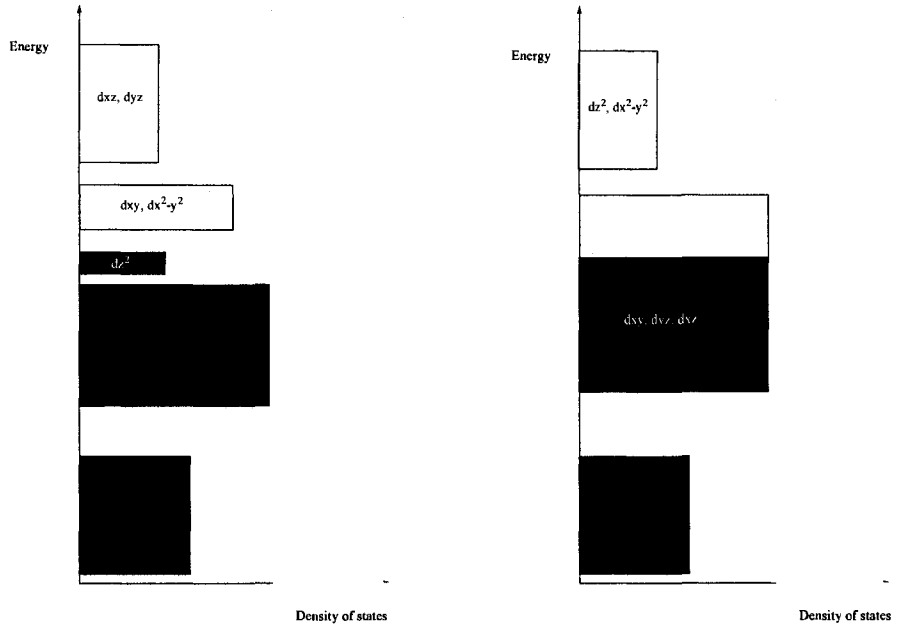

(a) 2H form (b) 1T form

Even though 2H-$MoSe_2$ has the same coordination as 2H-MoS_2, and both of them transfer from 2H to 1T type when the same reducing agents are applied, there are still some differences between the two systems. For example, the van der Waals gap of $MoSe_2$ (3.22 Å) is relatively wider than that of MoS_2 (2.96 Å) due to the fact that

lone-pair repulsion between selenium atoms across the van der Waals gap is stronger than that between sulfur atoms.[62] The molybdenum dichalcogenides are semiconductors with indirect band gaps. The indirect band gaps of MoS_2, $MoSe_2$, and $MoTe_2$ are 1.29 eV, 1.10 eV and 1.00 eV, respectively.[63] The decrease in band gap from MoS_2 to $MoTe_2$ might be due to the trend of metal-metal bond formation.[1] Compared to the extensive intercalation chemistry reported for the MoS_2 system, much less work has been done for the $MoSe_2$ system.[57, 64-65]

1.4 Project goals

The main goal of this project is to explore the exfoliation and restacking properties of $MoSe_2$. This will be achieved by first treating pristine $MoSe_2$ which is in the 2H form with an excess of n-BuLi to form the lithiated phase of $MoSe_2$ (Li_xMoSe_2).

By making use of the exfoliation and restacking properties of Li_xMoSe_2, a series of sandwiched compounds will be prepared. The guest species that will be inserted into $MoSe_2$ in this project will consist of solid polymer electrolytes (SPE) such as PEG, PVP, methyl cellulose, POMOE and MEEP; electronically conductive polymers such as polyaniline and substituted polyanilines; and small molecules such as glycine, ferrocene and 7,7,14,14-Tetramethyl-1,4,8,11-tetrazacyclotetradeca-4,11-diene (TTCD). SPE/$MoSe_2$ sandwiched compounds are prepared in hopes that they will possess good ionic conductivity and improved mechanical stability. Thereafter, they could be choices for electrolyte materials for lithium ion batteries. Electronically conductive polymer/$MoSe_2$ intercalates may possess good electronic conductivity,

large charge capacity and may increase free mobility of lithium ions between the layers. Therefore, they could be used as cathode materials in lithium ion batteries. Small molecule/$MoSe_2$ sandwiched hybrids might have good electronic conductivity and catalytic activity, so that they could be utilized as electrode materials or HDS catalysts in the future.

XRD will be used to confirm if the guest species are inserted into the $MoSe_2$ layers. TGA will be used to determine the stoichiometric ratio between the host and guest, as well as the thermal stabilities of the resulting intercalates.

The host-guest interactions, which have close relationships with the ionic conductivity and the electronic conductivity of the intercalates, can be explored by FT-IR and DSC. The stability of the 1T 'restacked $MoSe_2$' can also be measured by DSC.

The ionic conductivity data are generated by using AC impedance spectroscopy and the electronic conductivities are acquired by the four-probe van der Pauw method.

Based on the differences between $MoSe_2$ and MoS_2, $MoSe_2$ intercalates may be superior to those of MoS_2 intercalates. For example, the smaller band gap of $MoSe_2$[63] may result in higher conductivity and the heavier 'Se' atoms may hinder the "glide motion" [55] from 1T to 2H-type so that the metallic (1T) form of $MoSe_2$[55-57] is more stable. It is hoped that materials with improved properties will be generated.

Chapter 2: $MoSe_2$

Compared with other layered systems, much less work has been done for the $MoSe_2$ system in terms of exploring its intercalation chemistry. Due to its low electron affinity $MoSe_2$ can not be intercalated with big molecules such as polymers.[55-57] However, lithium ions can be inserted into the $MoSe_2$ layered structure.[57, 60] By exploring the exfoliation and restacking properties of Li_xMoSe_2, potentially large molecules such as polymers could be inserted into the layered structure. In addition, it is worthwhile to study the stability of the 1T form of $MoSe_2$ that could affect the conductivity of the $MoSe_2$ intercalates prepared and discussed in the later chapters.

2.0 Materials

Molybdenum (IV) selenide (99.9 % Mo) was purchased from Strem and used as received without any further purification. n-Butyllithium (2.5 M solution in hexane) was purchased from Aldrich.

2.1 Experimental:

2.1.1 Lithiation of $MoSe_2$

Molybdenum (IV) selenide (1.3 grams, 5 mmol) was transferred into a 50 mL Erlenmeyer flask in a dry box. n-Butyllithium (6.5 mL, 16 mmol) was then introduced *via* a syringe into the flask. The reaction mixture was allowed to stir at room temperature in the dry box for 12 days. The product (Li_xMoSe_2) was filtered in the dry box and washed

with pentane. It was then stored in the dry box for future use.

2.1.2 Exfoliation and restacking of Li_xMoSe_2

Li_xMoSe_2 (300 mg) was removed from the dry box. Deionized water (30 mL) was added, resulting in the immediate formation of a black suspension. The suspension was sonicated for 2 hours to ensure complete exfoliation of the $MoSe_2$. It was then stirred at room temperature for 24 hours. A thin film of the sample was then cast on a glass substrate for XRD analysis. This was performed by pipeting some of the sample onto a glass slide and allowing for the evaporation of the solvent. The rest of the product was purified by centrifugation. Part of the purified $MoSe_2$ was cast on another glass substrate for XRD analysis. The rest of the product was freeze-dried for 24 hours for DSC and FT-IR characterization.

In a similar experiment, hydrochloric acid was introduced into the reaction system. Li_xMoSe_2 (300 mg) was removed from the dry box. Deionized water (30 mL) was added to the Li_xMoSe_2, resulting in the immediate formation of black suspension. The suspension was sonicated for 2 hours to ensure complete exfoliation of the $MoSe_2$. It was then stirred at room temperature for 16 hours. Hydrochloric acid (12M, 1.35 mL) was added to the $MoSe_2$ suspension (dropwise) to assist in restacking of the exfoliated $MoSe_2$ single layers. The reaction system was stirred for another 8 hours. A thin film of the sample was then cast on a glass substrate for XRD analysis. The rest of the product was purified by centrifugation. Part of the purified $MoSe_2$ was cast on another glass substrate for XRD analyses.

2.1.3 Titration of Li_xMoSe_2 with standard HCl

Li_xMoSe_2 (945 mg) was transferred to a 500 mL beaker and removed from the dry box. Deionized water (300 mL) was then added to the beaker. The mixture was sonicated using an ultrasonic probe (30% amplitude) for 1.5 hours. The suspension of $MoSe_2$ was filtered. Part of the $MoSe_2$ residue was cast as a thin film on a glass plate and dried in the fume hood for XRD analysis. The filtrate, which was a transparent solution, was concentrated by using a rotary evaporator. The filtrate was titrated with 0.10 M HCl to a phenolphthalein endpoint. After the titration the $MoSe_2$ residue was transferred into the filtrate. The mixture was sonicated for 1 hour, no pink colour was observed. However, after 12 hours it turned from transparent to a pink colour, and titration with 0.10 M HCl was continued until the endpoint. The titration experiment was run twice by using two similar samples of Li_xMoSe_2.

2.2 Results and Discussions:

2.2.1 $MoSe_2$

The properties of the pristine $MoSe_2$ need to be explored, and the results can be compared with that of the later synthesized guest/$MoSe_2$ sandwiched compounds.

Powder X-ray diffraction (XRD) was run on a Bruker AXS D8 Advance instrument equipped with a graphite monochromator, variable divergence slit, variable antiscatter slit and a scintillation detector. Cu (Kα) radiation (λ=1.524 Å) was used and the data collection was carried out at room temperature. Samples were prepared as thin films on a glass substrate or silicon substrate. The powder pattern of pristine $MoSe_2$ is shown in

Figure 2.1. The different peaks result from different planes in the $MoSe_2$ crystal structure. The interlayer spacing of $MoSe_2$ is 6.42 Å measured from the peak at the lowest angle in the XRD spectrum. From the powder pattern (Figure 2.1), the average crystallite size of $MoSe_2$ was calculated to be 370 Å as determined by making use of the Scherrer equation: [66]

$$\mathbf{D = K \times \lambda \times 57.3 / \beta^{1/2} \times \cos\theta} \qquad 2.1$$

In the Scherrer equation, D is the average crystallite size in Å, λ is the wavelength of the Cu (Kα) radiation (λ=1.524 Å), $\beta^{1/2}$ is the peak width at half-height in degrees and θ is the position of the peak in degrees. K is a constant depending on the shape of the crystallites. Assuming that the crystallites are perfect spheres, K is assigned a value of 0.9. The constant 57.3, is the conversion factor from radians to degrees.

Figure 2.1 XRD spectrum of $MoSe_2$

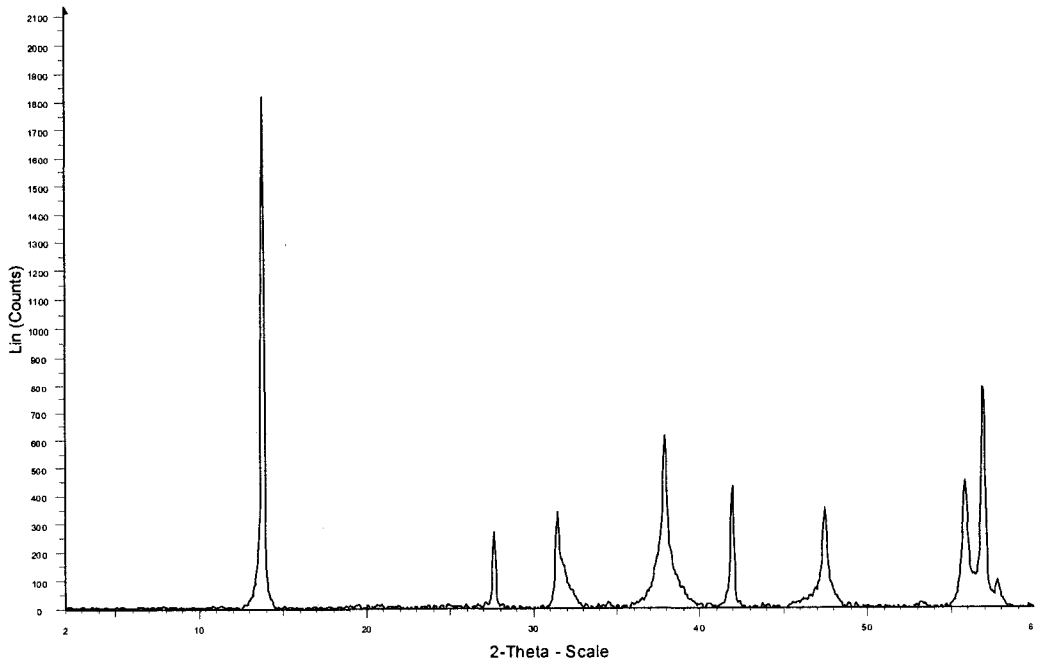

Thermogravimetric Analysis (TGA) was run on a TA 500 instrument in dry air or nitrogen purge using a heating rate of 10 °C/min.

The TGA of pristine $MoSe_2$ (in air) is shown in Figure 2.2. The aerial decomposition temperature of pristine $MoSe_2$ occurs at about 372 °C. From room temperature up to 580 °C, the weight percent loss was 42.85% and there was 57.15% by weight of the sample remaining. The observed plateau starting at 580 °C indicates that the resulting product is air-stable. The ratio of the molar mass of MoO_3 to that of $MoSe_2$ is 56.70% which is close to the weight% of the sample remaining as observed by TGA in air. The XRD of the resulting product from TGA in air (Figure 2.3) is very close to that of pure MoO_3 (Figure 2.4). From the TGA data, it can be concluded that at 580 °C $MoSe_2$ has been oxidised to MoO_3, with defects in the lattice structure accounting for variance in the two spectra.

Figure 2.2 TGA of $MoSe_2$ (in air)

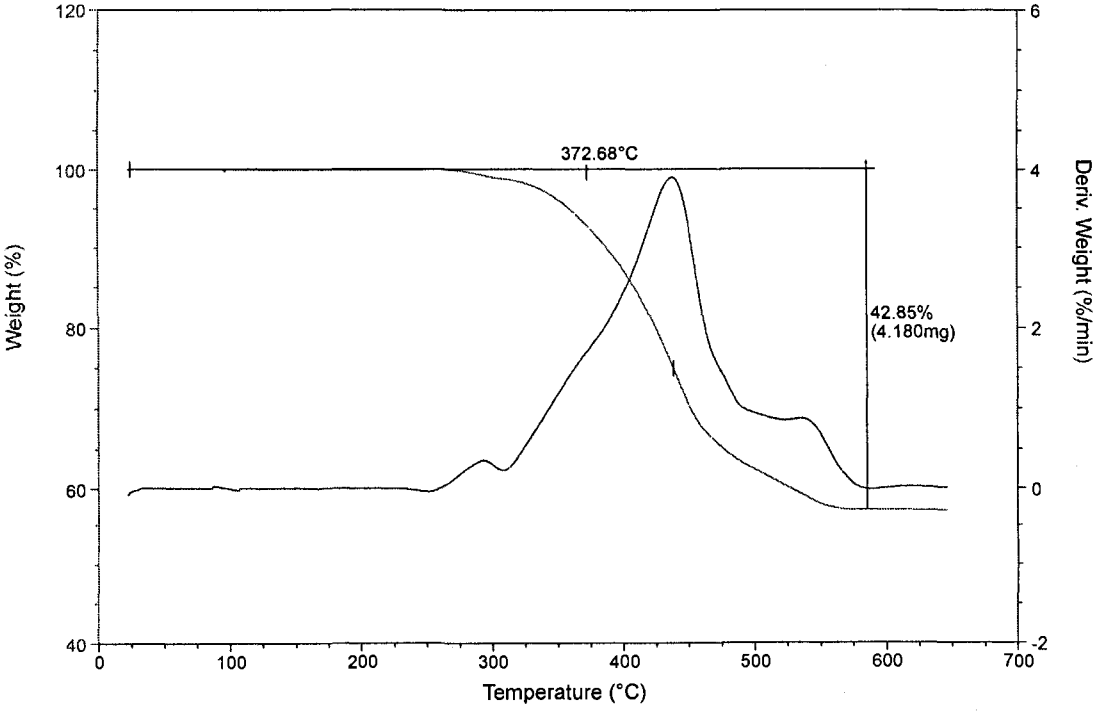

Figure 2.3 XRD spectrum of $MoSe_2$ after TGA (in air) up to 650 °C

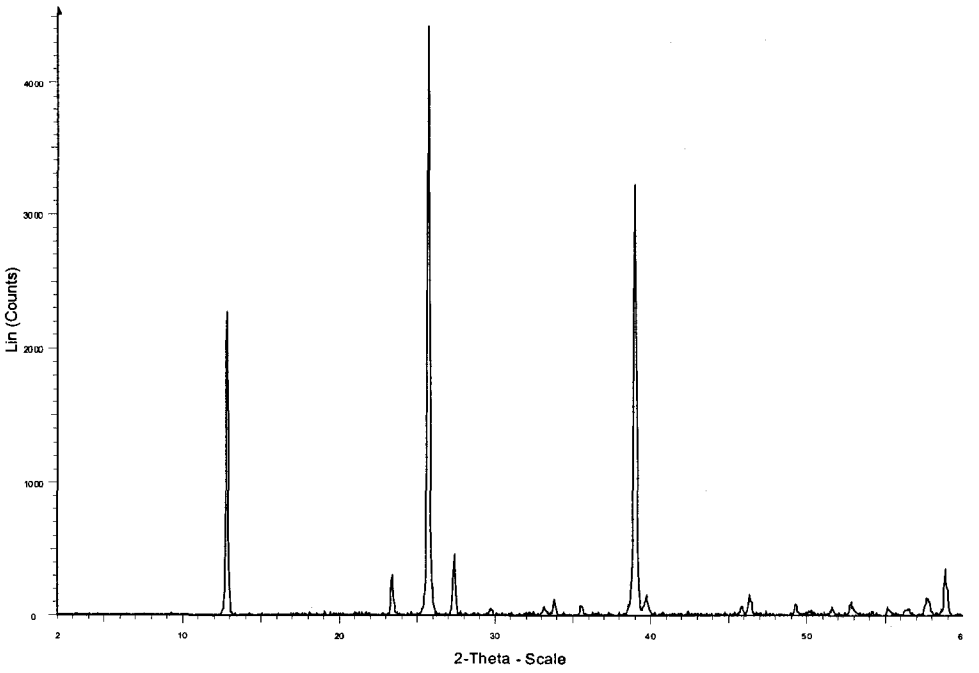

Figure 2.4 XRD spectrum of MoO_3

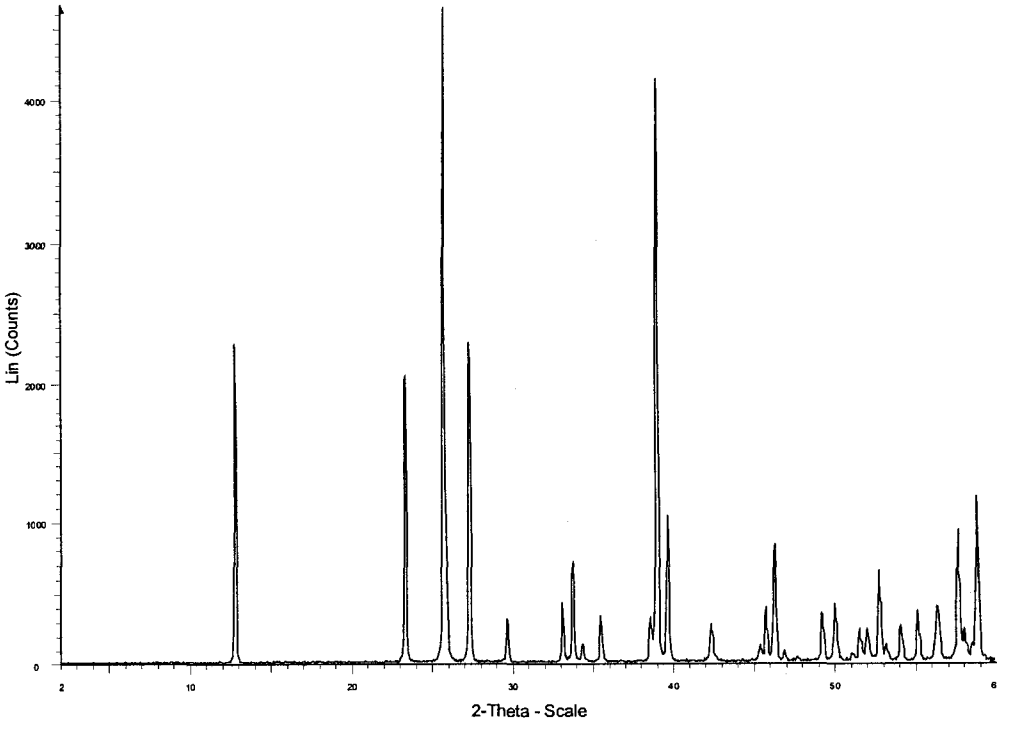

For comparison, the TGA of pristine $MoSe_2$ was also run in a nitrogen atmosphere (Figure 2.5). In nitrogen, $MoSe_2$ is stable up to 418 °C. In the thermogram, it can be observed that a plateau is reached at 600 °C. The weight change of 8.4% is attributed to the loss of Se atoms from the $MoSe_2$ sheets. The XRD powder pattern of the sample after TGA in nitrogen up to 700 °C is depicted in Figure 2.6. The powder pattern is very close to that of pristine $MoSe_2$. Therefore, no chemical transformation is observed for the $MoSe_2$ sample after TGA under nitrogen flow.

Figure 2.5 TGA of $MoSe_2$ in nitrogen.

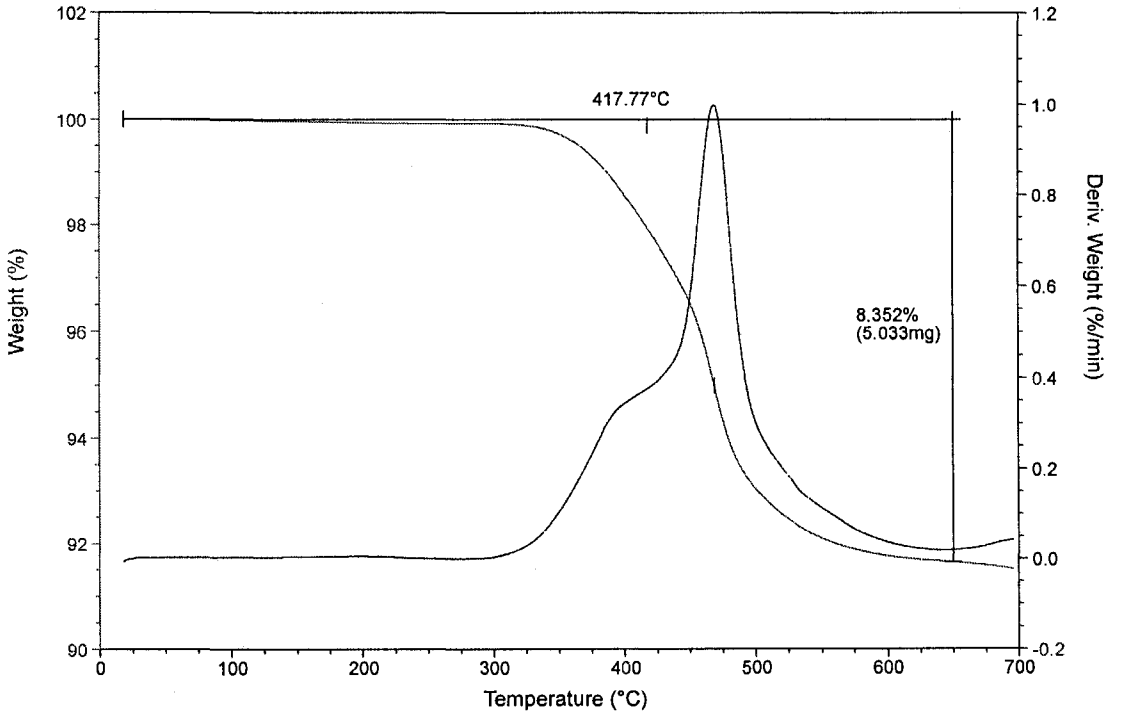

Figure 2.6 XRD spectrum of $MoSe_2$ after TGA in nitrogen up to 700 °C.

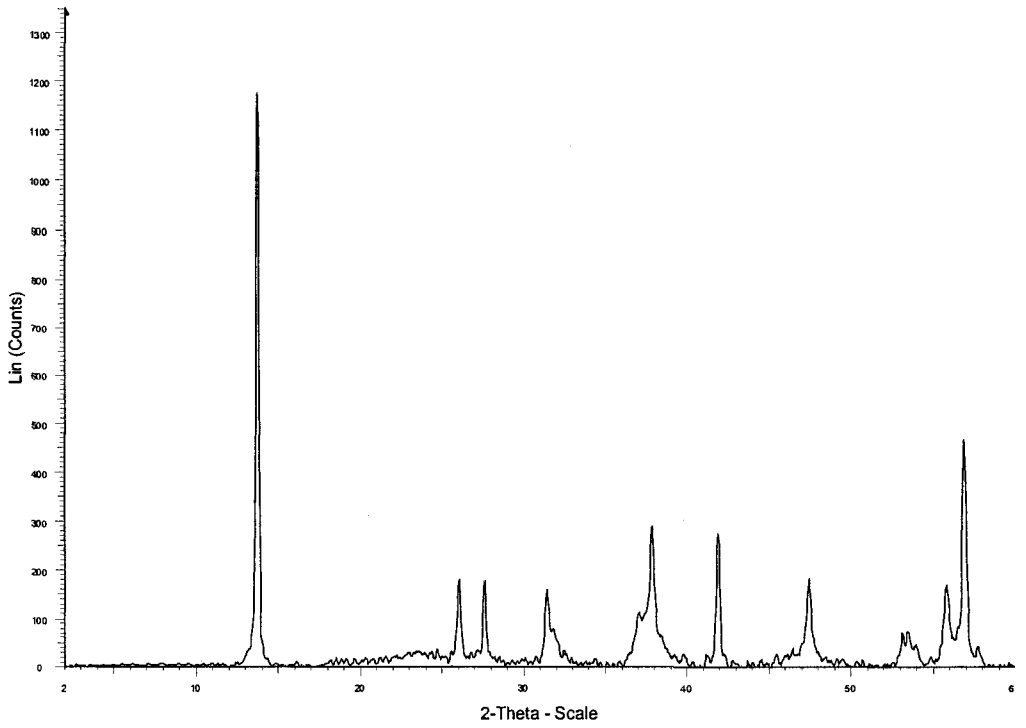

2.2.2 Lithiation, exfoliation and titration of $MoSe_2$

The formation of lithiated and exfoliated $MoSe_2$ is shown in Figure 2.7. Pristine $MoSe_2$ is neutral, however, upon treatment with n-BuLi, electrons are transferred onto the layers, and to maintain electrical neutrality, Li^+ ions are inserted in the gallery space of the layered host, resulting in the formation of Li_xMoSe_2. Addition of water or N-methylformamide (NMF) results in the association of water or NMF molecules with the Li^+ ions. The hydrogen gas formed between the layers forces the layers apart and cause complete exfoliation of the host.

Figure 2.7 Schematic diagram illustrating the formation of exfoliated $MoSe_2$

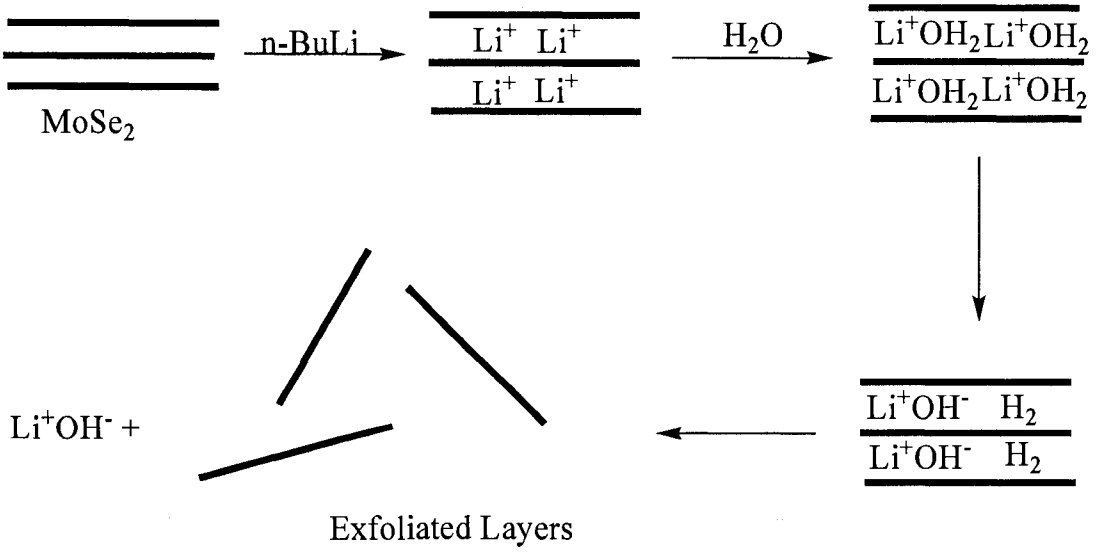

The powder pattern of a Li_XMoSe_2 sample cast on a glass slide is shown in Figure 2.8. Powder X-ray diffraction clearly shows a peak corresponding to a d-spacing value of 6.64 Å. Compared to the powder pattern of pristine $MoSe_2$, there is an interlayer expansion of 0.22 Å, and this corresponds to the insertion of lithium ions. This interlayer expansion value is close to that observed in the MoS_2 system (0.16 Å).[55] The absence of peaks from other reflection planes indicates that, similar to the MoS_2 system, the well-stacked, layered crystal structure is changed into a less-ordered state upon lithiation.[55]

Figure 2.8 XRD spectrum of Li_xMoSe_2

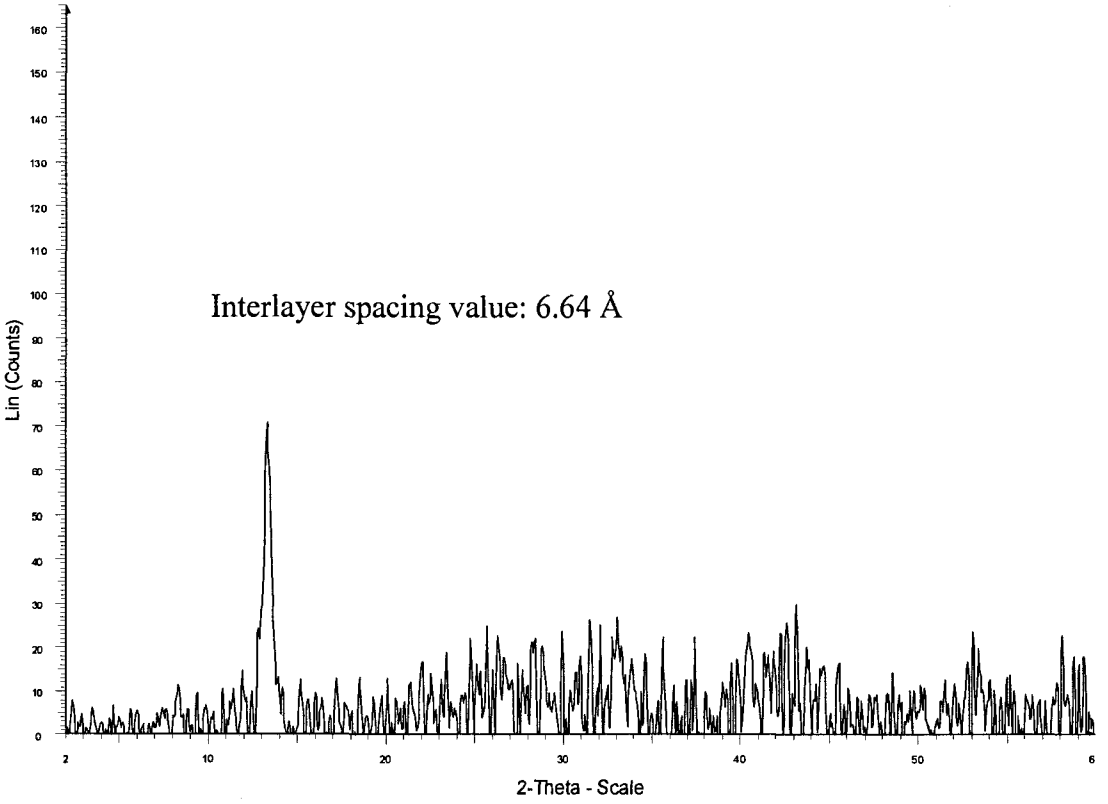

The objective of the titration experiment as described in section 2.1.3 is to determine the lithium content in Li_xMoSe_2. The titration experiment was performed two times and the value of x in Li_xMoSe_2 was found to $Li_{0.7}MoSe_2$. (The values from the two experiments are $Li_{0.65}MoSe_2$ and $Li_{0.67}MoSe_2$).

2.2.3 'Restacked $MoSe_2$'

Powder XRD shows a peak with a d-spacing value of 6.64 Å for $Li_{0.7}MoSe_2$ (See Figure 2.8) but no peaks are observed for 'restacked' $MoSe_2$ (See Figures 2.9 and 2.11). This indicates complete exfoliation of Li_xMoSe_2 and thorough diffusion of LiOH from the layered structure (See Figure 2.7). Otherwise, there must be a peak or several peaks in

Figure 2.9. The totally disordered phase from 'restacked' $MoSe_2$ is due to the strong lone pair repulsion from 'Se' atoms across the layers[62] and the increased entropy in comparison to that of the ordered phase. In contrast, restacked MoS_2 layers were found to have a similar interlayer spacing value as that of pristine MoS_2,[67] due to the stronger adhesive force and weaker lone-pair repulsion between MoS_2 layers.[55, 62]

Figure 2.9 XRD spectrum of 'restacked $MoSe_2$' without addition of acid.

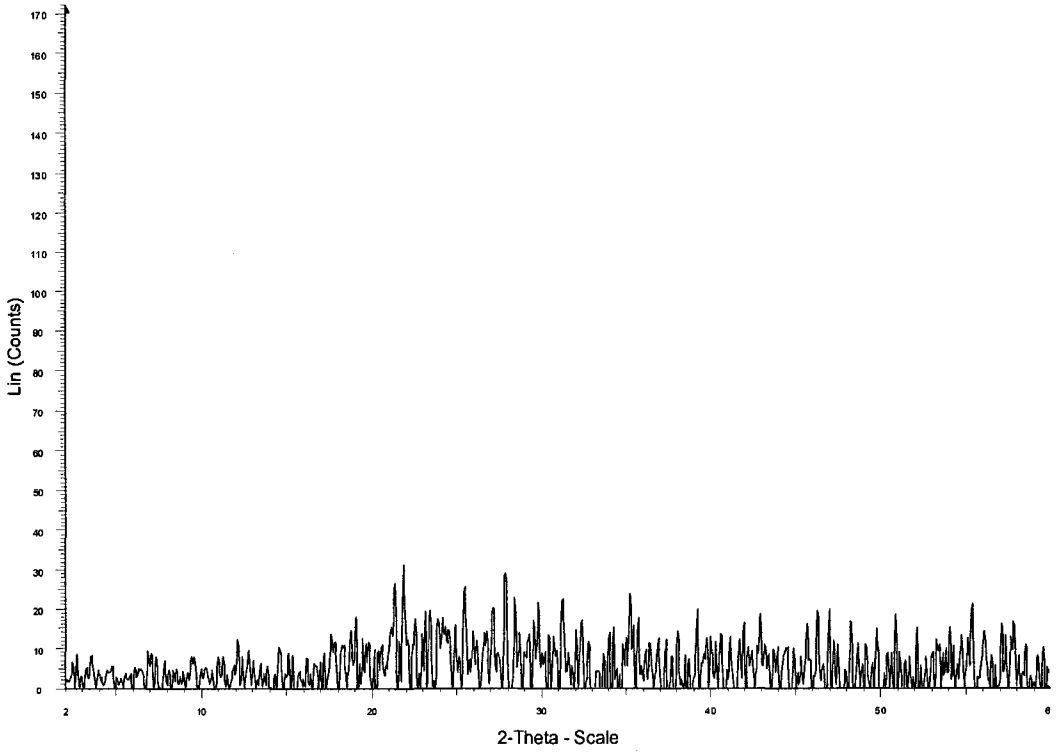

The powder patterns of 'restacked $MoSe_2$' treated by HCl acid before centrifugation and after centrifugation are shown in Figure 2.10 and Figure 2.11, respectively. Powder pattern in Figure 2.10 indicates that $MoSe_2$ restacks in acidic medium and the interlayer expansion is 5.01 Å with respect to pristine $MoSe_2$ due to the intercalation of hydronium ions.[67] A disordered phase is obtained upon centrifugation which reveals that

restacked $MoSe_2$ is not as stable as restacked MoS_2 due to the stronger lone pair repulsion between 'Se' atoms.[62]

Figure 2.10 XRD spectrum of 'restacked $MoSe_2$' with acid

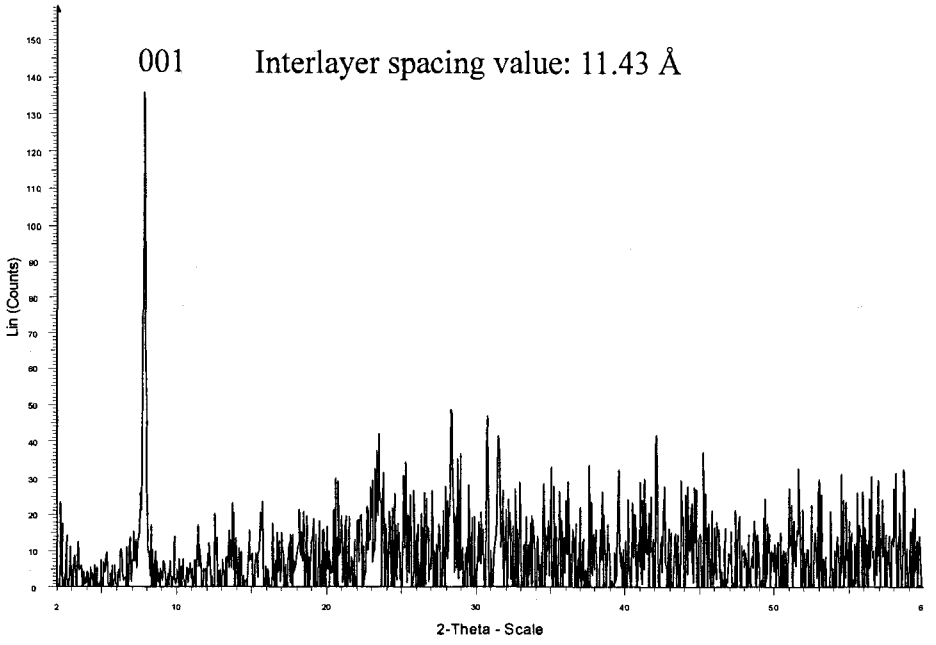

Figure 2.11 XRD spectrum of 'restacked $MoSe_2$' with acid after centrifugation

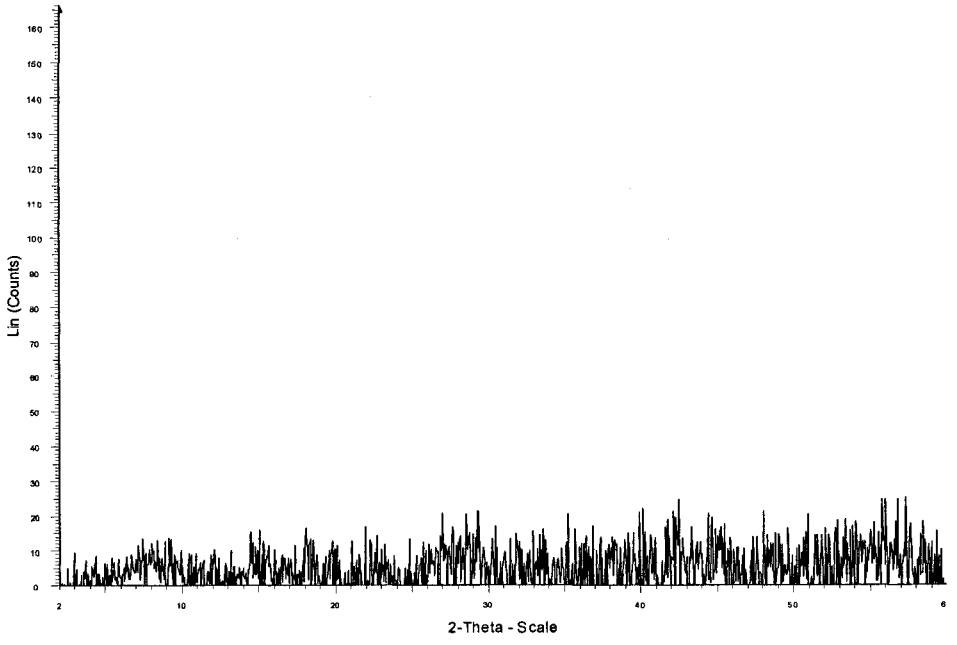

TGA of 'restacked $MoSe_2$' in air (Figure 2.12) shows that it is oxidized at 370 °C, which is close to the decomposition temperature of pristine $MoSe_2$ (372 °C). However, substantially less weight is observed for the remaining MoO_3 phase and this is attributed to defects (molybdenum and oxygen vacancies) in the structure.

Figure 2.12 TGA of 'restacked $MoSe_2$' in air (without acid)

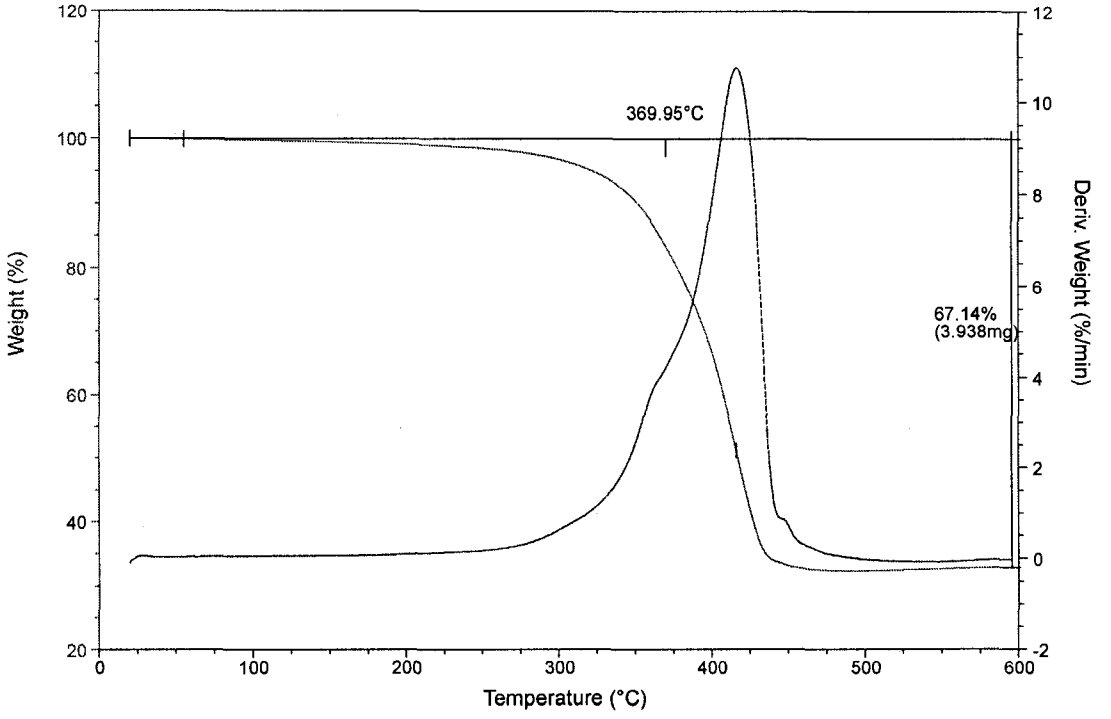

The powder pattern of 'restacked $MoSe_2$' after TGA in air up to 600 °C is shown in Figure 2.13. The powder pattern is very close to that of pure MoO_3 (Figure 2.4) indicating that $MoSe_2$ has been oxidized into MoO_3. The absence of some peaks from Figure 2.13 might be due to the defects in the lattice structure.

Figure 2.13 XRD spectrum of 'restacked $MoSe_2$' after TGA in air up to 600 °C.

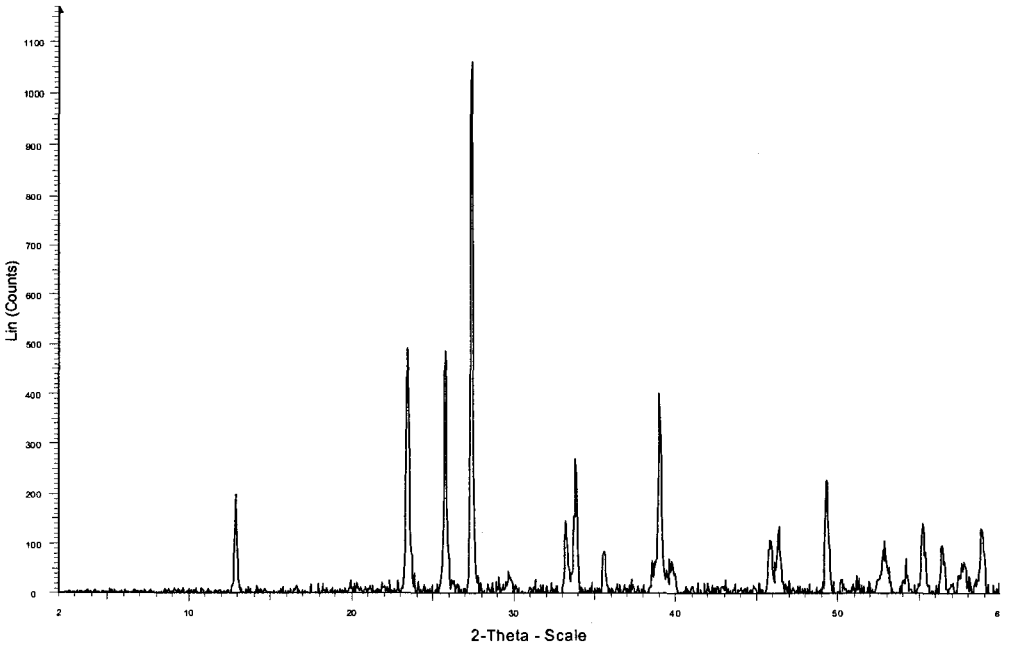

Variable temperature van der Pauw electrical conductivities were measured in a system coupled with a model 350CP CTI Cryogenics closed cycle helium refrigerator in Dr. Douglas Dahn's lab in the Department of Physics at UPEI. Electronic conductivities show that the conductivity of 'restacked $MoSe_2$' is higher than that of the pristine 2H-semiconductor form. At 293K, the pristine $MoSe_2$ is a semiconductor with a conductivity of 1.13 $x10^{-3}$ S/cm. At 300K, the conductivity of 'restacked $MoSe_2$' is 5.02 $x10^{-2}$ S/cm. The result confirmed the conversion from 2H to 1T configuration after the exfoliation and 'restacking' process.

Differential Scanning Calorimetry (DSC) was performed on a Q100 TA instrument under dry nitrogen purge using variable heating rates. The DSC of 'restacked $MoSe_2$' performed in the low temperature region (-90 °C to 40 °C) is depicted in Figure 2.14. There is no change in energy observed for 'restacked $MoSe_2$'. Figure 2.15 below shows

the DSC of 'restacked $MoSe_2$' performed in the high temperature region (40 °C to 200 °C). An endothermic peak is observed at 66 °C which corresponds to the evaporation of water from the surface of the layered structure. A broad exothermic peak is also observed at 162 °C and this is attributed to the conversion of 'restacked $MoSe_2$' from the 1T form (O_h metallic) to the 2H-type (D_{3h} semiconducting form).[55-57,68] The samples from high temperature DSC were run again, and no peaks were observed indicating the conversion of $MoSe_2$ from 1T to 2H-type is irreversible. As a comparison restacked MoS_2 converts to the 2H-MoS_2 at 92 °C.[69] This suggests that the 1T metallic form of 1T-$MoSe_2$ is more stable than the 1T metallic form of MoS_2.

Figure 2.14 DSC for 'restacked $MoSe_2$' (-90 to 40 °C, heating rate: 5 °C/min)

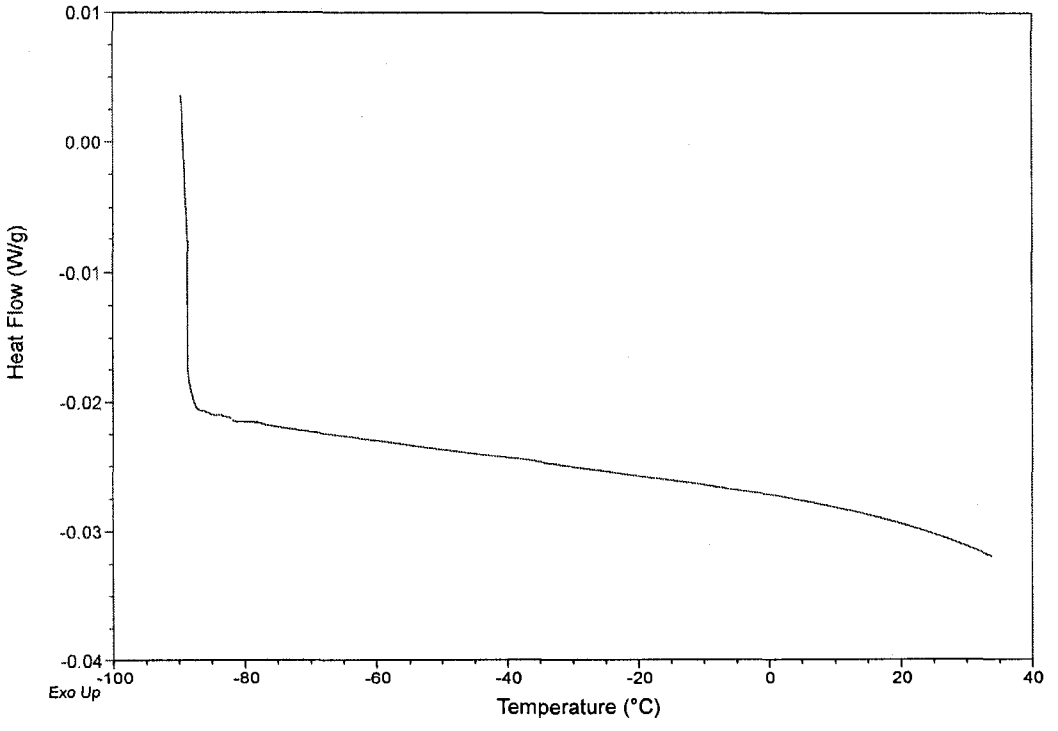

With increasing heating rate, it is observed that the exothermic peak shifts to higher temperature (Figures 2.15-2.18). The data are summarized in Table 2.1.

Figure 2.15 DSC for 'restacked $MoSe_2$' (40 to 200 °C, heating rate: 5 °C/min)

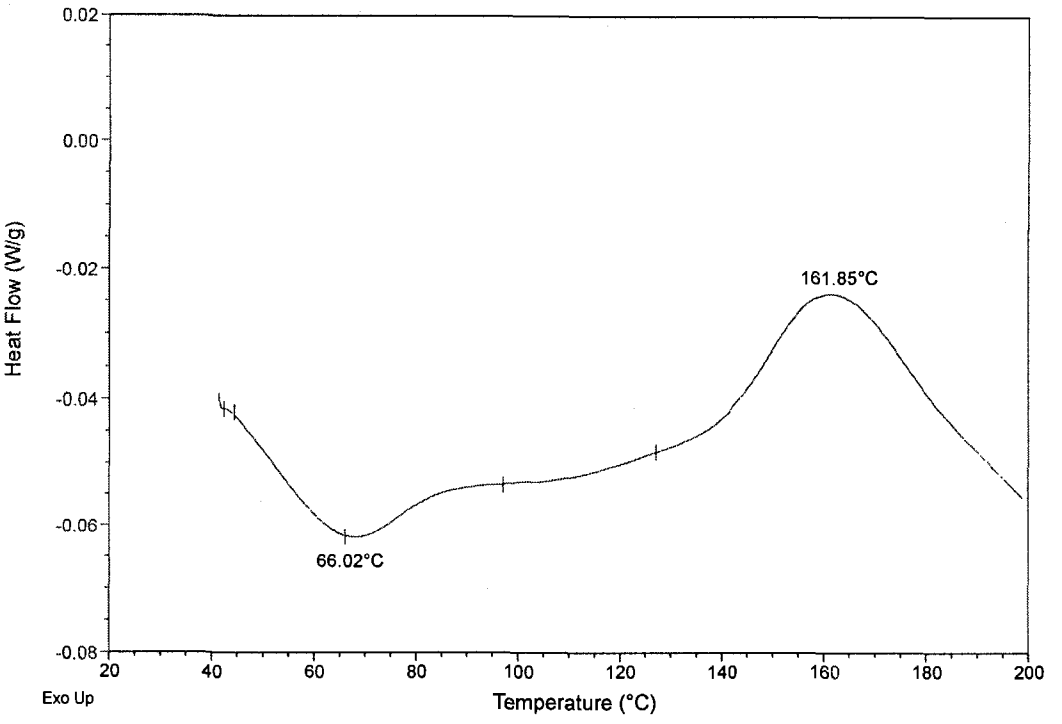

Figure 2.16 DSC for 'restacked $MoSe_2$' (40 to 200 °C, heating rate: 10 °C/min)

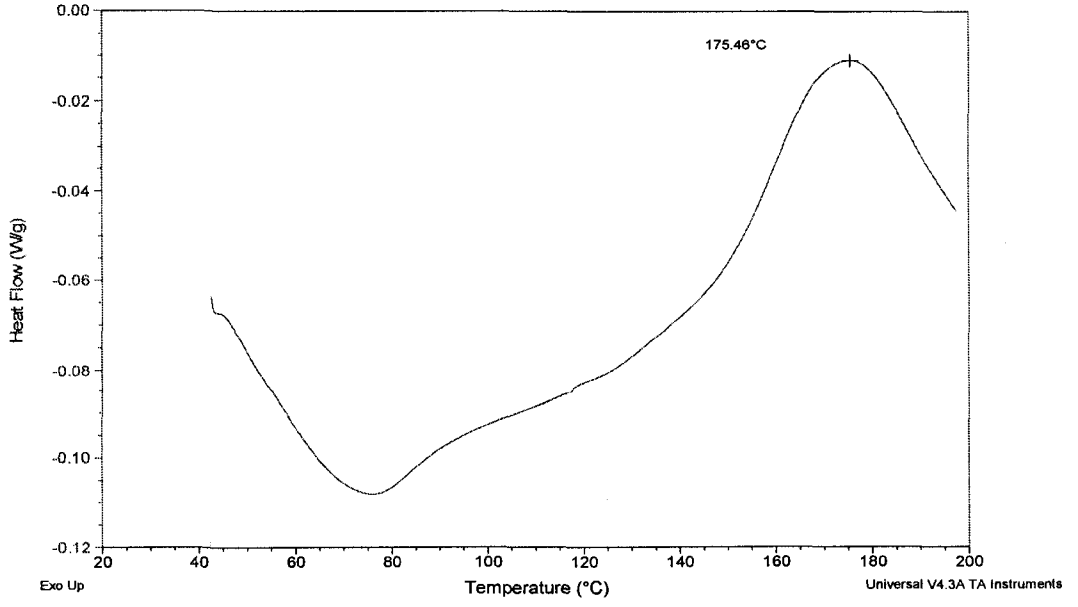

Figure 2.17 DSC for 'restacked $MoSe_2$' (40 to 200 °C, heating rate: 15 °C/min)

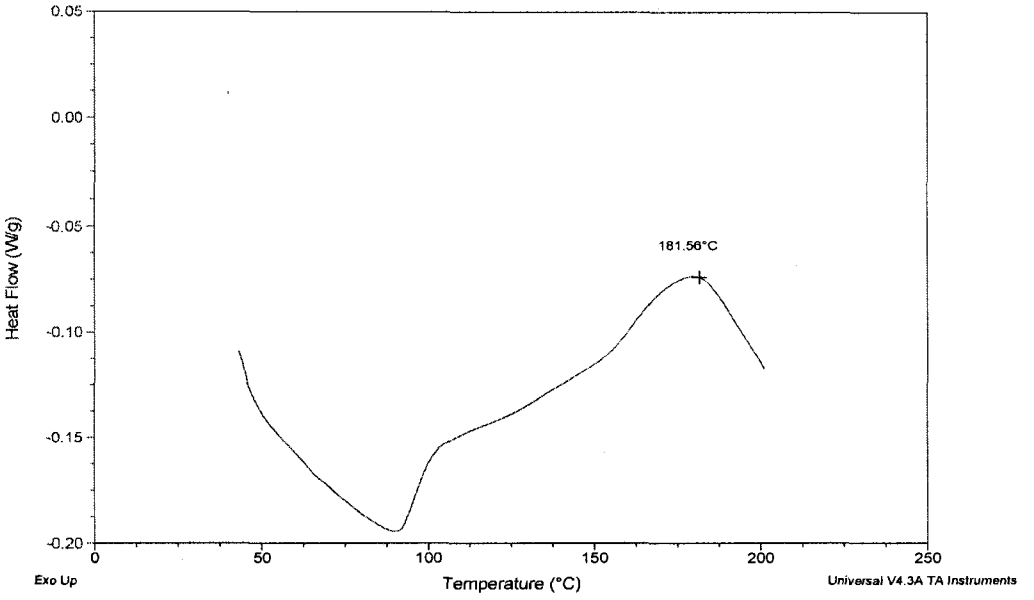

Figure 2.18 DSC for 'restacked $MoSe_2$' (40 to 200 °C, heating rate: 20 °C/min)

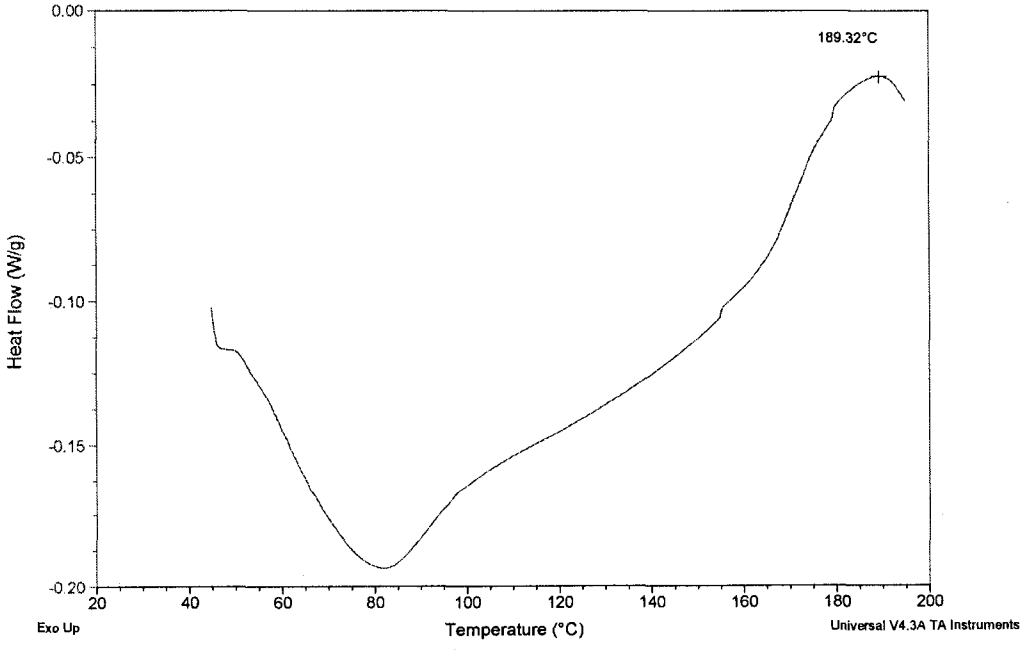

Table 2.1 DSC data on 'restacked $MoSe_2$'

Heating rate (β) K/min	Max of the transition temperature (T)
5	434 K
10	448 K
15	455 K
20	462 K

The activation energy (E_a) for the conversion of $MoSe_2$ from 1T to 2H-form was determined by fitting the set of data in Table 2.1 into an Arrhenius-type of equation as shown in Equation 2.2, where β is heating rate, R is molar gas constant ($8.314 J \cdot K^{-1} \cdot mol^{-1}$), T is the maximum transition temperature (K), E_a is the activation energy in $J \cdot mol^{-1}$, and A is a constant.[70]

$$\ln \beta = E_a/RT + A \qquad 2.2\ [70]$$

From the slope of the straight line (Figure 2.19), the activation energy 'E_a' (1T to 2H-$MoSe_2$) was found to be 84 kJ/mole, which is higher than that of WS_2 and MoS_2.[68] This is ascribed to the fact that the selenium atoms are larger and heavier than the sulphur atoms and this hinders the "glide motion"[55] of the 'Se' atoms from 1T to 2H-type $MoSe_2$. Therefore, 1T-$MoSe_2$ is more stable relative to 1T-MoS_2.

Figure 2.19 Kinetic Arrhenius plot for the conversion of 'restacked $MoSe_2$' from 1T-form to 2H-form.

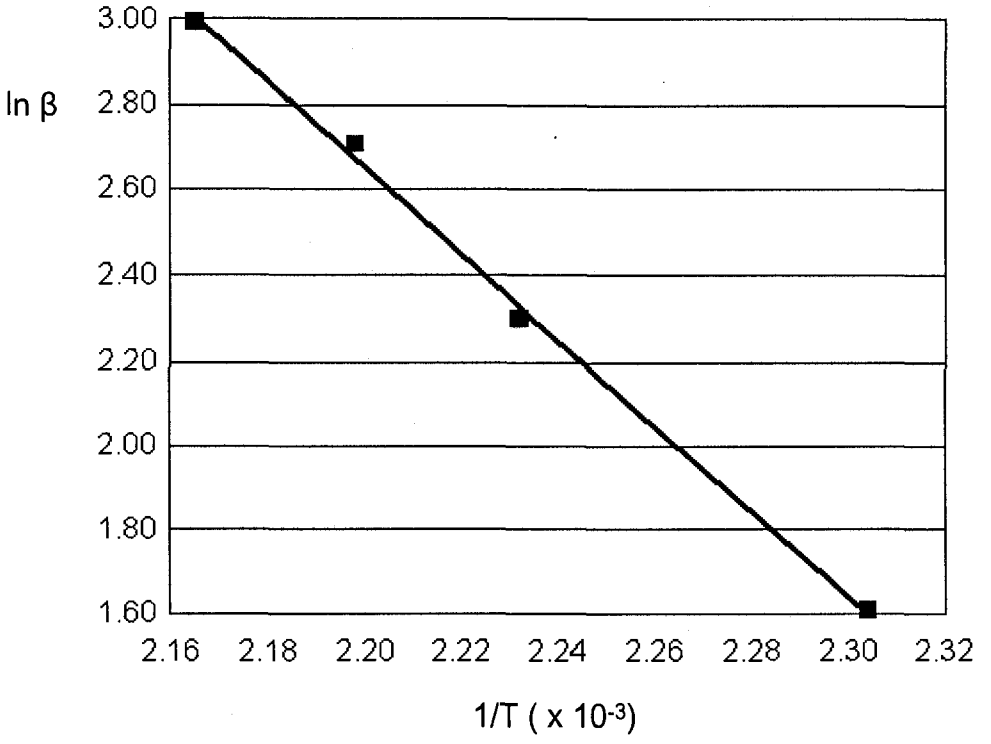

Exfoliated $MoSe_2$ single layers have been achieved in this chapter. It seems that without the introduction of the guest species, $MoSe_2$ does not restack orderly. This might be due to the strong lone pair repulsion between the $MoSe_2$ single layers.[62] The disordered $MoSe_2$ single layers have a much larger surface area compared with pristine $MoSe_2$ and restacked MoS_2. This suggests that, in principle, as an HDS catalyst, 'restacked $MoSe_2$' may have more activity than pristine $MoSe_2$ or restacked MoS_2. It will be very interesting to test the HDS catalytic activity of 'restacked $MoSe_2$' in the future. Guest species such as organic molecules can help $MoSe_2$ single layers to restack orderly. Compared with pristine $MoSe_2$, sandwiched compounds with increased entropy and a reduced coulombic repulsion between $MoSe_2$ layers may be formed.[55]

Chapter 3: $MoSe_2$ and Solid Polymer Electrolytes

Complete exfoliation of $MoSe_2$ in Chapter 2 creates opportunities for solid polymer electrolytes to be inserted into the $MoSe_2$ layers. The resulting compounds may have good ionic conductivity and mechanical stability, similar to related systems such as SPE/MoS_2[49] and SPE/MoO_3.[44]

3.0 Materials

PEO (M_W: 100,000), PVP (M_W: 63,000), Methylcellulose (M_n: 63,000), phosphonitrilic chloride trimer (99%), and lithium triflate (99.9095%) were purchased from Aldrich and used as received.

3.1 General Methodology for Synthesizing polymer/$MoSe_2$ intercalates

$Li_{0.7}MoSe_2$ (100 mg) was charged into a 50 mL Erlenmeyer flask in the dry box. The sample was removed from the dry box and deionized water (10 mL) was added. The mixture was sonicated for two hours. The polymers or polymer-salt complexes [PEO, PVP, Methyl Cellulose, POMOE, $(POMOE)_{25}$ LiOTf , MEEP and $(MEEP)_4$LiOTf] were dissolved in deionized water. The polymer solution (2 mg/mL) or solution of the polymer salt complex (2 mg/mL) was then added to the Li_xMoSe_2 suspension dropwise with stirring. The resulting mixture was allowed to stir for 24 hours at room temperature. The intercalates were purified by filtration or centrifugation. Part of the wet sample was cast on a glass substrate for XRD analysis. The rest was freeze-dried for TGA analysis. The role of adding hydrochloric acid to the reaction mixture for restacking purposes has also

been explored. HCl (12M) was added to the $MoSe_2$ suspension dropwise right after the polymer solution was added. The pH value was about 1 for all systems studied.

3.2 Results and Discussions on PEO/$MoSe_2$ intercalates

The powder X-ray diffraction pattern of pristine PEO is shown in Figure 3.1. The sharp peaks indicate that PEO is crystalline. When PEO is inserted into $MoSe_2$ the peaks corresponding to PEO are no longer observed, suggesting that the intercalation of PEO into $MoSe_2$ suppresses the tendency of the polymer to crystallize. Therefore, in principle, the ionic conductivity of the intercalated polymer can be improved.

Figure 3.1XRD spectrum of PEO [71]

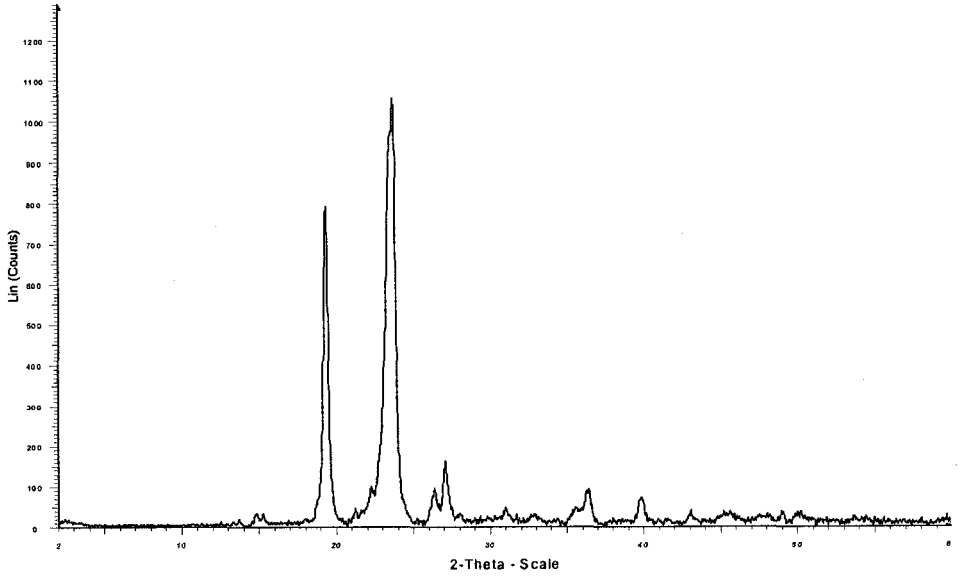

XRD spectra of PEO/$MoSe_2$ nanocomposites with different mole ratios between $MoSe_2$ and the PEO are shown in Figures 3.2 - Figure 3.6. The interlayer spacings for these composites are constant, around 16 Å. The average interlayer expansion value is around 9.3 Å, close to that of PEO/MoS_2 (9.2 Å).[72] This interlayer expansion value

corresponds to a bilayer insertion of the polymer, as determined by the computational cross-section diameter of PEO (4 Å).[73] Varying the mole ratio of PEO to $MoSe_2$ has no effect on the interlayer spacing in these materials. This is attributed to the host-guest interaction and guest-guest interaction. In general, the loading capacity of a layered structure for a particular guest species is limited. For example, some polymers are only allowed to stack up to a maximum of two layers in the confined van der Waals gap of a layered structure. Addition of HCl during the intercalation process did not change the interlayer spacing of the intercalate either. From the powder patterns, the average crystallite size of the intercalates were found to be 72 Å, a five-fold decrease when compared with pristine $MoSe_2$ which has an average crystallize size of 370 Å. This is due to the imperfect restacking of $MoSe_2$ with PEO.[51]

Figure 3.2 XRD spectrum of PEO/$MoSe_2$ intercalate (1:1 mole ratio)

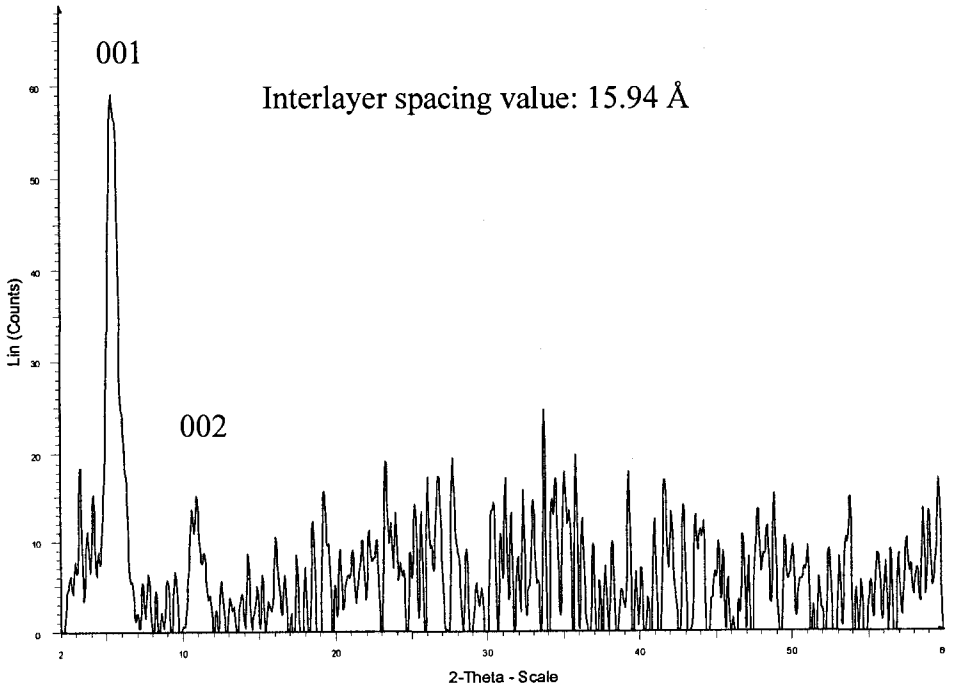

Figure 3.3 XRD spectrum of PEO/$MoSe_2$ intercalate (1.6:1 mole ratio)

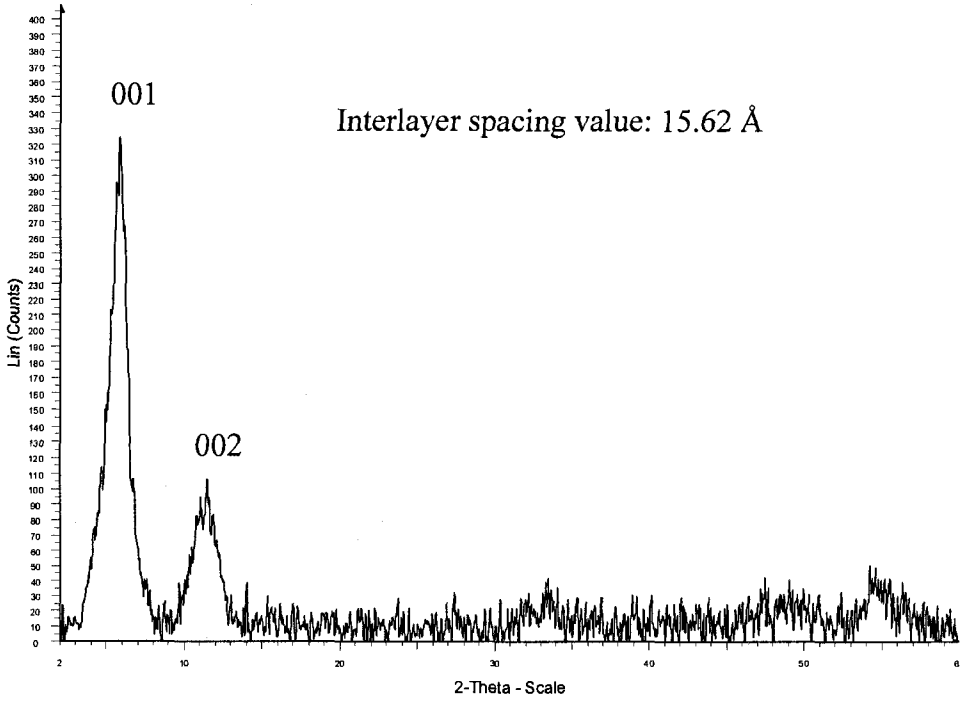

Figure 3.4 XRD spectrum of PEO/$MoSe_2$ intercalate (2.2:1 mole ratio)

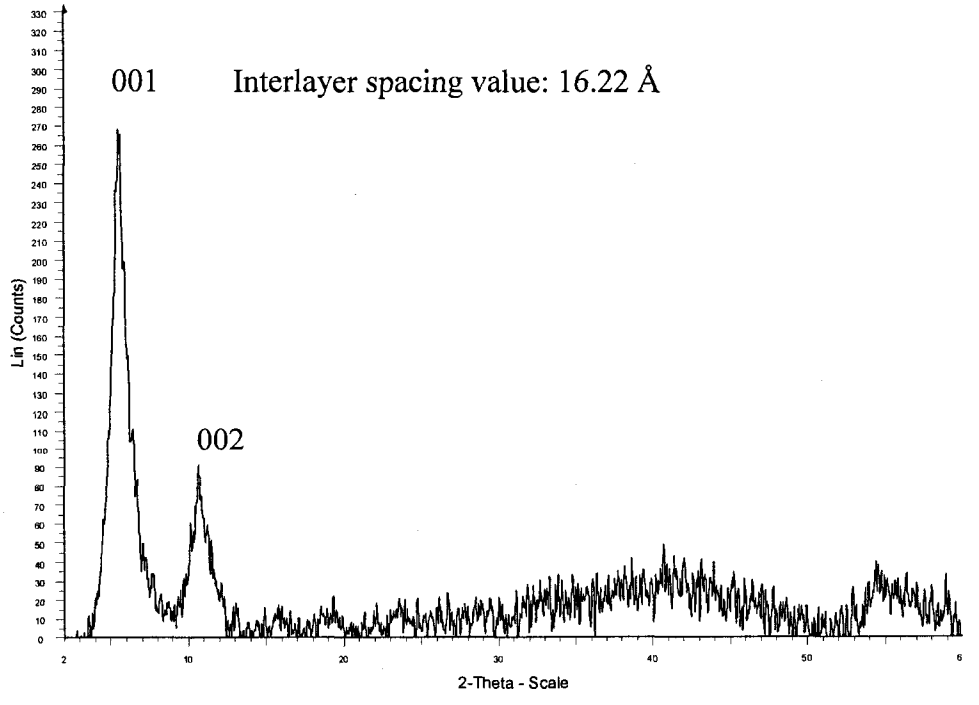

Figure 3.5 XRD spectrum of PEO/$MoSe_2$ intercalate (6:1 mole ratio)

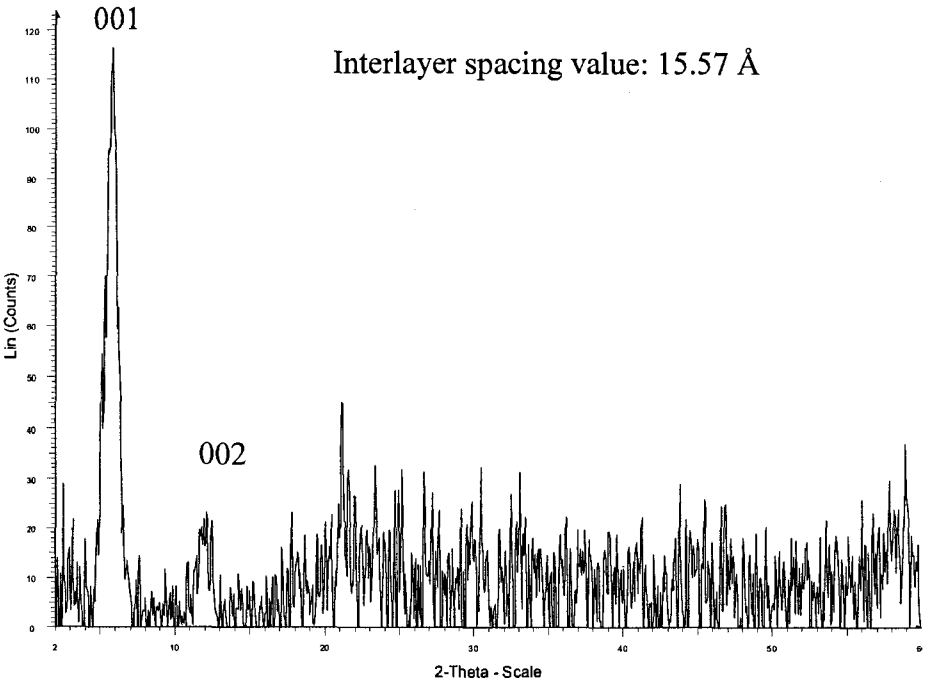

Figure 3.6 XRD spectrum of PEO/$MoSe_2$ intercalate with added acid (pH: 0.55, 6:1 mole ratio)

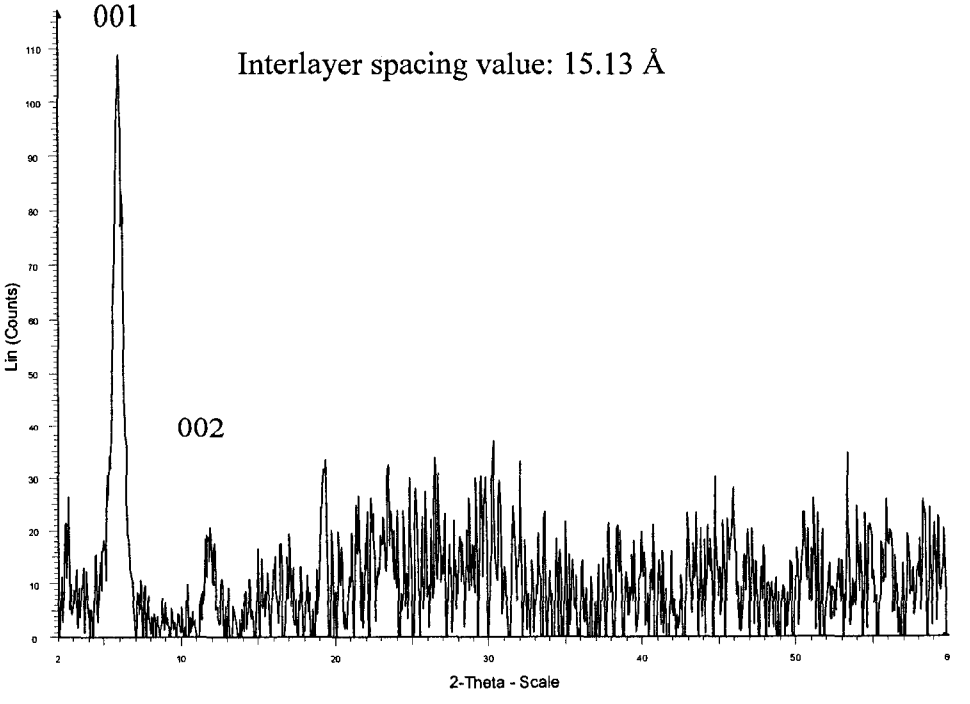

The stoichiometry of the polymer/$MoSe_2$ nanocomposites can be determined from TGA. TGA studies show that in air, PEO decomposes from 220 °C to 450 °C (Figure 3.7). It should be noted that 'restacked' $MoSe_2$ was oxidized from 337 °C to 500 °C (Figure 2.12), *i.e.* the two decomposition temperature ranges overlap. The thermogram (in air) of the intercalation compound of PEO into $MoSe_2$ in a 1:1 mole ratio is shown in Figure 3.8. There was no weight change at 220 °C (Figure 3.8), which indicates all of the externally lying PEO was washed away during the isolation of the intercalate and that the $MoSe_2$ layered structure delays the decomposition of the intercalated PEO. The composition of the material as determined from the TGA data was found to be $(H_2O)_{1.62}(PEO)_{1.23}MoSe_2$. The mole ratio between PEO and $MoSe_2$ is close to the actual ratio (1:1) used during the intercalation reaction. It is reasonable to have co-intercalation of water molecules, since the intercalation reaction was done in an aqueous medium.

Figure 3.7 TGA of PEO in air [71]

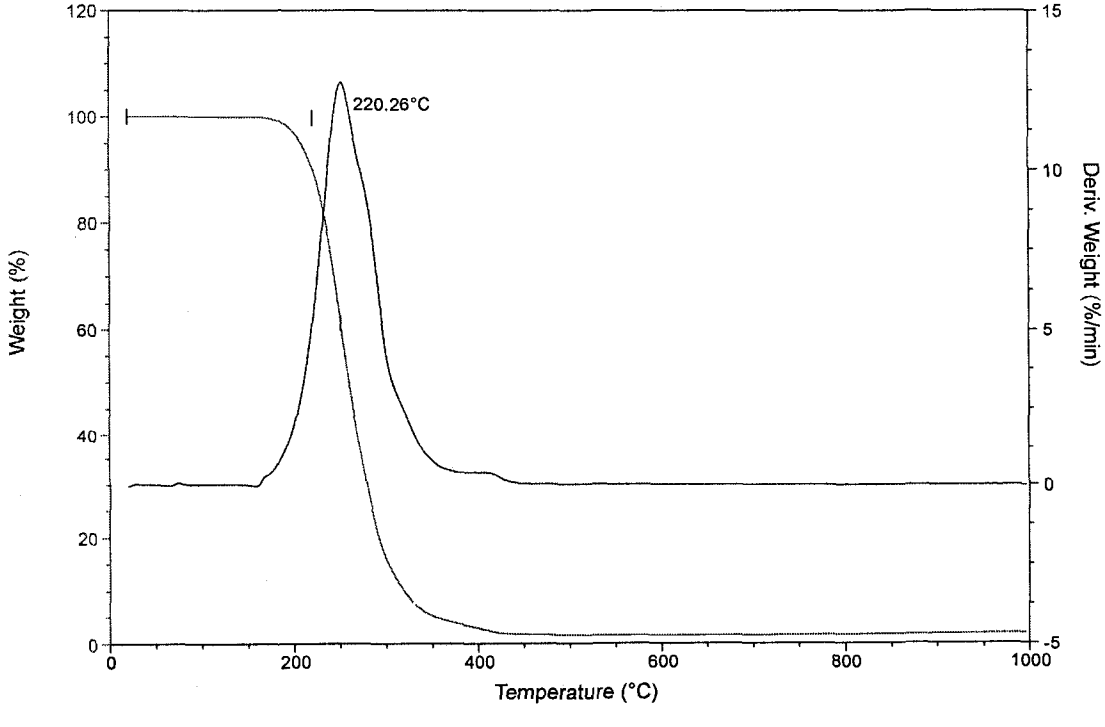

Figure 3.8 TGA of PEO/$MoSe_2$ intercalate in air (1:1 mole ratio)

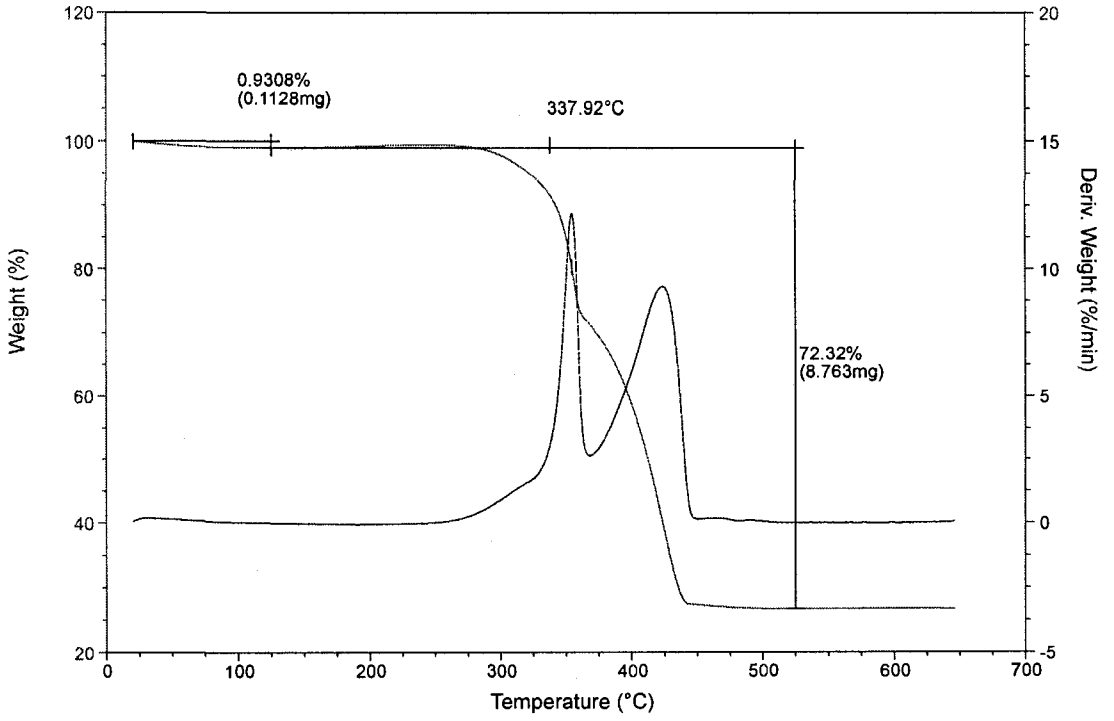

3.3 Results and Discussions on PVP/$MoSe_2$ intercalate

The XRD pattern of pristine PVP is depicted in Figure 3.9. There are no sharp peaks in the diffractogram indicating that PVP is amorphous. XRD pattern of the PVP/$MoSe_2$ nanocomposite is shown in Figure 3.10. The d-spacing of the intercalate is 22.02 Å. This corresponds to an interlayer expansion value of 15.6 Å close to that of PVP/MoS_2 (14.9 Å). This interlayer expansion value corresponds to a bilayer insertion of the polymer, as determined by the computational cross-section diameter of PVP (8 Å).[73] The first three diffraction peaks can be clearly seen in the diffractogram due to the fairly well-ordered, restacked crystals. From the powder pattern of the intercalate, its average crystallite size was found to be 253 Å. Compared with the PEO/$MoSe_2$ system, this fairly large crystallite size indicates a greater affinity between PVP and the $MoSe_2$ host.

When the mole ratio of PVP to $MoSe_2$ was increased from 1:1 to 2:1, no effect on the interlayer spacing value of the intercalate was observed, indicating that the host-guest and the guest-guest interactions only allow a maximum bilayer stacking of PVP between the $MoSe_2$ layers. Addition of acid also did not have an effect on the interlayer expansion.

Figure 3.9 XRD spectrum of pristine PVP [71]

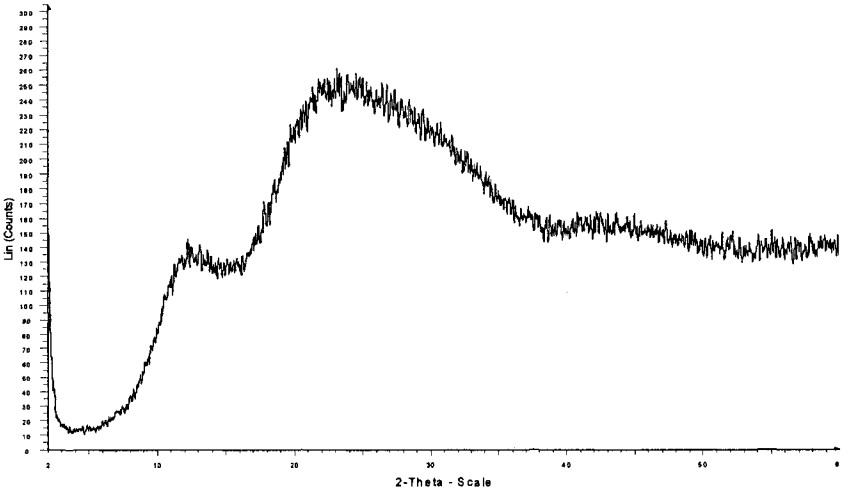

Figure 3.10 XRD spectrum of PVP/$MoSe_2$ intercalate (1:1 mole ratio)

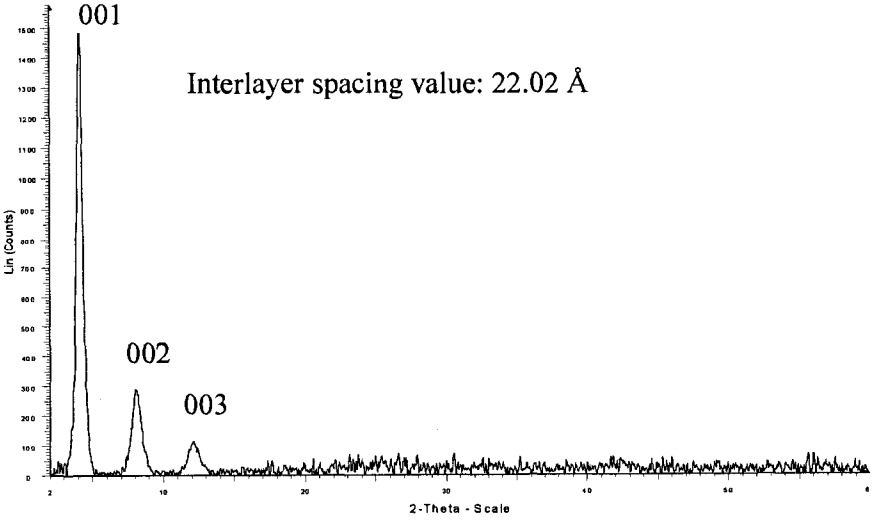

Thermogrametric analysis in air shows that both PVP and PVP/$MoSe_2$ decomposed at 312 °C (Figure 3.11 and 3.12). This might be attributed to some of the polymer chains staying out of the layered host and behaving as pristine PVP. PVP in the sandwiched compound was oxidized faster than pristine PVP. This might be due to a chemical reaction between the guest and the host at high temperatures. The stoichiometry was determined in a similar manner to that of the PEO/$MoSe_2$ system. The calculated composition is $(H_2O)_{0.51}(PVP)_{0.75}MoSe_2$. The mole ratio between PVP and $MoSe_2$ is a little lower compared to the actual ratio (1:1) used during the intercalation reaction. This is attributed to the loading capacity of the layered structure for a particular guest species, *i.e.* only a certain maximum amount of a polymer can be inserted into the host.

Figure 3.11 TGA of PVP in air[71]

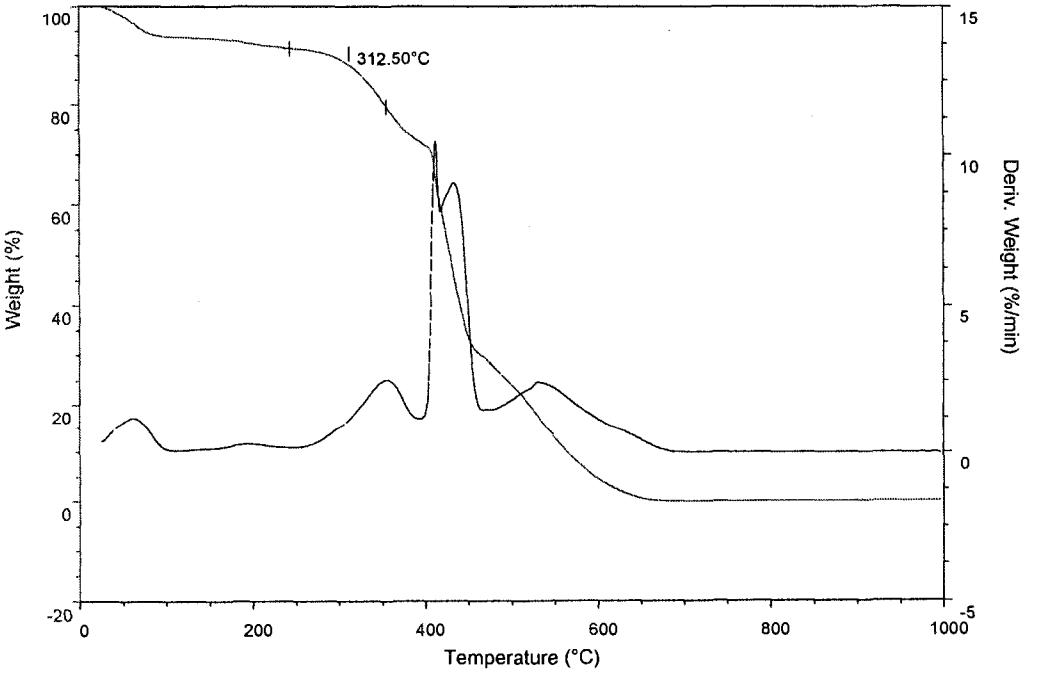

Figure 3.12 TGA of PVP/$MoSe_2$ intercalate in air

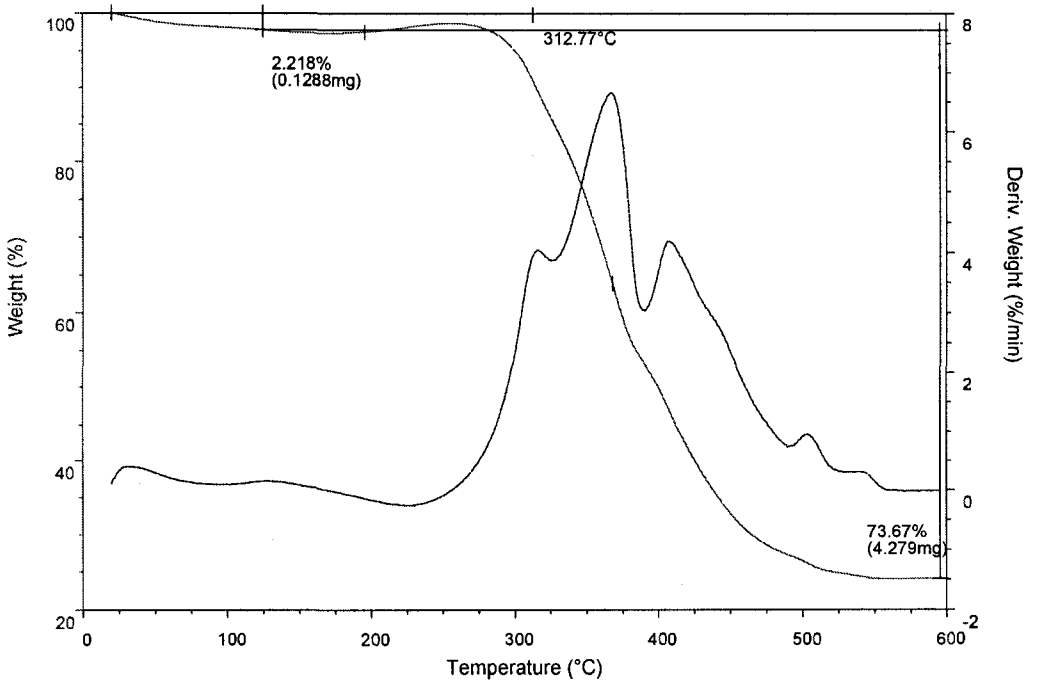

3.4 Results and Discussions on methyl cellulose/$MoSe_2$ intercalate

XRD powder pattern of methyl cellulose (MCel) is shown in Figure 3.13. The broad peak shows that methyl cellulose is amorphous. Figure 3.14 shows the powder pattern of methyl cellulose/$MoSe_2$ sandwiched compound. The d-spacing is 20.7 Å with an interlayer expansion of 14.3 Å in comparison to pristine $MoSe_2$. This interlayer expansion value is close to that of the methyl cellulose/MoS_2 system (14.2 Å).[72] A bilayer insertion of the polymer is observed based on the computational cross-section diameter of MCel (7 Å).[73] From the powder pattern of the intercalate, the average crystallite size of the intercalate was 86 Å which is smaller than that of pristine $MoSe_2$ due to the imperfect restacking of $MoSe_2$ with MCel.[51]

Figure 3.13 XRD spectrum of methyl cellulose [71]

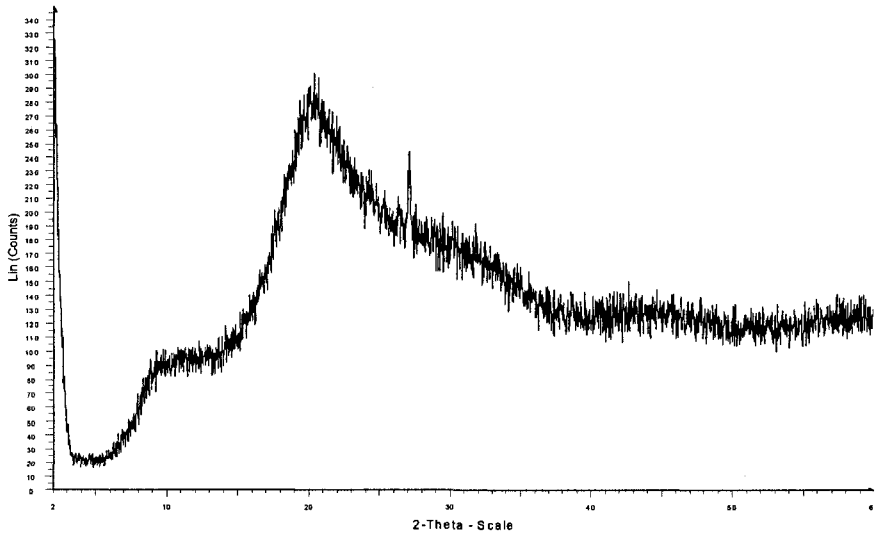

Figure 3.14 XRD spectrum of methyl cellulose/$MoSe_2$ intercalate (0.5:1 mole ratio)

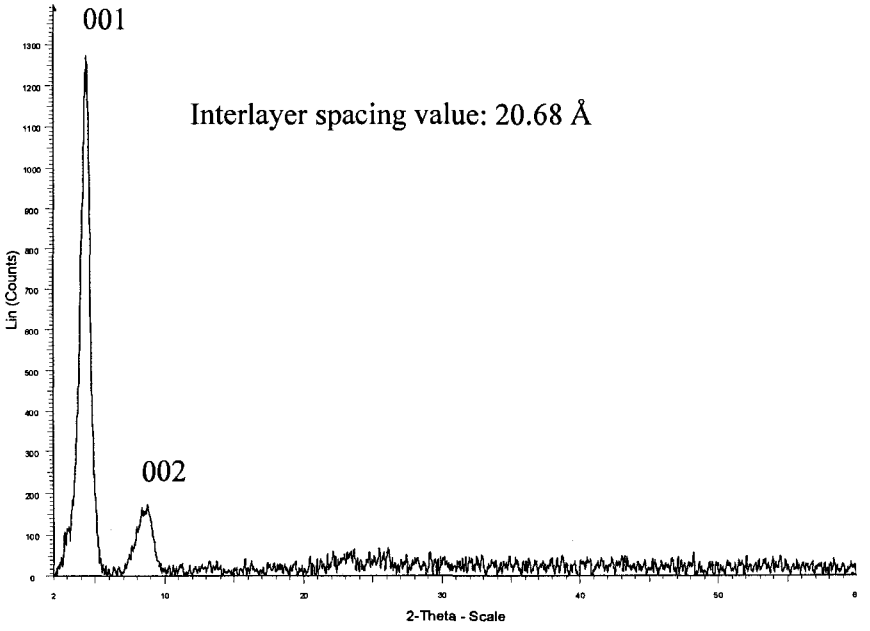

TGA (Figure 3.15) shows that methyl cellulose decomposes from 296 °C to 600 °C (in air), which overlapped with the decomposition temperature of $MoSe_2$ (372-580 °C).

Figure 3.15 TGA of methyl cellulose in air[71]

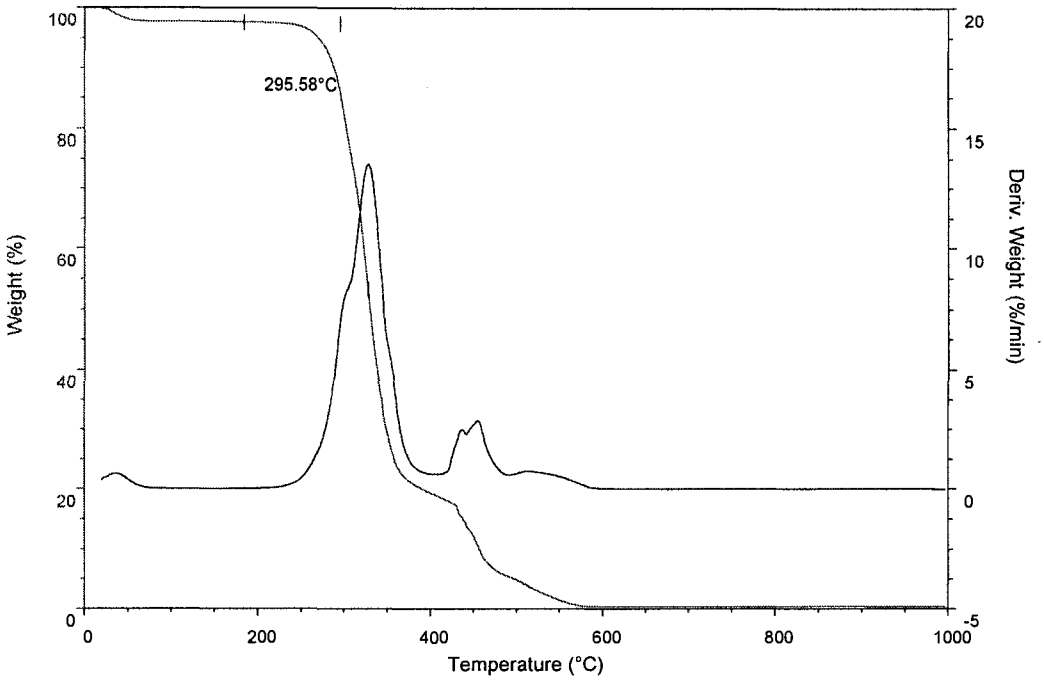

The TGA of methyl cellulose/$MoSe_2$ intercalate in air is depicted in Figure 3.16. The data shows that there was 0.04410 mg of water which evaporated until the first plateau was reached. The intercalated compound of methyl cellulose into $MoSe_2$ decomposed earlier than the pristine polymer. This might be due to the increased surface area of the polymer. The MCel molecules were separated by the $MoSe_2$ layers. At about 700 °C, a weight loss is observed due to the sublimation of MoO_3. The calculated stoichimetry is $(H_2O)_{0.058}$ (methyl cellulose)$_{0.56}$ $MoSe_2$. The actual mole ratio of methyl cellulose to $MoSe_2$ used in the reaction was (methyl cellulose)$_{0.5}$ $MoSe_2$.

Figure 3.16 TGA of methyl cellulose/$MoSe_2$ intercalate in air

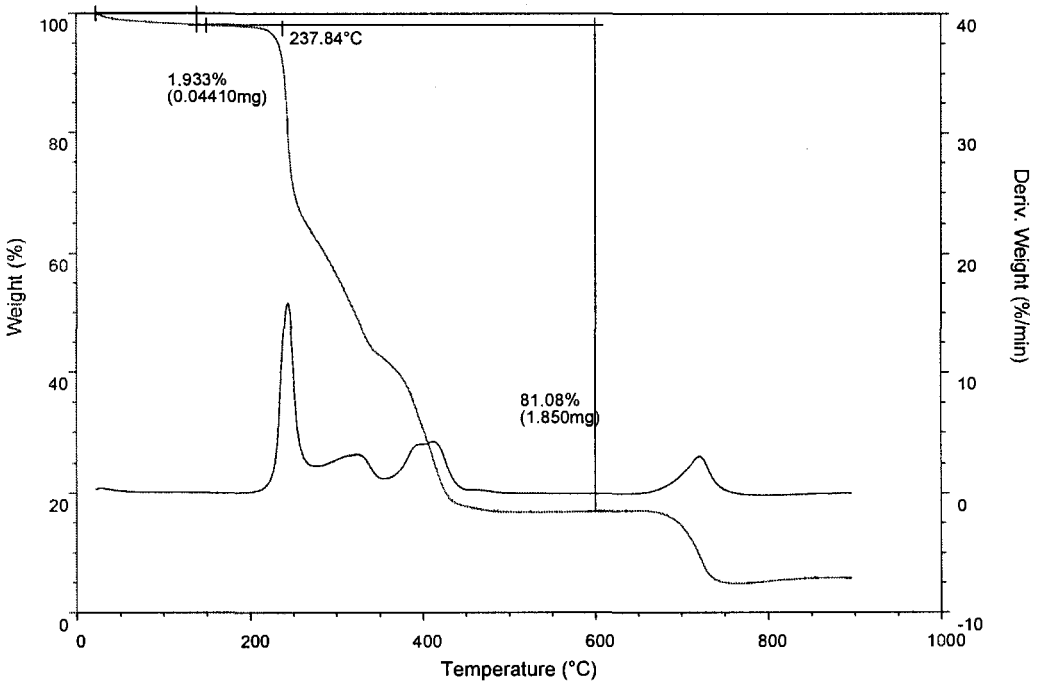

3.5 POMOE/$MoSe_2$ System

3.5.1 Synthesis of POMOE and LiOTf/$POMOE_{25}$ complex

POMOE was synthesized as described in the literature.[39] 50.00 grams (0.8913 mol) of KOH was ground into a fine powder and placed in a three-neck flask. 136.0 mL (2.122 mol) of dried dichloromethane was transferred to the three-neck flask, under nitrogen purge. 34.00 mL (0.8508 mol) of PEG (MW400) that had been dried over molecular sieves was then added dropwise *via* a dropping funnel. The flask was then stirred under nitrogen purge during the PEG addition. The reaction was stirred in the dark for three days at room temperature. Thereafter, the excess dichloromethane was removed under vacuum and water was added to dissolve the excess KOH. The resulting solution was then transferred to dialysis tubes to remove the excess KOH. A

clear liquid remained after dialysis. The sample was freeze-dried to leave a highly viscous material. The balanced equations of the reaction is shown below:

$$2\ KOH + HO(CH_2CH_2O)_9OH \rightarrow KO(CH_2CH_2O)_9OK + 2\ H_2O \qquad 3.1$$

$$n\ KO(CH_2CH_2O)_9OK + n\ CH_2Cl_2 \rightarrow [(OCH_2CH_2)_9OCH_2]_n + 2n\ KCl \qquad 3.2$$

7.7g of POMOE was dissolved in 100 mL deionized water and mixed with 1.14g of $LiCF_3SO_3$ dissolved in 50 mL of deionized water. Therefore, the mole ratio of the ether functional group to lithium ion was $(POMOE)_{25}LiOTf$.[39] The mixture was allowed to stir for 16 hours and then the water was evaporated by freeze-drying.

3.5.2 Results and Discussions on POMOE and POMOE/$MoSe_2$ system (NMR, XRD, TGA, FTIR, and DSC)

Nuclear Magnetic Resonance (NMR) spectra were collected on a Bruker 300 spectrometer. (300 MHz for the ^1H spectra, 75MHz for the ^{13}C spectra and 121 MHz for the ^{31}P spectra). Deuterated chloroform ($CDCl_3$) was used as the reference solvent. (H_3PO_4 was used as the reference for ^{31}P spectra)

The ^1H NMR spectrum of POMOE is depicted in Figure 3.17. The peak at 4.71 ppm corresponds to -OC$\boldsymbol{H_2}$$(OCH_2CH_2)_9$- and the peak at 3.60 ppm corresponds to -$OCH_2(OC\boldsymbol{H_2}C\boldsymbol{H_2})_9$-. The results are in good agreement with the literature.[74-76] The ^{13}C NMR spectrum of POMOE along with the chain structure interpretation are

shown in Figure 3.18. The results are also very close to the literature values.[77-78]

Figure 3.17 ^{1}H NMR spectrum of POMOE

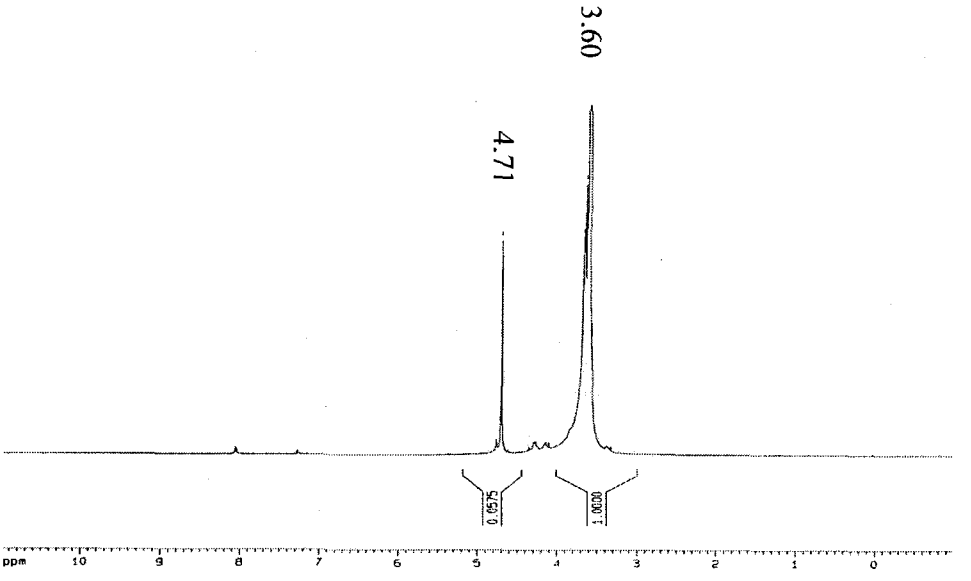

Figure 3.18 ^{13}C NMR spectrum of POMOE and the Chain Structure Interpretation

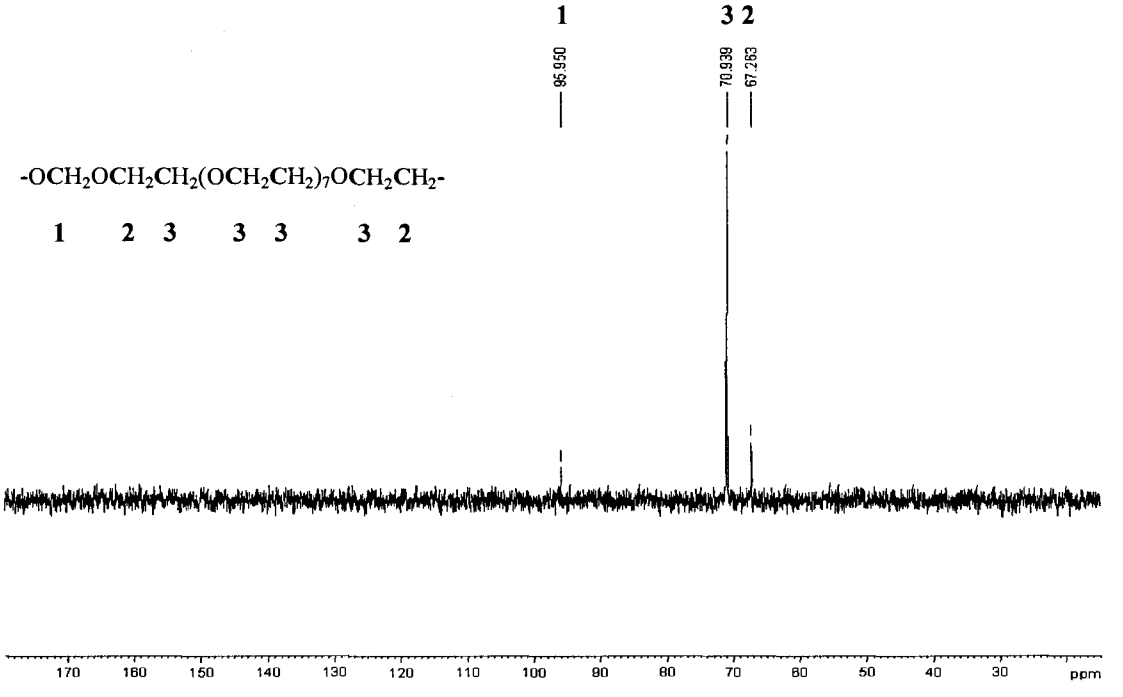

XRD powder pattern of POMOE is shown in Figure 3.19. The broad peak shows that POMOE is amorphous. The powder X-ray diffraction pattern of POMOE/$MoSe_2$ is depicted in Figure 3.20. The first and second diffraction peaks are clearly visible. The d-spacing of the material is 15.67 Å, which corresponds to an interlayer expansion value of 9.25 Å, which is attributed to a double-layer insertion of the polymer. This interlayer expansion value is close to that found in POMOE/MoS_2 intercalate (9.63 Å).[49] The crystallite size was 117 Å as determined by making use of the Scherrer equation. The actual mole ratio of $MoSe_2$ to POMOE used in the reaction was 1:1.3.

Figure 3.19 XRD spectrum of POMOE[71]

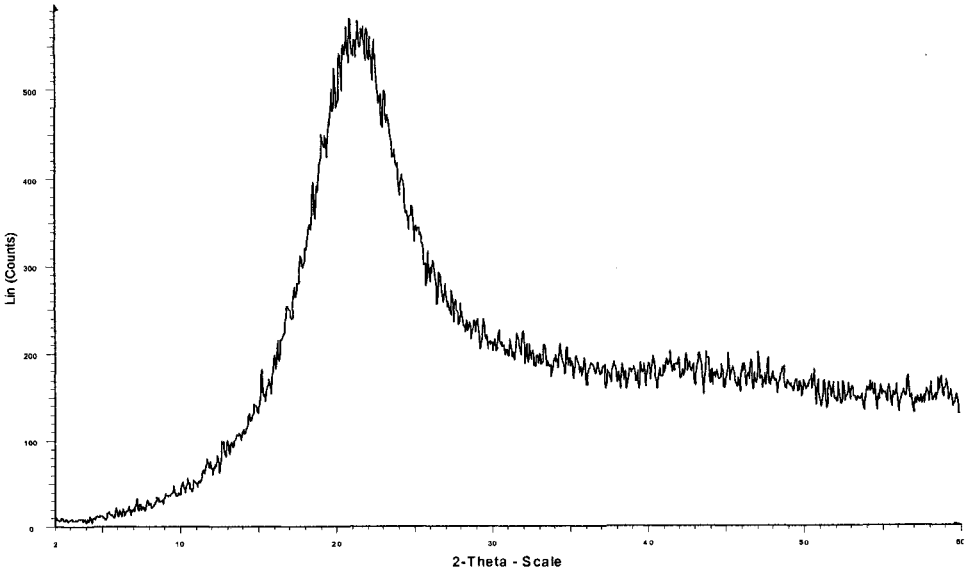

Figure 3.20 XRD spectrum of POMOE/$MoSe_2$ intercalate

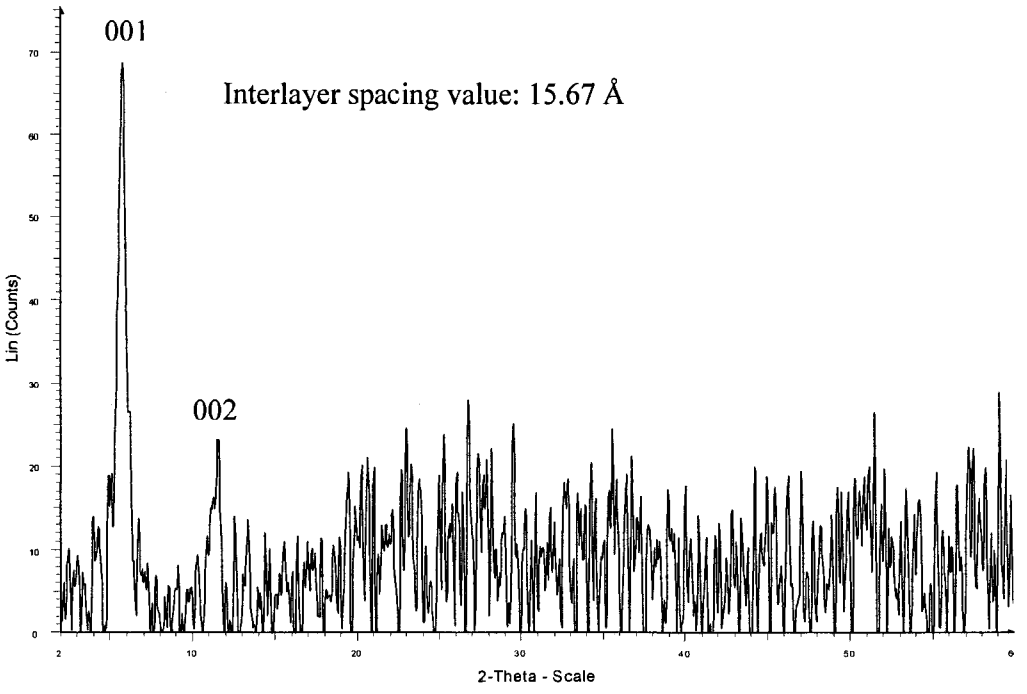

The XRD diagram of lithium triflate is shown in Figure 3.21. The sharp peaks with high intensity reveal that lithium triflate is very crystalline. However, when lithium triflate is complexed with POMOE, the resulting product is amorphous, as shown in the X-ray diffraction pattern in Figure 3.22. XRD of the sandwiched compound $(POMOE)_{25}LiOTf/MoSe_2$ is shown in Figure 3.23. The interlayer spacing is 16.99 Å, which is close to that of the POMOE/$MoSe_2$ system.

Figure 3.21 XRD spectrum of LiOTf

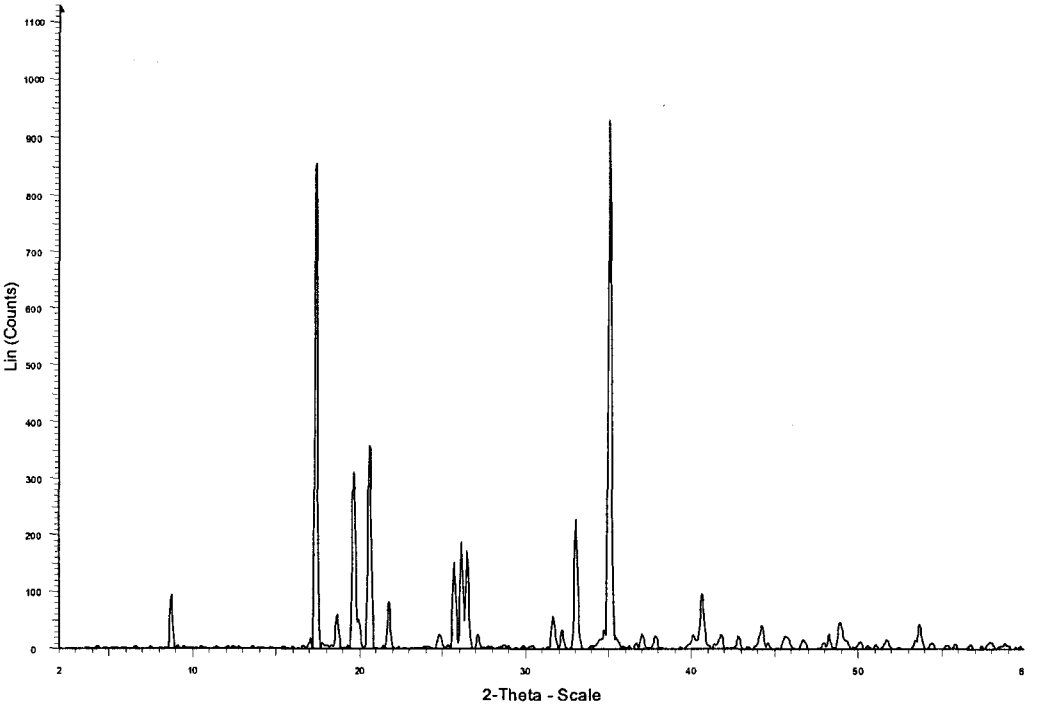

Figure 3.22 XRD spectrum of $(POMOE)_{25}LiOTf$

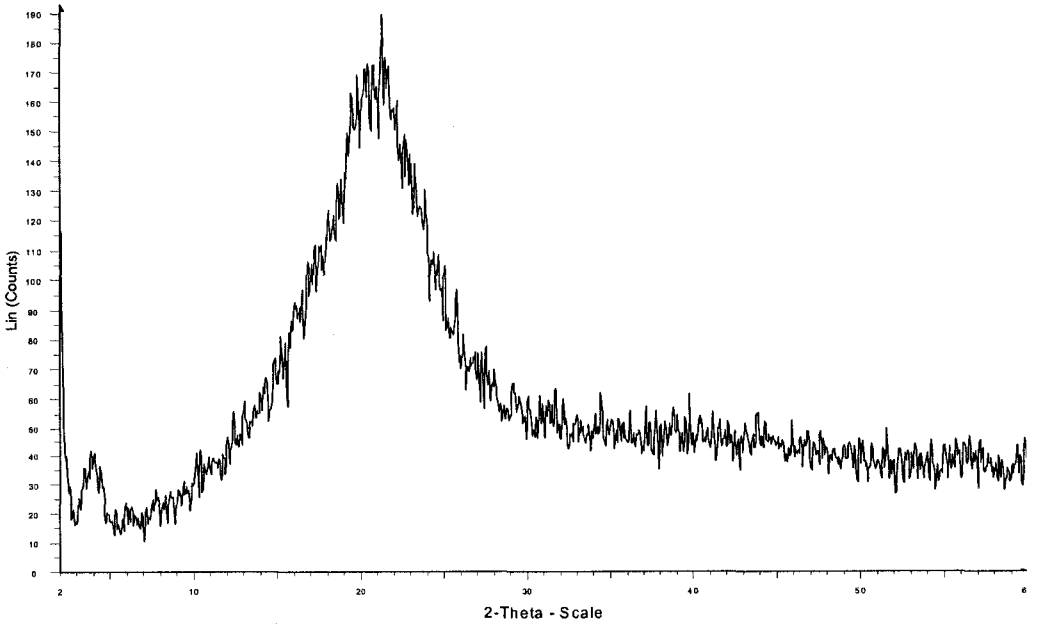

Figure 3.23 XRD spectrum of $(POMOE)_{25}LiOTf/MoSe_2$ intercalate

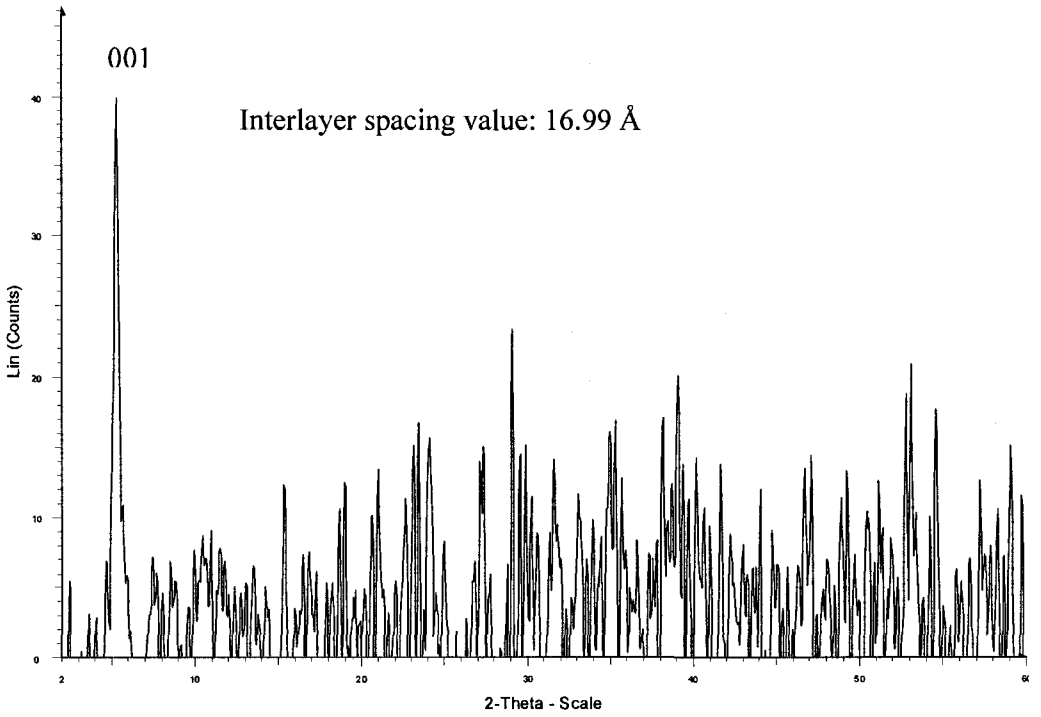

Thermal stabilities of POMOE and POMOE/$MoSe_2$ intercalate were studied through TGA. In Figure 3.24 (TGA of POMOE in air), POMOE decomposes from 215 °C to 500 °C (in air), which overlapped with the decomposition temperature of $MoSe_2$ (372-580 °C).

Figure 3.24 TGA of POMOE in air

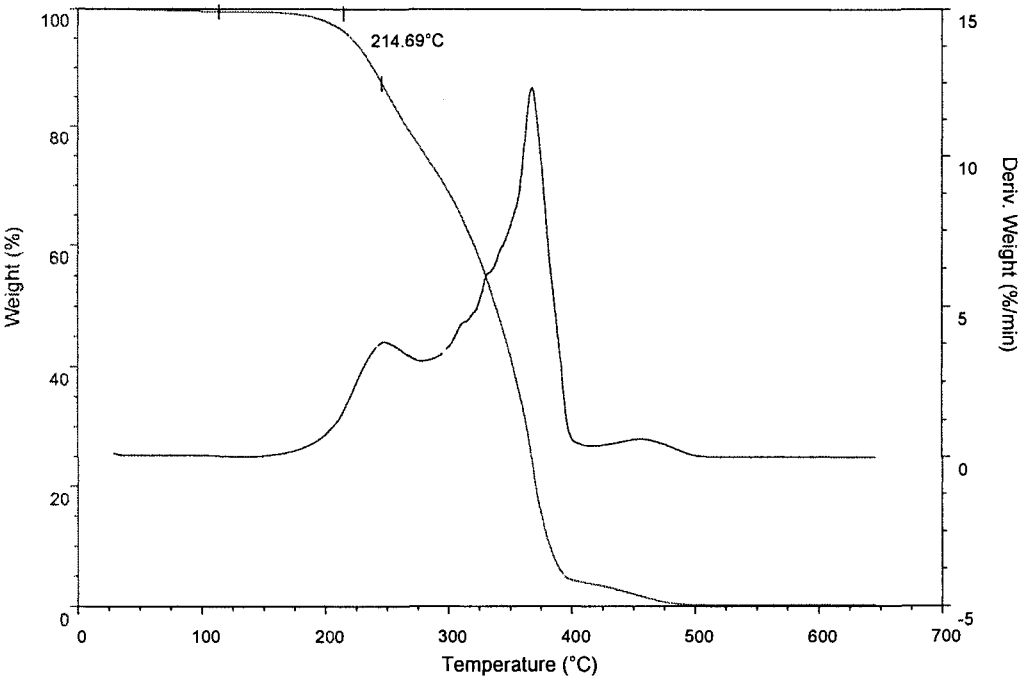

The thermogram of POMOE/$MoSe_2$ sandwiched compound is depicted in Figure 3.25. As shown in Figure 3.25, there was no weight change at 215 °C, which indicates that there is no externally lying POMOE and, in fact, the polymer is fully intercalated. The $MoSe_2$ layered structure delays the decomposition of the intercalated POMOE. The decomposition temperature of the POMOE/$MoSe_2$ sandwiched compound is 327 °C, which is lower than that of 'restacked $MoSe_2$' but higher than that of pure POMOE. This is due to the decomposition of polymer between the $MoSe_2$ layers. Therefore, layered structure delayed the decomposition of the polymer.

Figure 3.25 TGA of POMOE/$MoSe_2$ in air

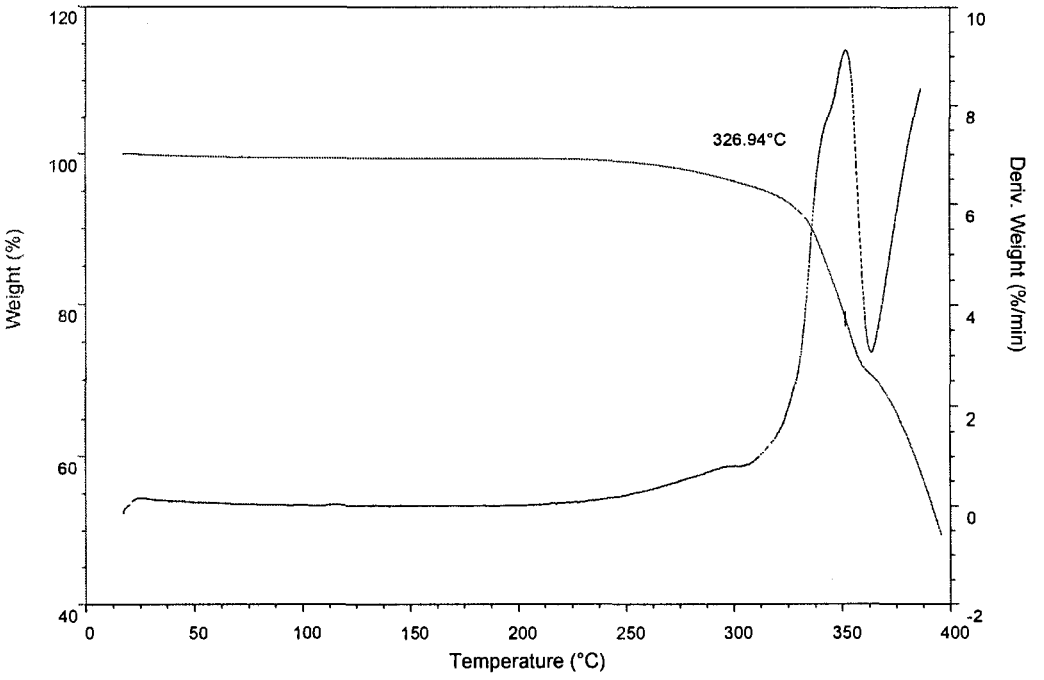

Due to damages done to the TGA thermocouple when using $MoSe_2$ samples, it was decided not to use TGA for any further characterization of $MoSe_2$ intercalates. Instead, an analytical balance and a benchtop oven were used to determine the composition of $MoSe_2$ sandwiched compounds for the rest of the project. For example, the stoichiometry of the POMOE/$MoSe_2$ intercalation compound was determined in that manner. 0.0594 g of POMOE/$MoSe_2$ at room temperature reduced to 0.0584 g at 150 °C due to evaporation of water. At 600 °C, the weight of the sample stayed constant. (0.0169 g at 600 °C and 0.0159 g at 650 °C). The sample at 650 °C was defected MoO_3, as confirmed by XRD. The composition of POMOE/$MoSe_2$ was determined to be $(H_2O)_{0.3}(POMOE)_{0.13}$ $MoSe_2$, which lower than the the actual ratio (1:1) used during the intercalation reaction. This is attributed to the fact that even

though the structure of POMOE is similar to that PEO, the molar mass of its repeat unit is much larger, and only a certain maximum amount of the repeat units can be inserted into the host.

Infra-red spectroscopy was run on a Bruker Equinox 55 series instrument as pressed KBr pellets.

When POMOE or POMOE salt complex was inserted into $MoSe_2$, the IR bands of the major bond/group of POMOE shifted to lower wavenumbers. In addition, the intensity of most peaks decrease due to host-guest interaction, *i.e.* the host limits the vibrations of the bonds in the guest polymer.[48] (Figure 3.26-3.29, Table 3.3-3.4)

Figure 3.26 FT-IR spectrum of POMOE

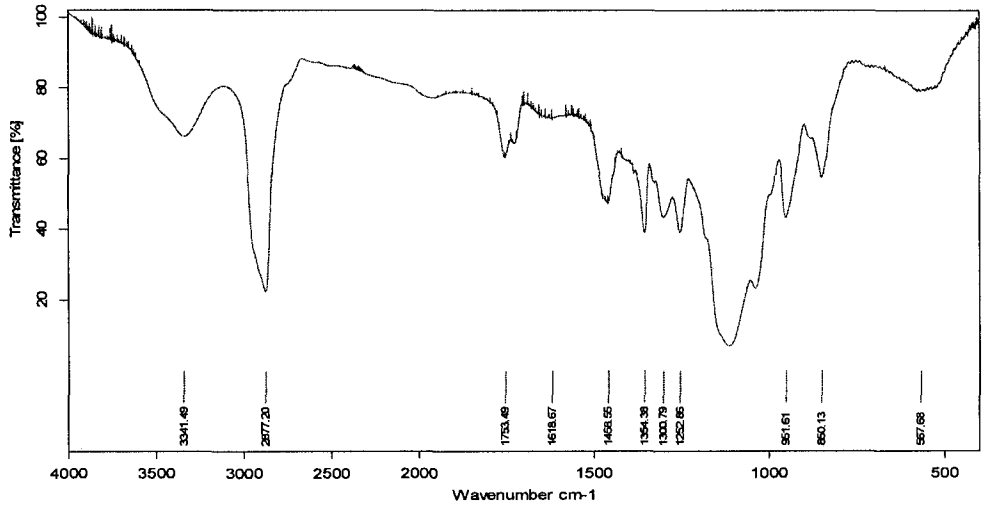

Table 3.1 Significant FT-IR peaks for POMOE [79]

Major bond/Group	Wavenumber (cm^{-1})
H-bond between molecular bond	3341
CH asymmetric bend	2877
C=O stretch	1753
OCH_2 symmetric bend	1459
CH_2 symmetric bend	1354
C-O stretch	1301
C-O stretch	1253
C-O-C stretch	1114
CH_2 rocking	952
CH_2 rocking	850

Figure 3.27 FT- IR spectrum of POMOE/$MoSe_2$ intercalate

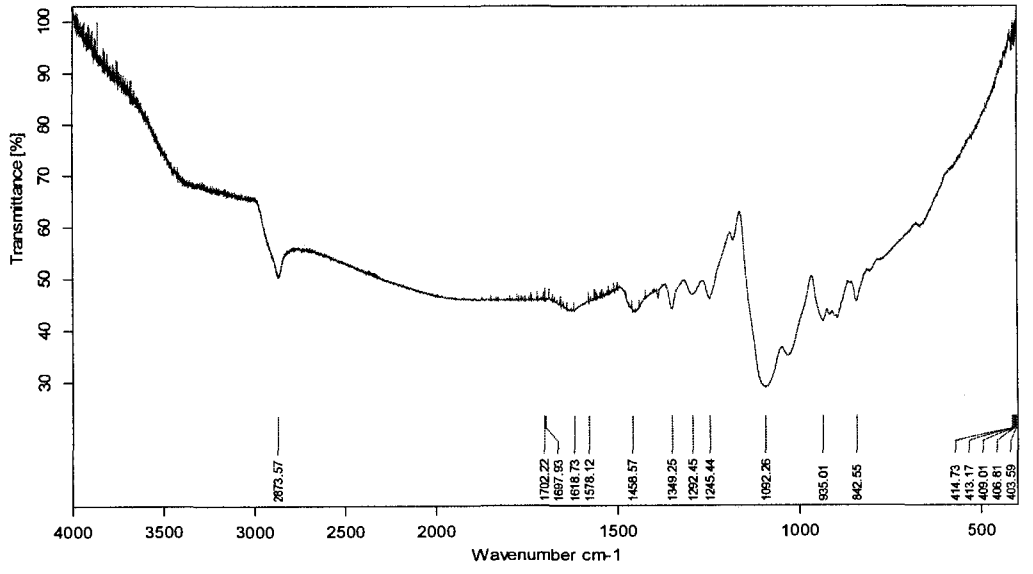

Table 3.2 Significant FT-IR peaks for POMOE/$MoSe_2$ intercalate [79]

Major bond/Group	Wavenumber (cm^{-1})	Band shift (cm^{-1})
CH asymmetric bend	2874	-3
OCH_2 symmetric bend	1459	0
CH_2 symmetric bend	1349	-5
C-O stretch	1292	-9
C-O stretch	1245	-8
C-O-C stretch	1092	-22
CH_2 rocking	935	-17
CH_2 rocking	843	-7

Figure 3.28 FT-IR spectrum of $(POMOE)_{25}LiOTf$

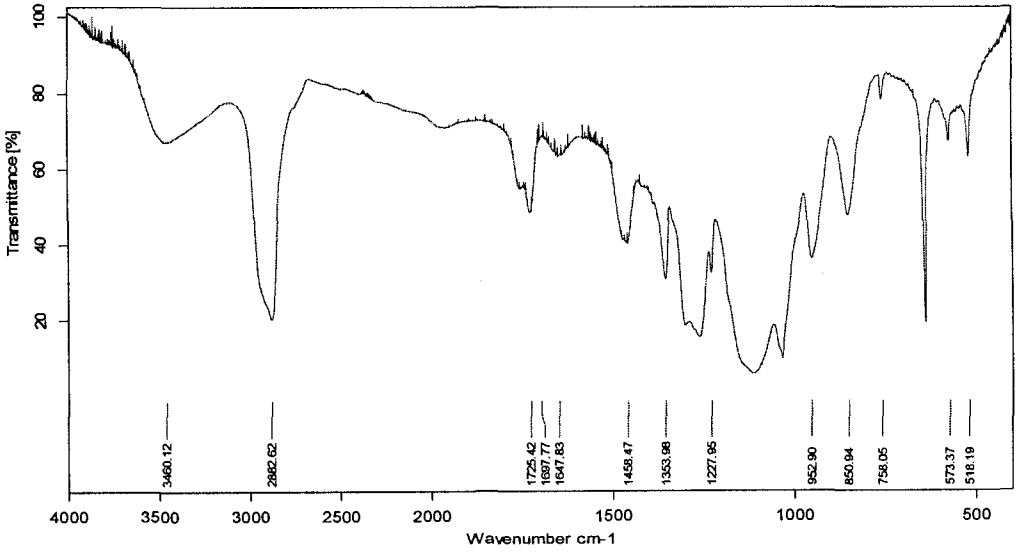

Table 3.3 Significant FT-IR peaks for $(POMOE)_{25}LiOTf$[79-81]

Major bond/Group	Wavenumber (cm^{-1})	Band shift (cm^{-1})
H-bond between OH groups	3450	+109
CH asymmetric bend	2883	-6
C=O stretch	1725	-28
OCH_2 symmetric bend	1458	-1
CH_2 symmetric bend	1354	0
CF_3 stretch	1260	
C-O stretch	1228	-25
C-O-C stretch	1114	0
CH_2 rocking	953	+1
CH_2 rocking	851	+1
C-F deformation (ion-ion interactions)	638	
SO_2 asymmetric bend	573	
SO_2 symmetric bend	518	

Figure 3.29 FT-IR spectrum of $(POMOE)_{25}LiOTf/MoSe_2$ intercalate

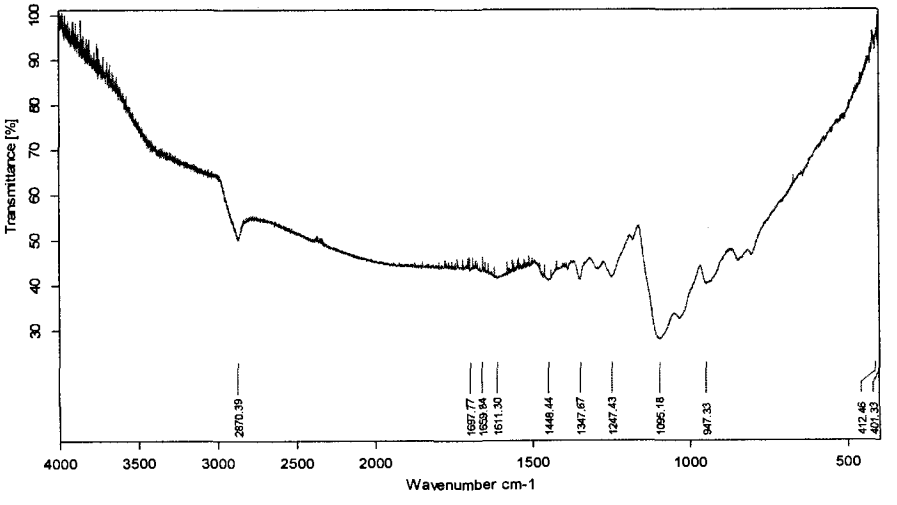

Table 3.4 Significant FT-IR peaks for $(POMOE)_{25}LiOTf/MoSe_2$ intercalate [79-81]

Major bond/Group	Wavenumber (cm^{-1})	Band shift (cm^{-1})
CH asymmetric bend	2870	-7
OCH_2 symmetric bend	1448	-11
CH_2 symmetric bend	1348	-6
C-O stretch	1247	-6
C-O-C stretch	1095	-19
CH_2 rocking	947	-5

POMOE was characterized by differential scanning calorimetry (DSC) (Figure 3.30). The glass transition temperature of POMOE was found to be -66 °C. This is in very good agreement with the literature value (-66±2 °C).[82] The multi endothermic peaks at 6 °C and 12 °C correspond to melting points of the two phases in this copolymer.[75] These data are close to the literature value (5 °C, 13±2 °C) [75, 82] and so are the heats of fusion (49.02 J/g, compared to 50±5 J/g in the literature).[82] The exothermic peak corresponds to the freezing point of the polymer. The difference between the melting point and the freezing point was caused by thermal lag originated by the thermal resistance within the sample, the instrument and the thermal contact between sample container (aluminum pan) and instrument.[83]

Figure 3.30 DSC of POMOE (heating rate: 5 °C/min)

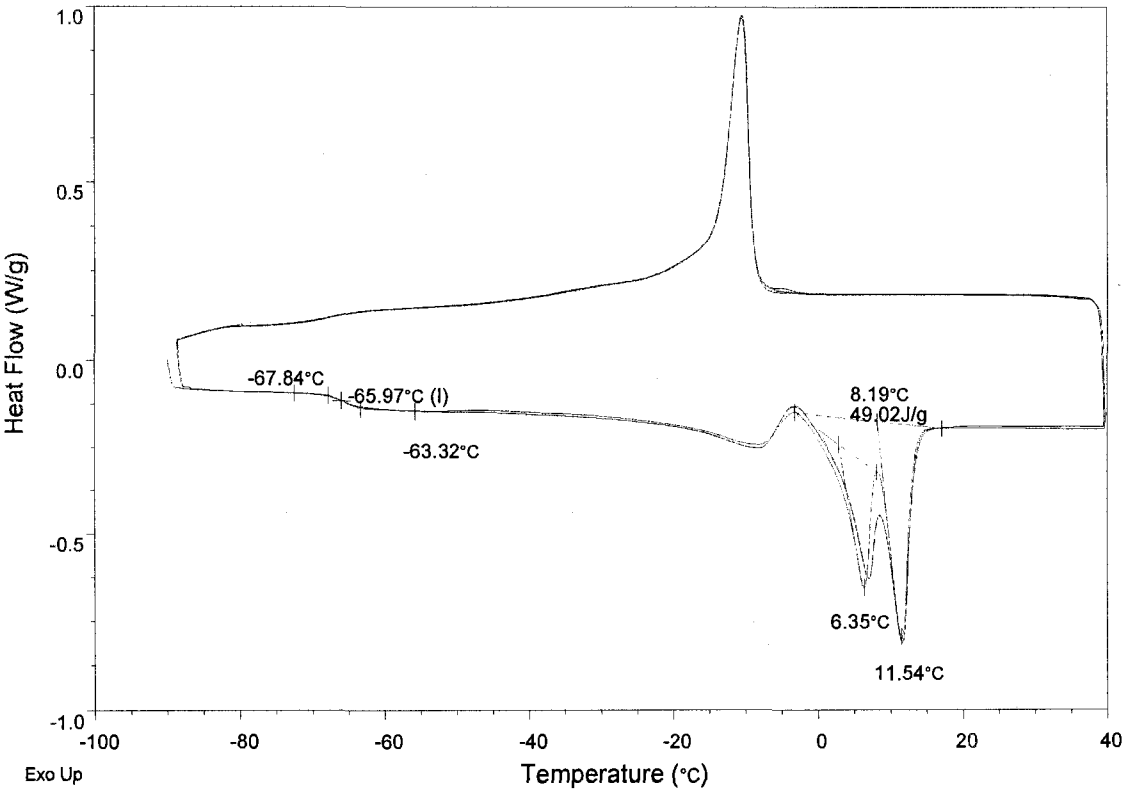

The DSC data of $(POMOE)_{25}LiOTf$ are depicted in Figure 3.31. It is found that upon complexation of POMOE with LiOTf, T_g shifts up to -55 °C, which is close to the value in the literature.[39] However, the melting point was not clearly detected upon the complexation of POMOE with LiOTf.

Figure 3.31 DSC of $(POMOE)_{25}LiOTf$ (heating rate: 5 °C/min)

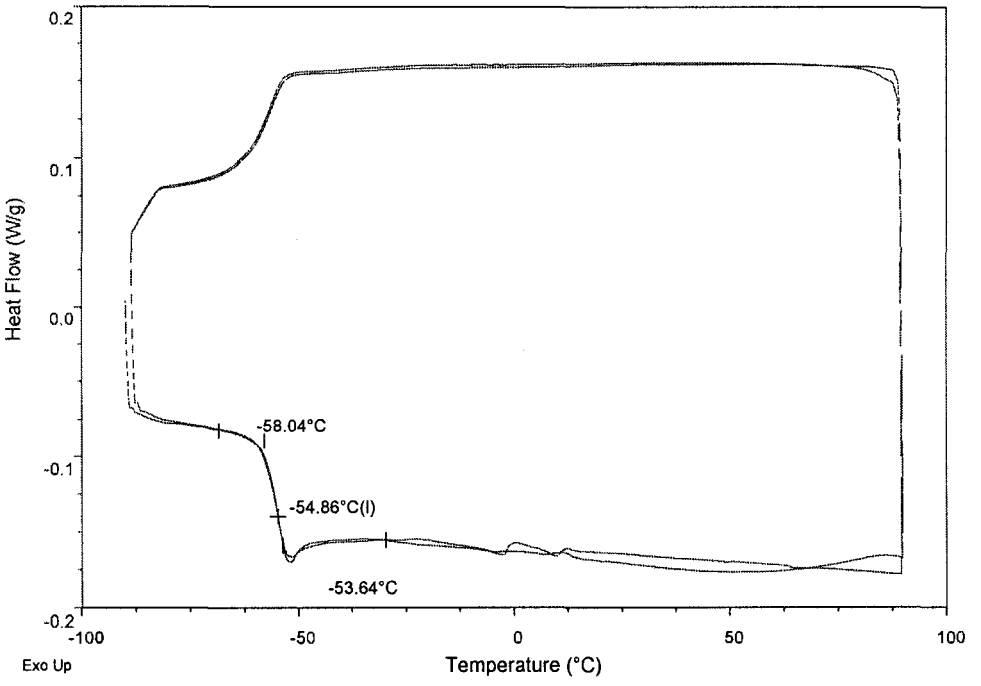

Due to the low mole ratio between POMOE and $MoSe_2$, the DSC of POMOE/$MoSe_2$ intercalate was run in the modulated mode (MDSC) to achieve clearer signals. Both the MDSC of POMOE/$MoSe_2$ intercalate (Figure 3.32) and the DSC of $(POMOE)_{25}LiOTf/MoSe_2$ intercalate (Figure 3.33) show that the T_g of POMOE shifts to a higher temperature, indicating interaction between the polymer and the layered host. In Figure 3.32 and Figure 3.33, the multi endothermic peaks at about 6.5 °C and 12.5 °C correspond to the melting points of the two phases in POMOE.[75] The melting point of ice (at 0 °C) was also detected in the DSC of $(POMOE)_{25}LiOTf/MoSe_2$ intercalate.

Figure 3.32 Modulated DSC of POMOE/$MoSe_2$ intercalate (heating rate: 3 °C/min)

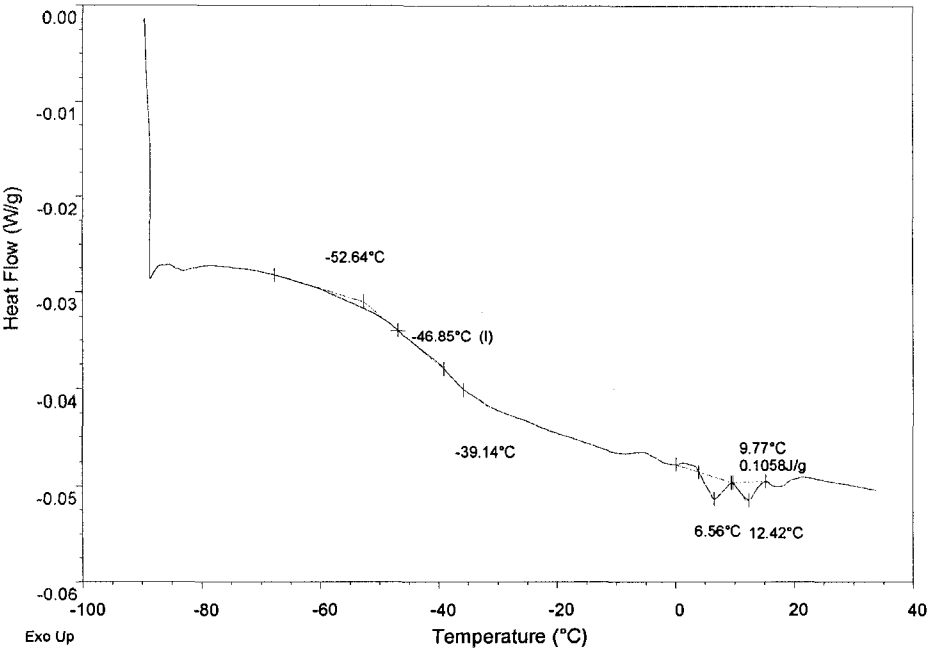

Figure 3.33 DSC of (POMOE)$_{25}$LiOTf/$MoSe_2$ intercalate (heating rate: 5 °C/min)

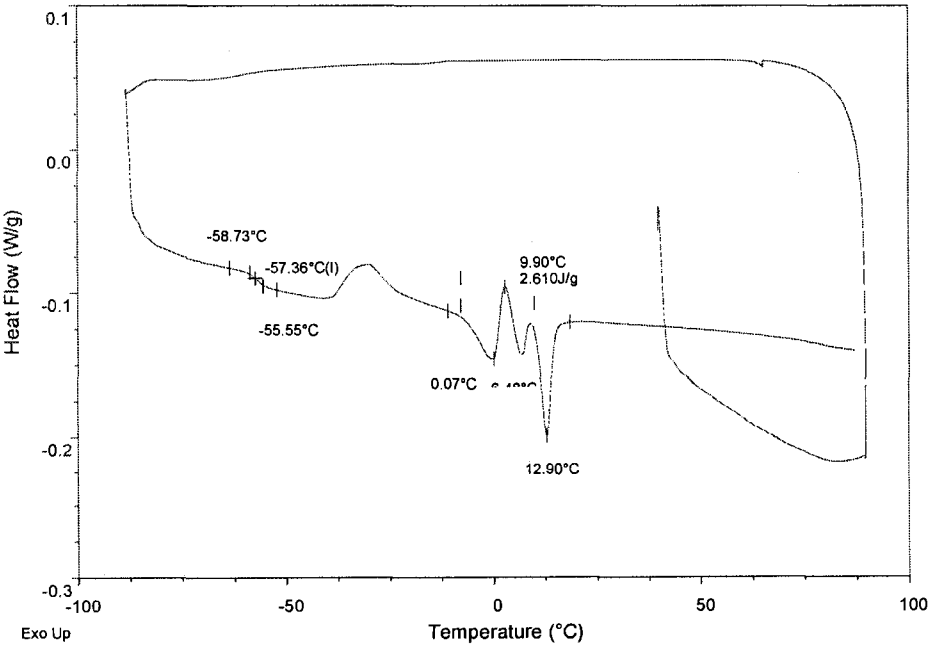

3.6 MEEP/$MoSe_2$ System

3.6.1 Synthesis of MEEP and $(MEEP)_4LiOTf$ complex

MEEP was synthesized following a literature procedure.[41] Five grams of the $PNCl_2$ trimer were charged into a glass tube in the dry box. The tube was then sealed under vacuum. The trimer was heated at 250 °C for 4 hours. The resultant product contains linear poly(dichlorophosphazene) polymer (-[-$PNCl_2$-]-$_n$), cross-linked poly(dichlorophosphazene) and unreacted trimer. The trimer was removed by sublimation under vacuum at 40 °C. The yield of the linear -[-$PNCl_2$-]- $_n$ polymer and cross-linked product was 3.9 g.

Sodium hydride (4g), THF (100 mL) and a stir bar were charged into a round bottom flask (500 mL) in the dry box. Dry 2-(2-methoxy ethoxy) ethanol (25 mL) was syringed into the above solution and the reaction mixture was allowed to stir for 4 hours under nitrogen purge. A light yellow solution of the desired sodium alkoxide was obtained. Finally, this solution of sodium alkoxide was syringed into a mixture of -[-$PNCl_2$-]-$_n$ polymer in 125 mL THF. The mixture was stirred for 24 hours under nitrogen at room temperature and then all volatile materials were removed under reduced pressure. Deionized water was added into the product, and the insoluble part (cross linked $PNCl_2$) was filtered. The linear $PNCl_2$ was purified through dialysis, followed by freeze-drying. The final product was an air stable, viscous honey like brown gel with a yield of 12.6% (1.2 g).

132 mg of MEEP was dissolved in 15 ml of deionized water, and then was added to 18 mg of LiOTf dissolved in 8.2 mL of deionized water, so that the mole ratio of the

polymer to salt was 4:1.[84] The mixture was allowed to stir overnight and then water was removed *via* freeze-drying.

3.6.2 Results and Discussions on MEEP and MEEP/$MoSe_2$ system (NMR, XRD, TGA, FTIR, and DSC)

The ^{1}H NMR spectrum of MEEP and the chain structure interpretation are shown in Figure 3.34. The ^{31}P NMR spectrum of MEEP is shown in Figure 3.35. The chemical shift is -7.1ppm. The results from Figure 3.34 and 3.35 are in good agreement with the literature. [85-86]

Figure 3.34 ^{1}H NMR spectrum of MEEP

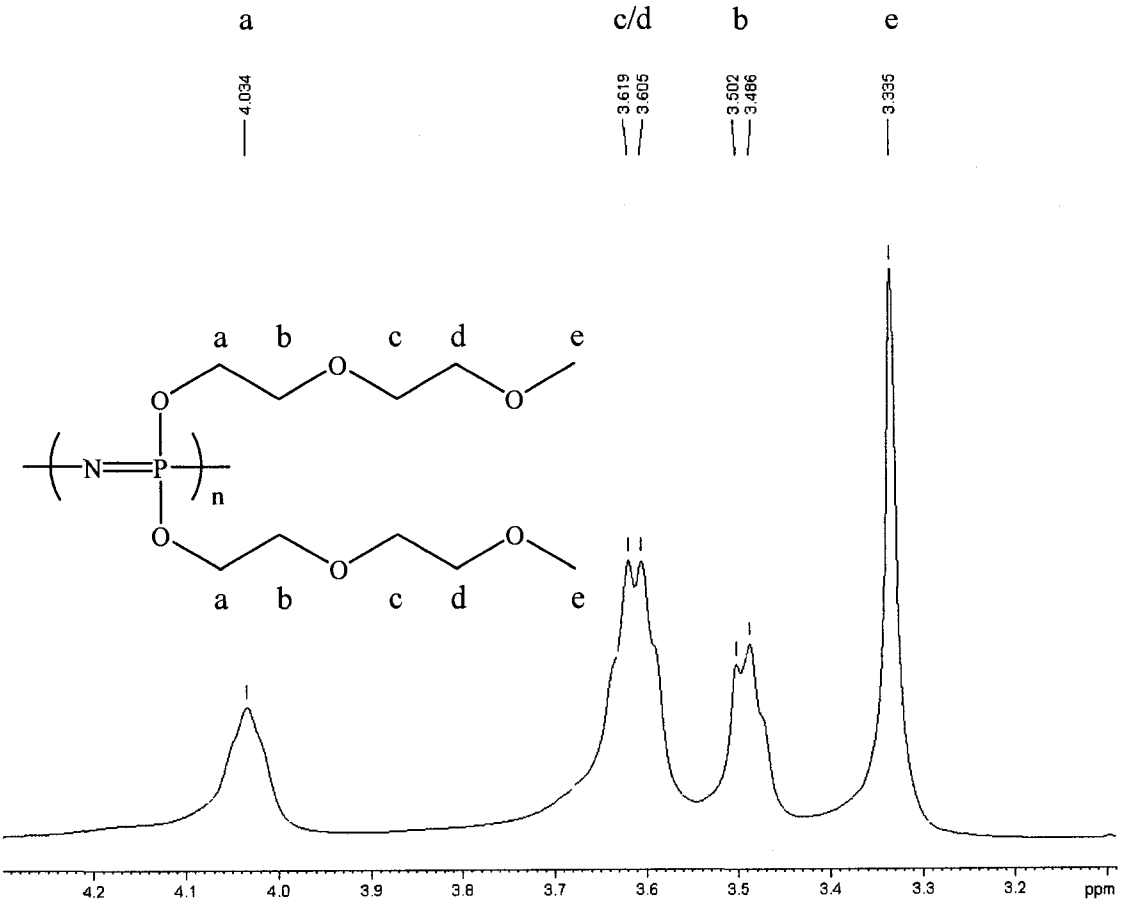

Figure 3.35 ^{31}P NMR spectrum of MEEP

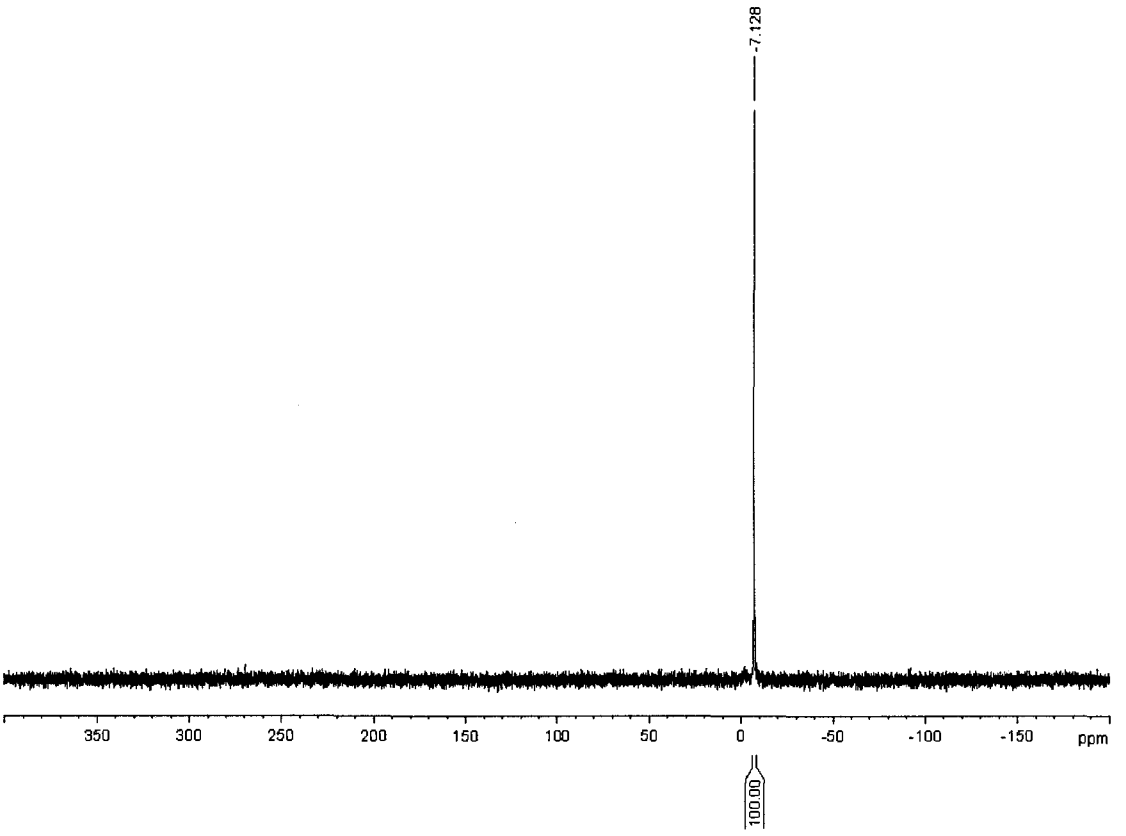

X-ray diffraction patterns of MEEP and MEEP/$MoSe_2$ sandwiched compound are depicted in Figure 3.36 and Figure 3.37, respectively. The broad peaks in Figure 3.36 indicate that MEEP is amorphous. The first three diffraction peaks in Figure 3.37 are clearly visible. The d-spacing of the material was 19.61 Å which corresponds to an inter layer spacing value of 13.19 Å, and this is consistent with having a single layer of the polymer layer chain sandwiched between the $MoSe_2$ sheets as determined by the computational cross section diameter of MEEP (13 Å).[73] This interlayer expansion value is 1.4 Å larger than that observed in MEEP/MoS_2.[51] The difference in interlayer expansion value might be due to the different mole ratio between MEEP and layered hosts, as determined from TGA: $(MEEP)_{0.33}MoS_2$[51] and $(MEEP)_{0.75}MoSe_2$ (See page73).

The difference could also be accounted for by different concentrations of water between the layers. A lower actual mole ratio (0.5 :1) of the repeat unit of MEEP to MoS_2 was used in reference 51. Different concentrations of the polymer may affect the conformation of the polymer between the layers. The intensity of the intercalated compound was very high, indicating that MEEP helps to re-stack the $MoSe_2$ layers. The crystallite size was 104 Å as determined by the Scherrer equation. The mole ratio of $MoSe_2$ to the repeat unit of MEEP used in the reaction was 1:0.83.

Figure 3.36 XRD spectrum of MEEP

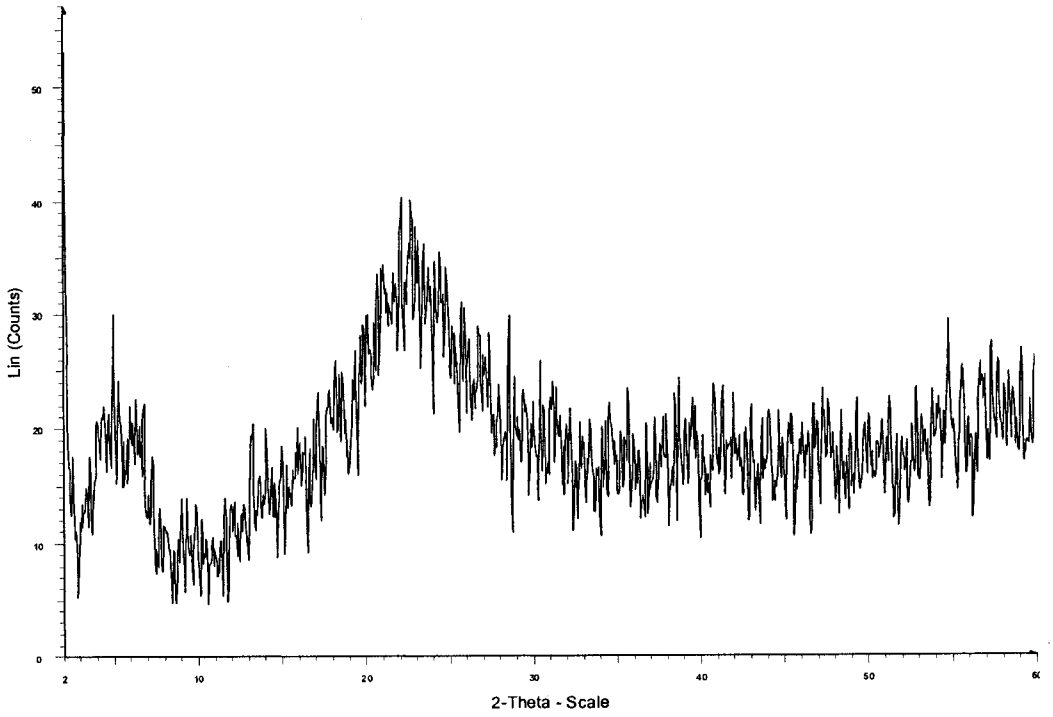

Figure 3.37 XRD spectrum of MEEP/$MoSe_2$ intercalate (0.83 : 1 mole ratio)

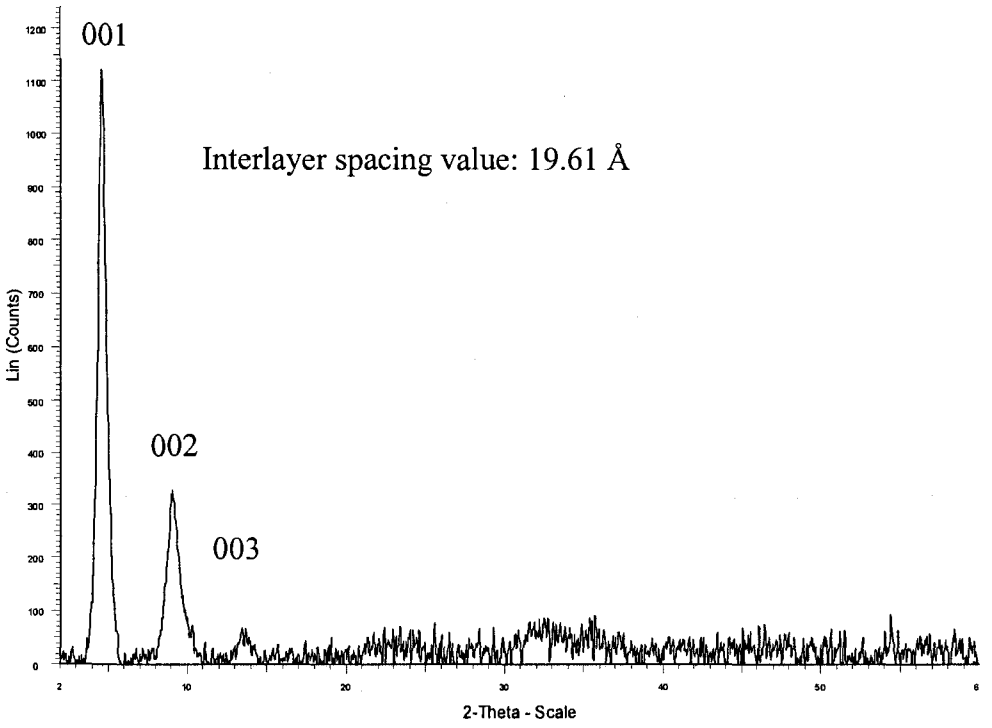

X-ray diffraction patterns of $(MEEP)_4LiOTf$, and $(MEEP)_4LiOTf/MoSe_2$ sandwiched compound are depicted in Figure 3.38 and Figure 3.39, respectively. Compared with the lithium triflate (Figure 3.21), the MEEP salt complex is amorphous (Figure 3.38). The absence of peaks from LiOTf and the presence of the new broad peaks indicate that all of the salt has been complexed with the polymer. The powder pattern of $(MEEP)_4$ $LiOTf/MoSe_2$ is similar to that of $MEEP/MoSe_2$ (Figure 3.37).

Figure 3.38 XRD spectrum of $(MEEP)_4$ LiOTf

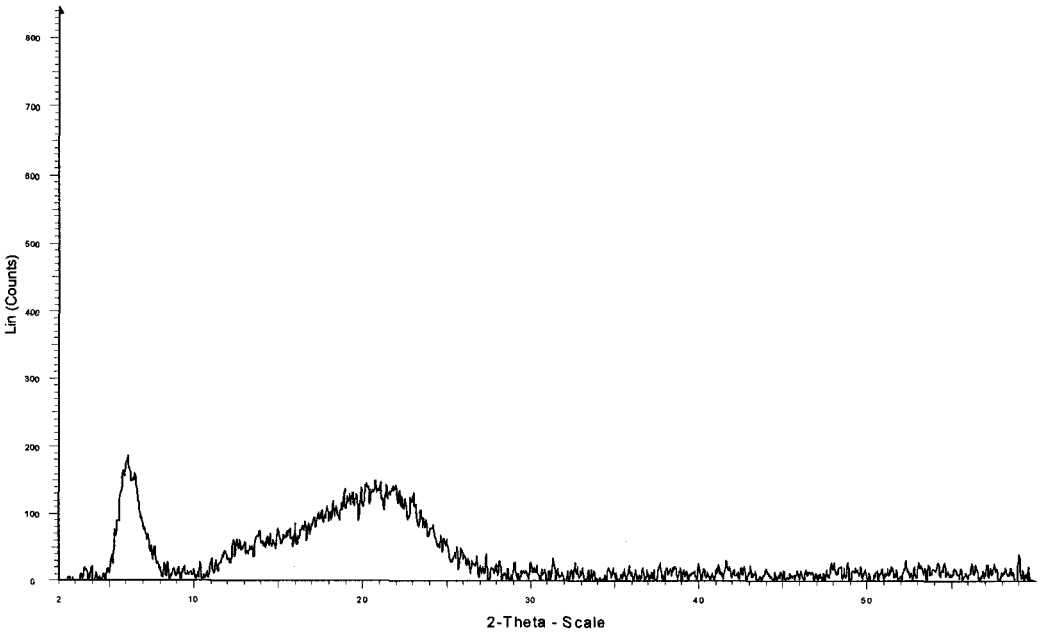

Figure 3.39 XRD spectrum of $(MEEP)_4$LiOTf/$MoSe_2$ intercalate (0.8:1 mole ratio)

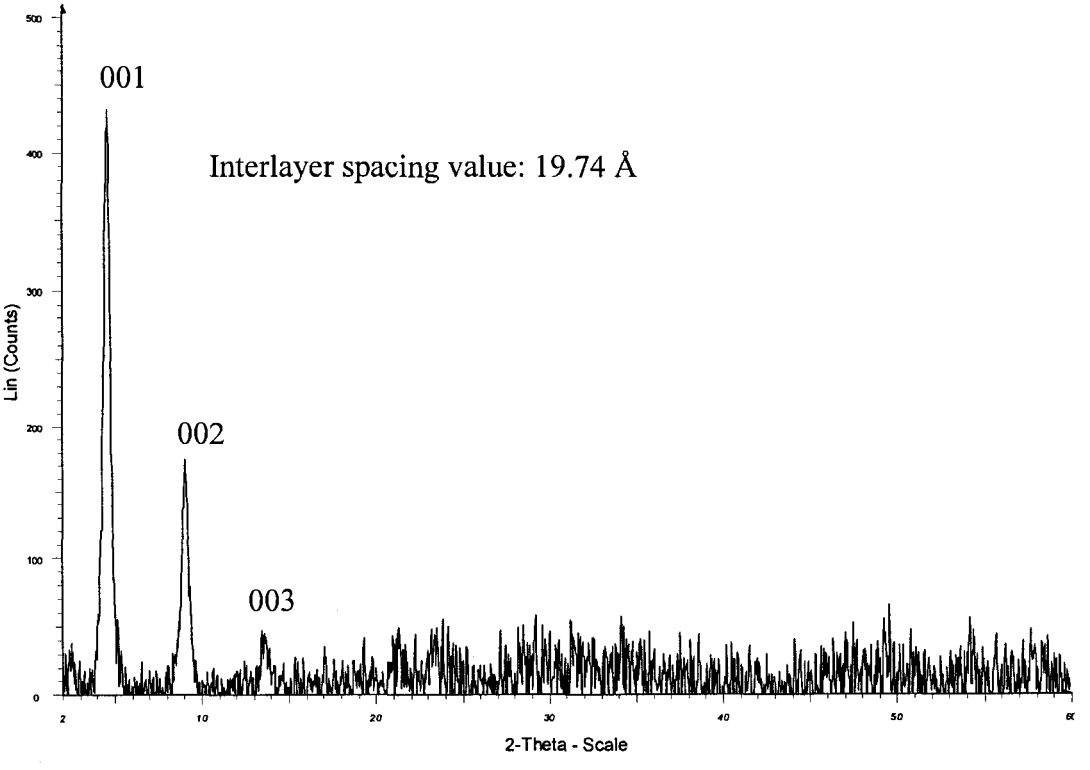

To protect the thermocouple, TGA of pristine MEEP (Figure 3.40) and MEEP/$MoSe_2$ composite (Figure 3.41) were run under nitrogen atmosphere. In Figure 3.40, MEEP decomposes at 234 °C in nitrogen and there is only 10% of the sample left at 1000°C. In Figure 3.41, the MEEP/$MoSe_2$ composite decomposes at 235 °C also, and reaches a plateau at 450 °C, which suggests that MEEP sandwiched between $MoSe_2$ layers decomposes faster than pristine MEEP. The calculated composition is $(MEEP)_{0.75}MoSe_2$, which is close the mole ratio used in the reaction: $(MEEP)_{0.83}$/ $MoSe_2$.

Figure 3.40 TGA of MEEP in nitrogen

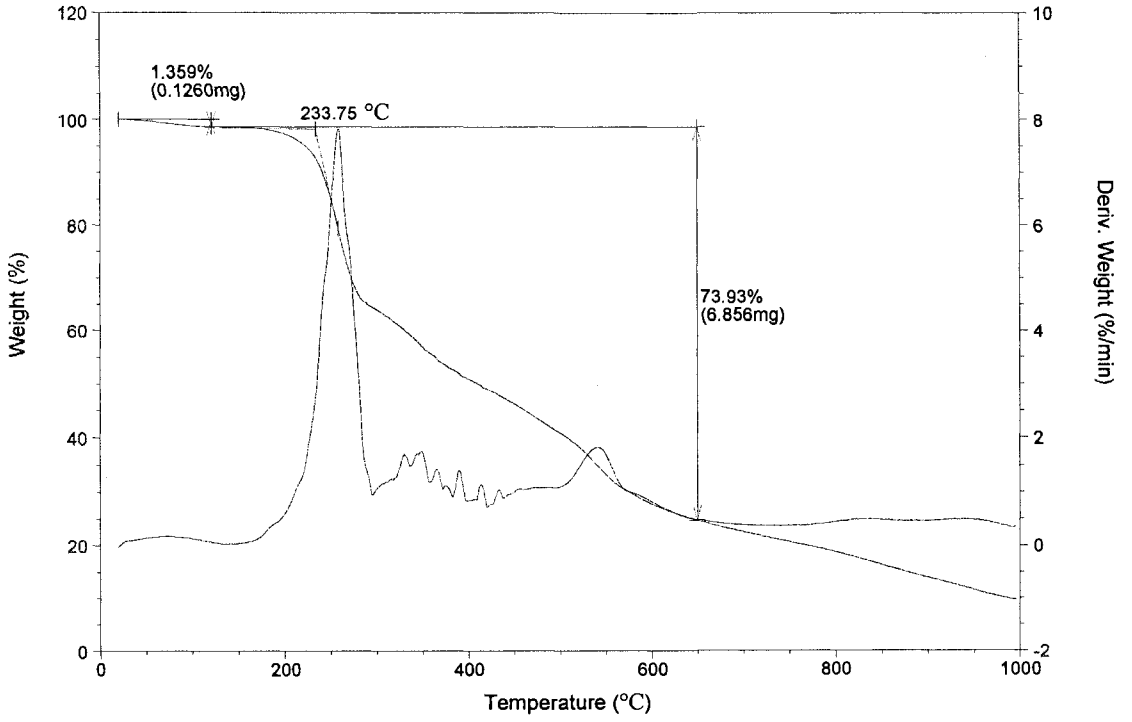

Figure 3.41 TGA of MEEP/$MoSe_2$ intercalate in nitrogen

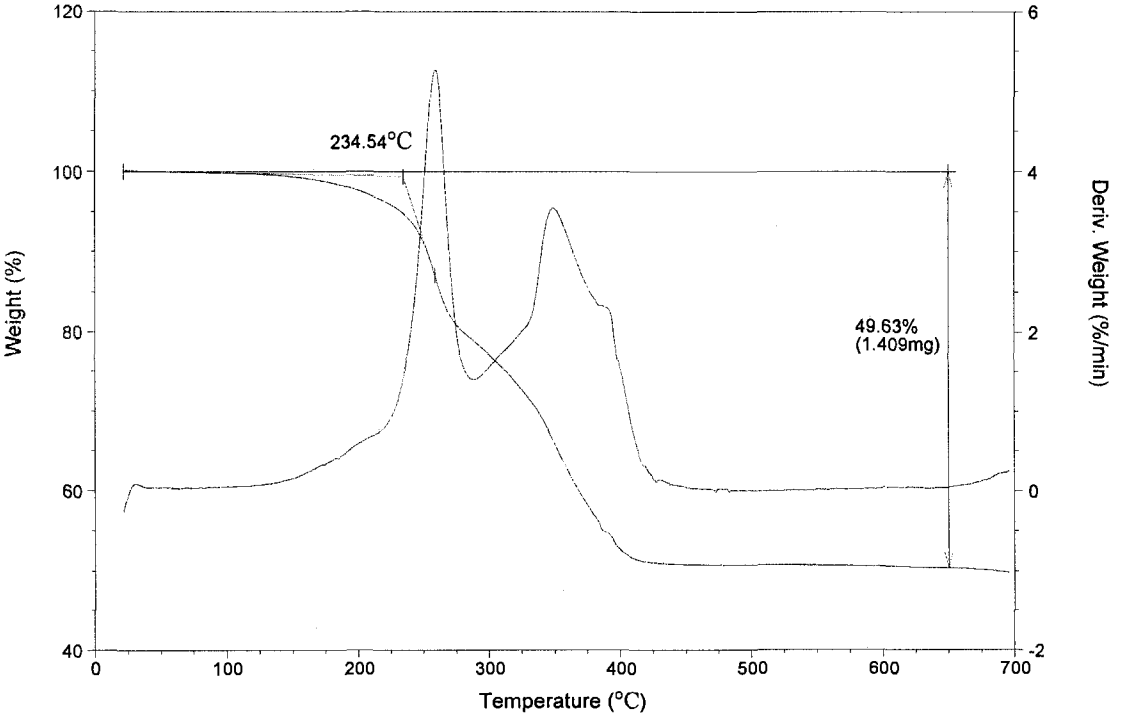

IR spectrum of pristine MEEP is shown the Figure 3.42 and the vibrations are summarized in the Table 3.5 below.

Figure 3.42 FT-IR spectrum of MEEP

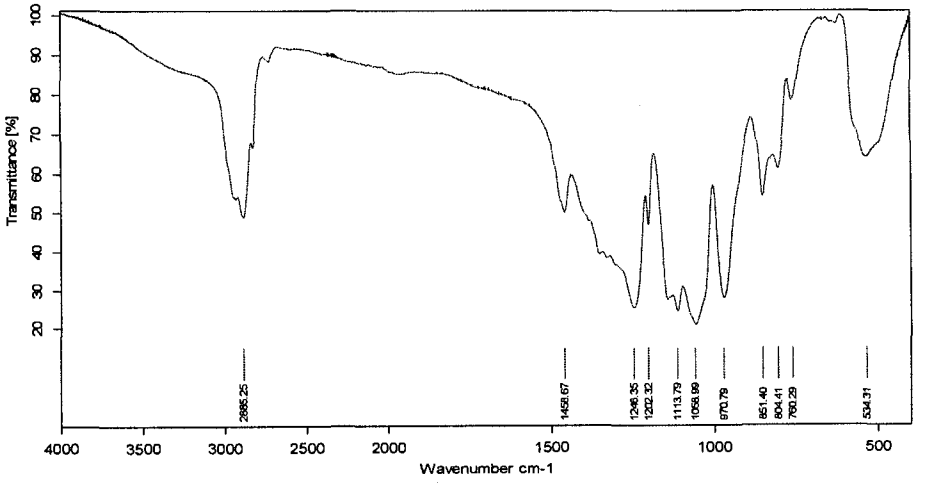

Table 3.5 Significant FT-IR peaks for MEEP [87-88]

Major bond/group	Wavenumber (cm^{-1})
CH asymmetric bend	2885
OCH_3 symmetric bend	1459
P=N stretch and POC bend	1246
COC stretch	1114
POC stretch	1059
POC deformation and COC bending	971
CH_2 rocking	851
PNP skeletal	804
PNP skeletal	760
OCC bending	534

FT-IR spectrum of the MEEP/$MoSe_2$ nanocomposite is shown in Figure 3.43. The band associated with asymmetric C-H bending is resolved into two well-defined bands at 2926 and 2858 cm^{-1} when the polymer is inserted. This behavior is ascribed to the interaction between oxygen atoms in the polymer and interlayer cations (Li^+ from $Li_{0.7}MoSe_2$).[89] The wavenumbers of P=N stretching and POC bending modes are red shifted down to 1235 cm^{-1}, COC stretching shifts down to 1108 cm^{-1}, POC stretching shifts down to 1049 cm^{-1}, POC deformation and COC bending shifts down to 956 cm^{-1}, PNP skeletal shift down to 799 cm^{-1}, and OCC bending shifts down to 501 cm^{-1}. The red shifts might be due to the confinement of the polymer within the gallery space of the host. When MEEP/salt complex was inserted into $MoSe_2$ the major IR bands shifted to lower wavenumbers too (Figure 3.45). In addition, the intensity of most peaks was diminished (Figure 3.44, Figure 3.45).

Figure 3.43 FT-IR spectrum of MEEP/$MoSe_2$ intercalate

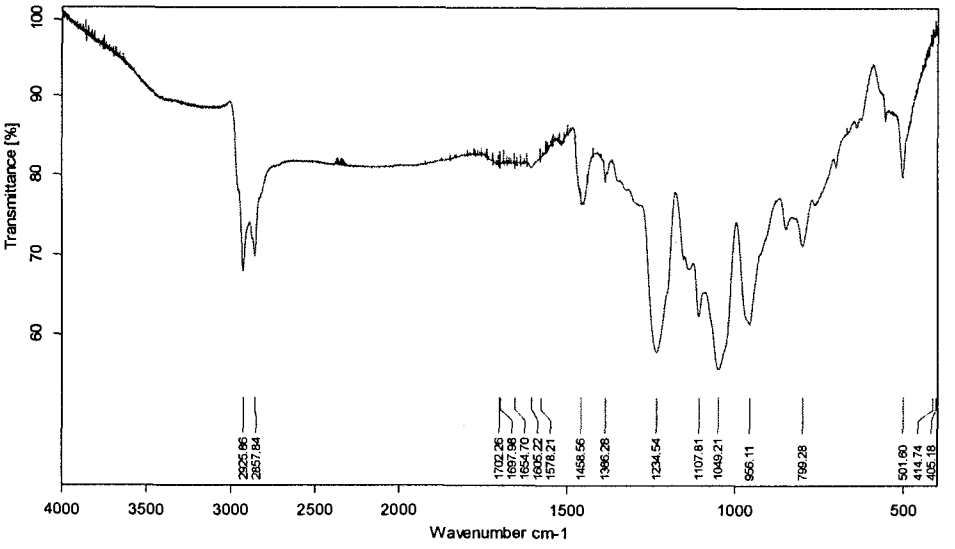

Table 3.6 Significant FT-IR peaks for MEEP/$MoSe_2$ intercalate [87-88]

Major bond/group	Wavenumber (cm^{-1})	Band shift (cm^{-1})
CH asymmetric bend	2926	
CH asymmetric bend	2858	-27
OCH_3 symmetric bend	1459	0
P=N stretch and POC bend	1235	-11
COC stretch	1108	-6
POC stretch	1049	-10
POC deformation and COC bending	956	-15
PNP skeletal	799	-5
OCC bending	501	-33

Figure 3.44 FT-IR spectrum of $(MEEP)_4$ LiOTf

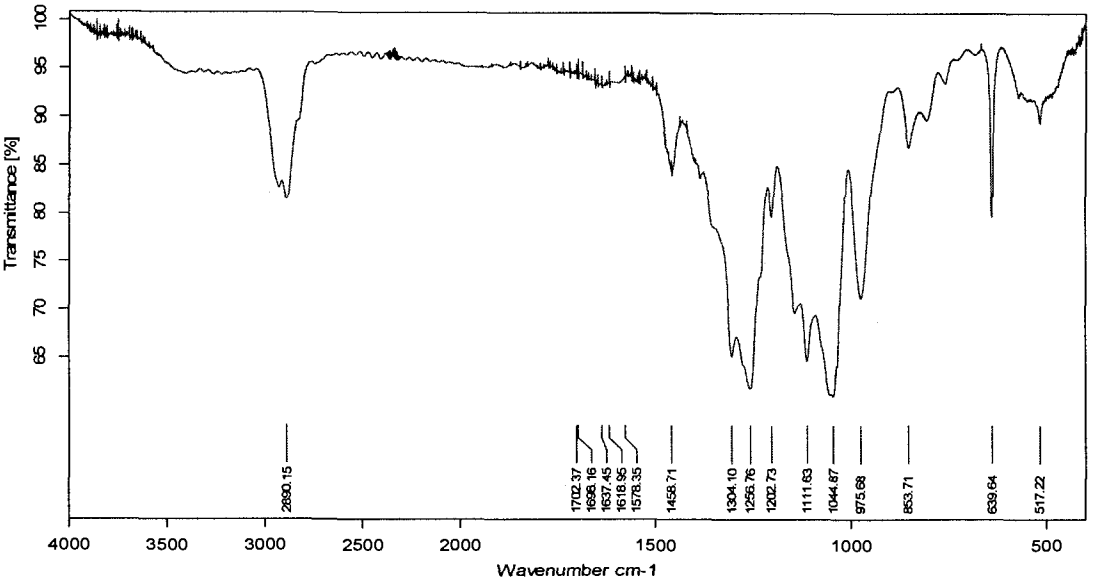

Table 3.7 Significant FT-IR peaks for $(MEEP)_4LiOTf$[87-88]

Major bond/group	Wavenumber (cm^{-1})	Band shift (cm^{-1})
CH asymmetric bend	2890	+5
OCH_3 symmetric bend	1459	0
P=N stretch and POC bend	1257	-11
COC stretch	1112	-2
POC stretch	1045	-14
POC deformation and COC bending	976	+5
CH_2 rocking	854	+3
PNP skeletal	804	0
PNP skeletal	760	0
C-F deformation (ion-ion interactions)	640	
SO_2 symmetric bend and OCC bending	517	

Figure 3.45 FT-IR spectrum of $(MEEP)_4LiOTf/MoSe_2$ intercalate

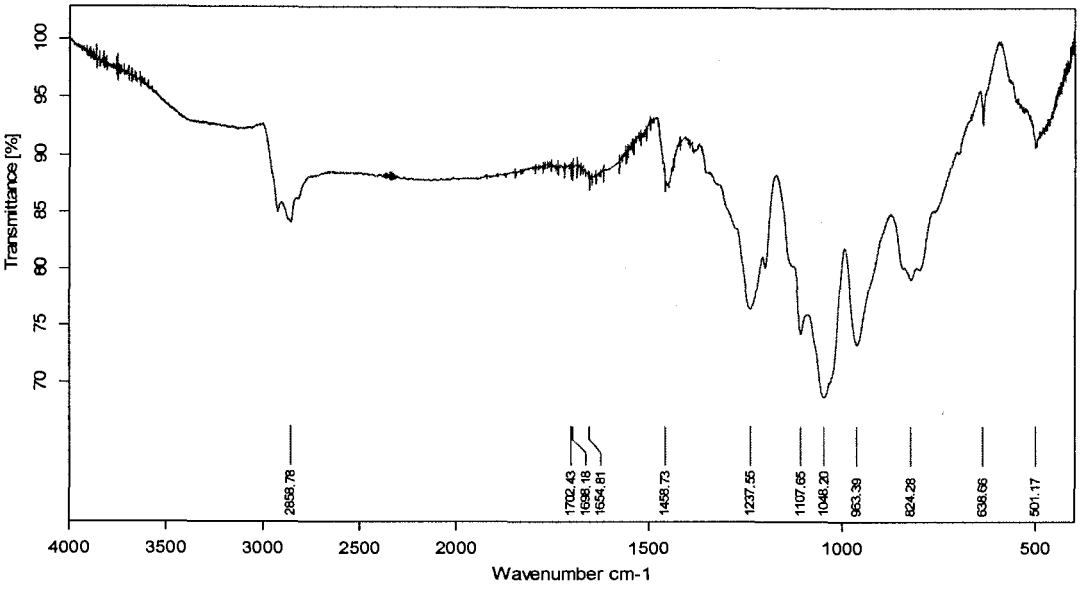

Table 3.8 Significant FT-IR peaks for $(MEEP)_4LiOTf/MoSe_2$ intercalate [87-88]

Major bond/group	Wavenumber (cm^{-1})	Band shift (cm^{-1})
CH asymmetric bend	2859	26
OCH_3 symmetric bend	1459	0
P=N stretch and POC bend	1238	-8
COC stretch	1108	-6
POC stretch	1048	-11
POC deformation and COC bending	963	-8
CH_2 rocking	824	-27
C-F deformation (ion-ion interactions)	639	-1
SO_2 symmetric bend and OCC bending	501	-16, -31

The T_g of pure MEEP is -80 °C (Figure 3.48). When MEEP was complexed with lithium triflate with a mole ratio of 4:1, the T_g shifts up to -69 °C (Figure 3.46). The above data are very close to the results in the literature.[90] (T_g of MEEP: -85 °C, T_g of $(MEEP)_4$ LiOTf: -70 °C).

Figure 3.46 DSC of MEEP (heating rate: 5°C/min)

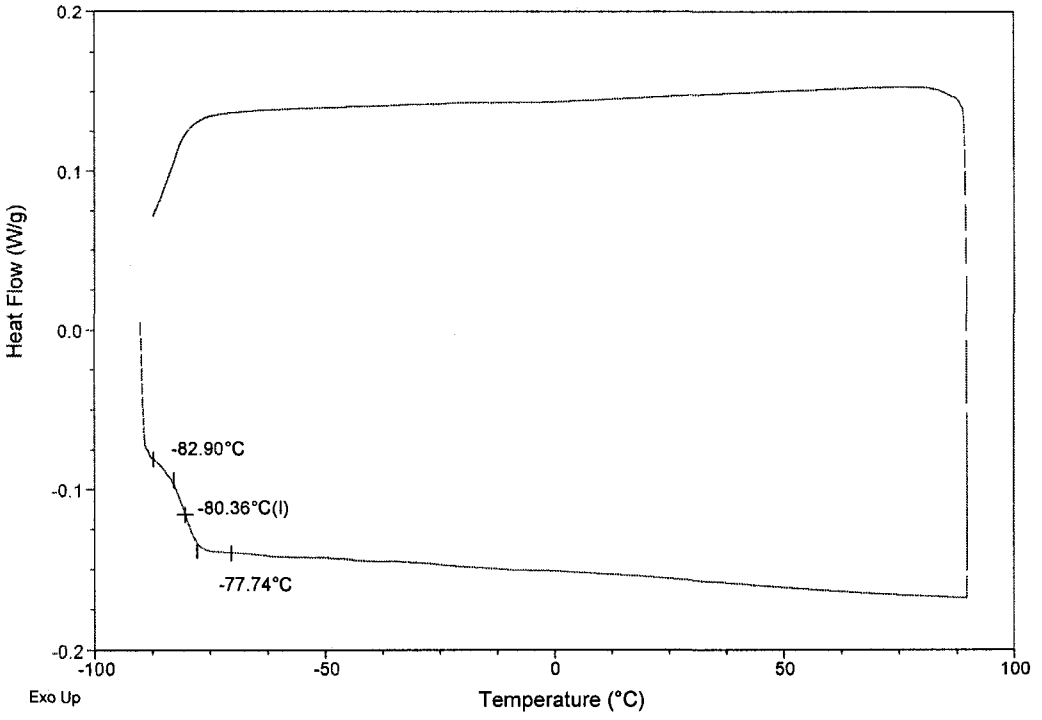

Figure 3.47 DSC of LiOTf/MEEP$_4$ (heating rate: 5°C/min)

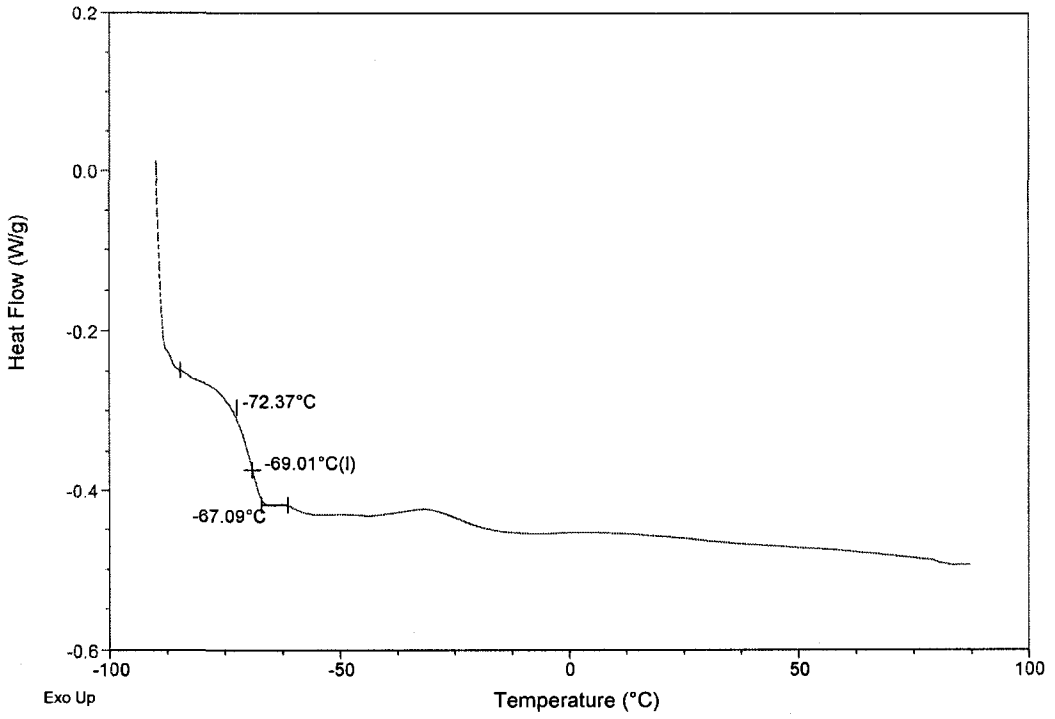

The DSC of MEEP/$MoSe_2$ structure is shown in Figure 3.48. When MEEP was inserted into $MoSe_2$ layers, the T_g, which is not clearly discernable, shifts to a higher temperature (-52 °C) compared with that of the pristine MEEP. (Modulated DSC did not show clearer spectrum for the MEEP/$MoSe_2$ composite). The absence or increasing of T_g might be due to the host-guest interaction, i.e. the mobility of polymer is confined by the layered host.[91]

Figure 3.48 DSC of MEEP/$MoSe_2$ intercalate (heating rate: 5°C/min)

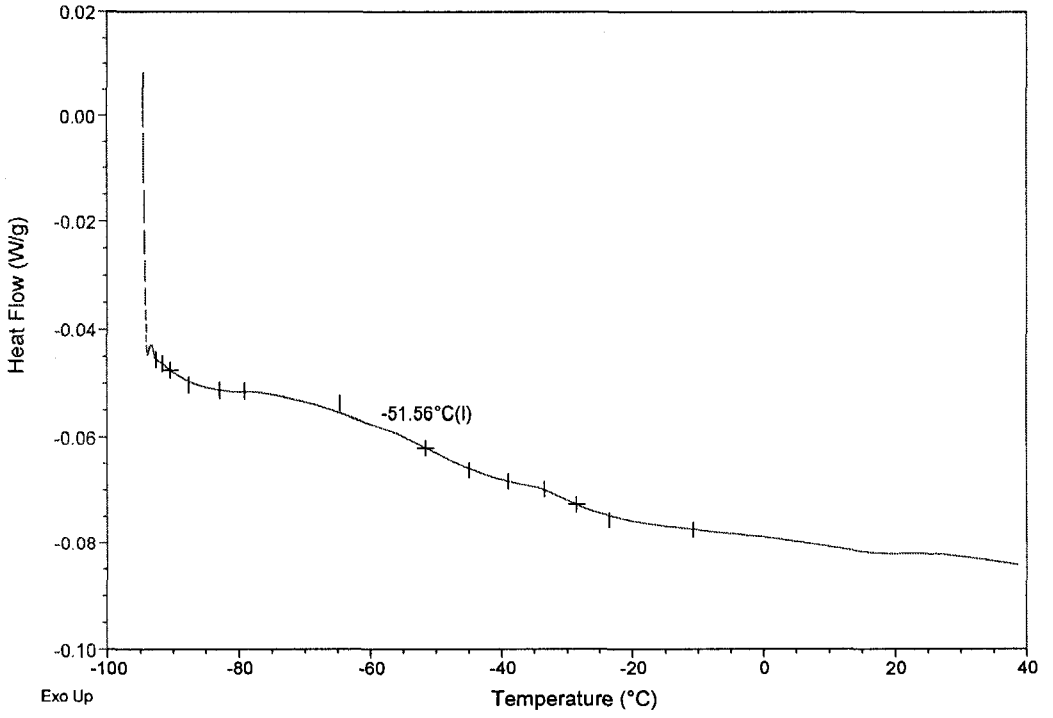

Because regular DSC did not show a clear T_g for $(MEEP)_4LiOTf/MoSe_2$ sandwiched structure, modulated DSC was used (Figure 3.49). The T_g of MEEP in $(MEEP)_4LiOTf/MoSe_2$ sandwiched structure is -35 °C higher than that of $(MEEP)_4LiOTf$ itself, due to the host-guest interaction. LiOTf might make this DSC plot clearer than that of $MEEP/MoSe_2$ intercalates. A similar phenomenon was observed between pure MEEP and $(MEEP)_4$/LiOTf complex. (Figure 3.47 and Figure 3.48)

Figure 3.49 MDSC of $(MEEP)_4LiOTf/MoSe_2$ intercalate (heating rate: 3°C/min)

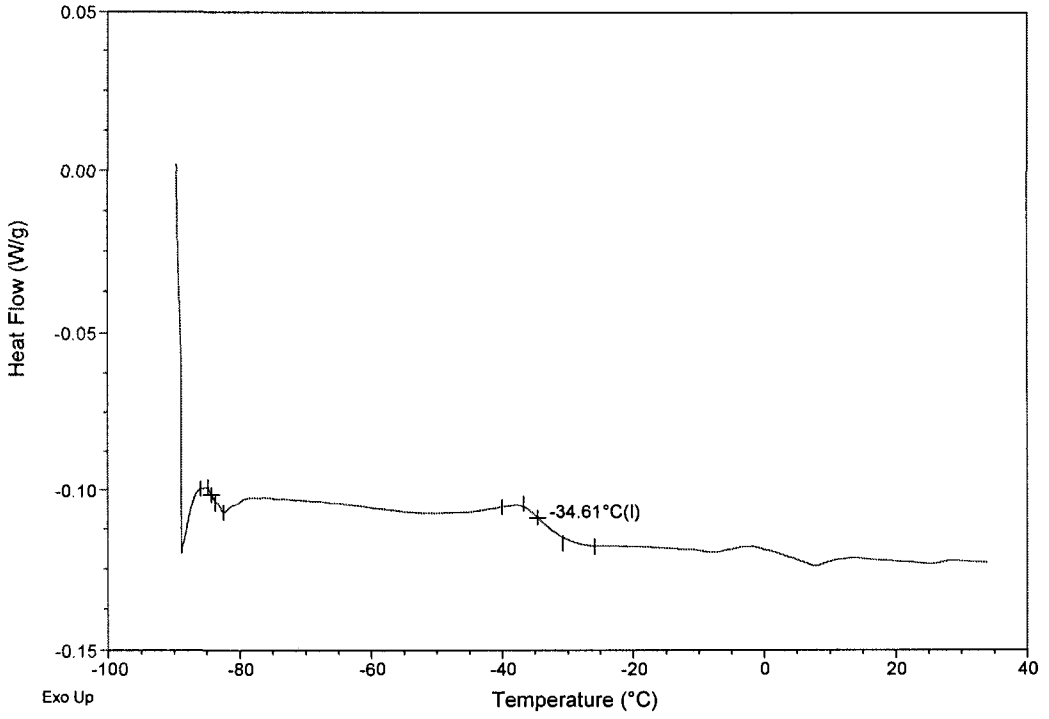

3.6.3 Ionic conductivity of $MEEP/MoSe_2$ system

Ionic conductivity measurements were run by using Alternating Current (AC) Impedance Spectroscopy with a Solartron 1250 response analyzer in Dr. Douglas Dahn's lab in the Department of Physics at UPEI.

Samples of MEEP and $(MEEP)_4LiOTf$ were prepared on a glass slide painted by stainless steel electrodes. A solution of MEEP or $(MEEP)_4LiOTf$ complex was cast between the electrodes connected to wires. To make sure that humidity has no effect on the conductivity, the samples were freeze-dried before the measurements were performed, under vacuum. The sample preparation of $(MEEP)_4LiOTf/MoSe_2$ was similar to that of other layered systems[42] (see Figure 3.50). Freeze-dried powders of

$(MEEP)_4LiOTf/MoSe_2$ intercalate were pressed into a tablet which was then inserted between a pair of stainless steel dies and placed in a sample holder. A spring was then placed between the die and the bolt on one side. When the bolts were screwed into the sample holder, the pressure applied on the stainless steel electrodes will ensure good contact with the sample. High-vacuum silicon grease was added in the threads and around the bolts to block moisture from the environment. Electrodes from the AC impedance analyzer were then connected to the bolts and the measurements were started.

Figure 3.50 Sample Holder for Ionic Conductivity Measurements of $(MEEP)_4LiOTf/MoSe_2$ intercalate [42]

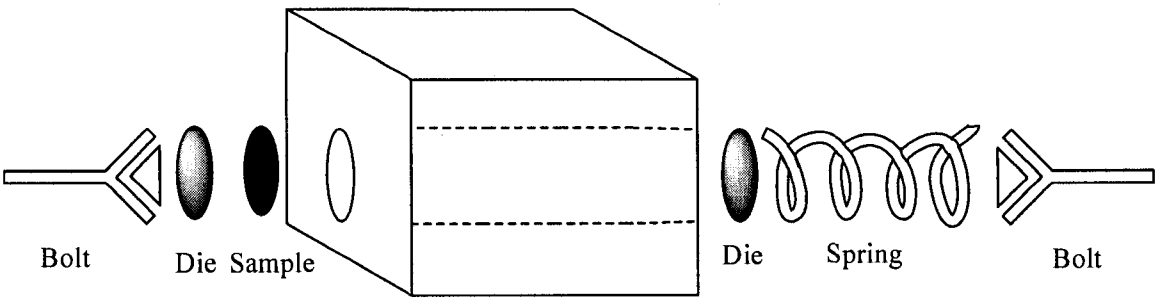

The raw impedance data of MEEP, $(MEEP)_4$/LiOTf complex and $(MEEP)_4LiOTf/MoSe_2$ intercalates are shown in Figures 3.51, 3.52 and 3.53, respectively.

Figure 3.51 Nyquist Plot of MEEP at 300K.

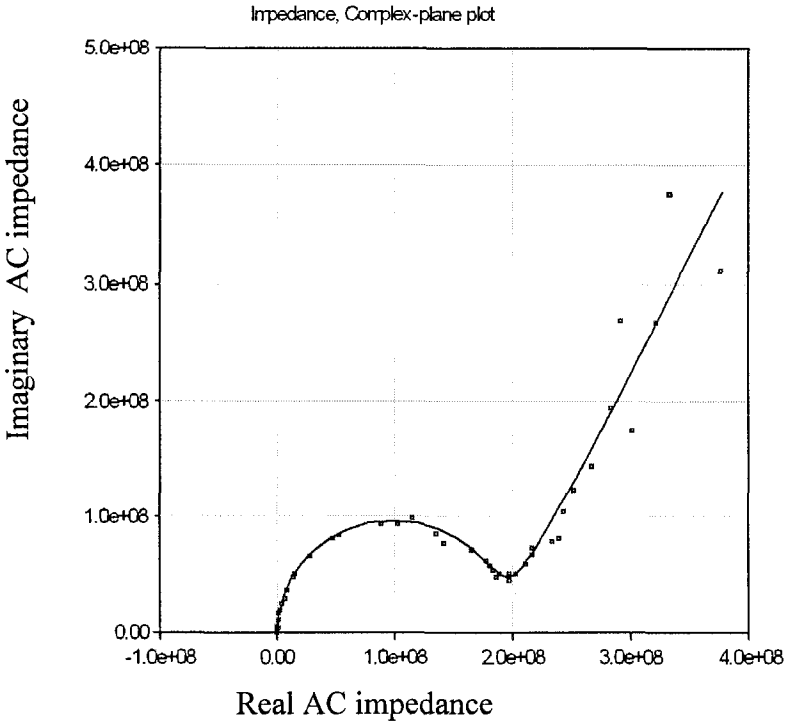

Figure 3.52 Nyquist Plot of $(MEEP)_4LiOTf$ at 300 K

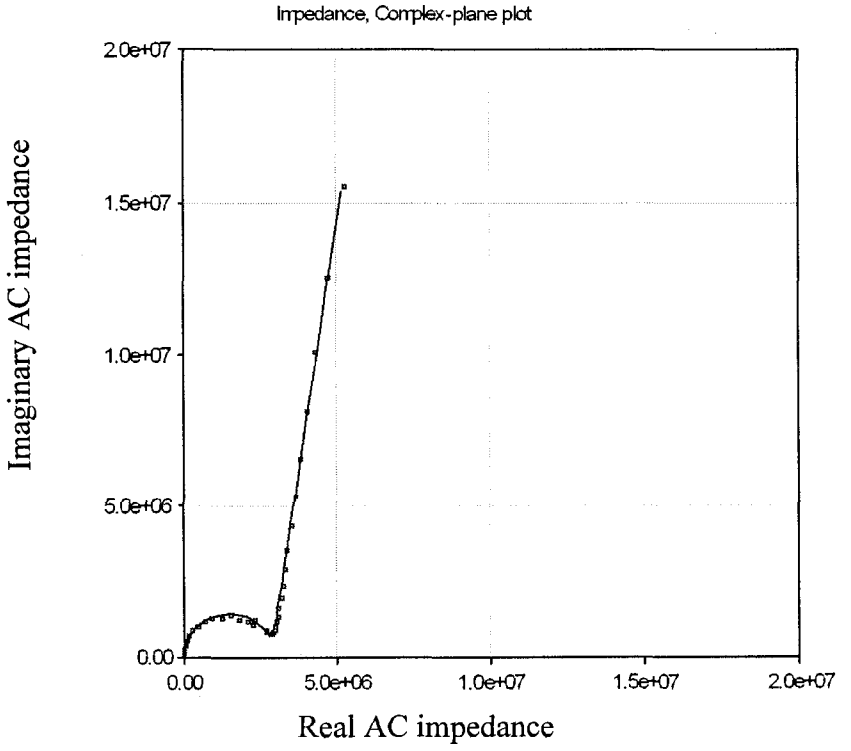

Figure 3.53 Nyquist Plot of (MEEP)$_4$LiOTf/MoSe$_2$ intercalate at 300K

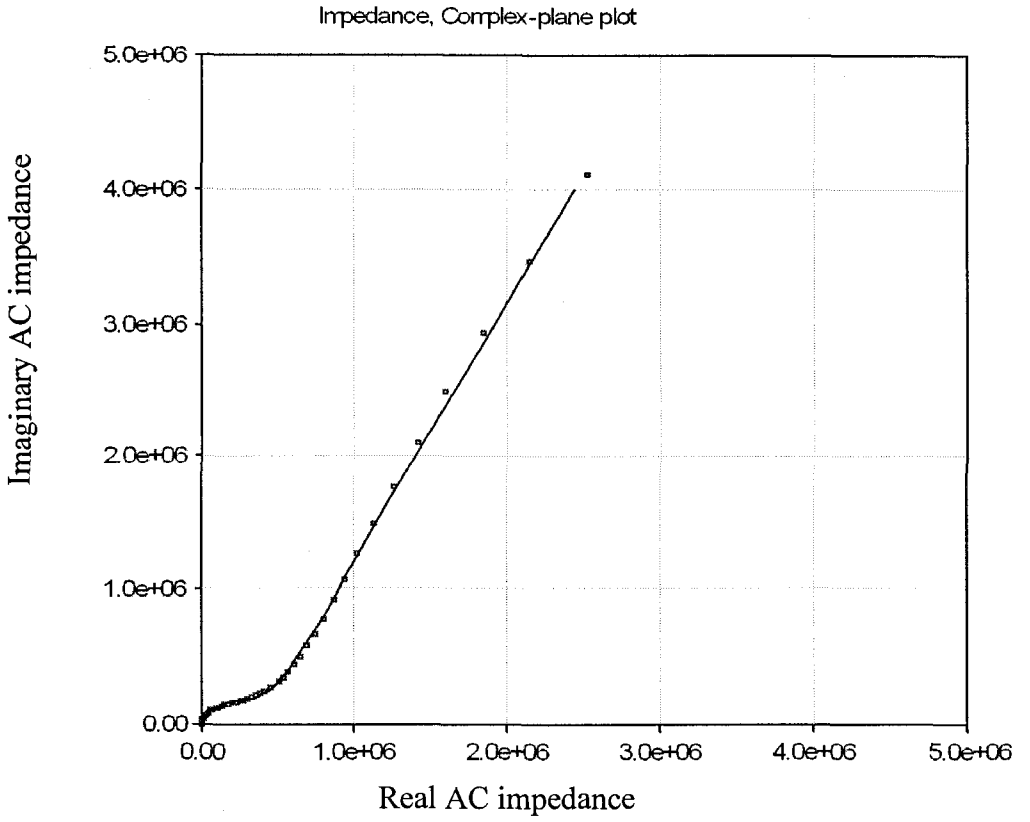

These data were then fit into an equivalent electrical circuit through a computer program, which creates an electrical circuit imitating the ionic conductivity behaviour of the material. From this circuit the bulk resistance of the sample can be acquired and the resistivity is calculated from the geometry of the sample.

The measurement of ionic conductivity can be carried out at different temperatures. A group of resistivities as a function of temperature are obtained by repeating the process and the conductivities can be achieved by taking the reciprocals.[36]

From these data (Figure 3.54) the room temperature ionic conductivity of MEEP, (MEEP)$_4$LiOTf complex and (MEEP)$_4$LiOTf /MoSe$_2$ intercalate were found to be $2.7\text{x}10^{-7}$ S/cm, $2.0\text{x}10^{-5}$ S/cm and $7.89\text{x}10^{-8}$ S/cm, respectively. The conductivity value

of $(MEEP)_4LiOTf$ was lower than the literature value (4×10^{-4} S/cm)[91] and this is due to difference in the sample preparation and sample measurements. For example, difference in purity of the polymer or salt as well as moisture will affect the results. The value from $(MEEP)_4LiOTf/MoSe_2$ intercalate was too low to be qualified as electrolyte and this is due to the fact that the mole ratio between $(MEEP)_4LiOTf$ and $MoSe_2$ was too low [$(MEEP)_4LiOTf/MoSe_2$ =0.8:1].

Figure3.54 Arrhenius Plot of MEEP, $(MEEP)_4$/LiOTf complex and $(MEEP)_4$LiOTf/$MoSe_2$ intercalate

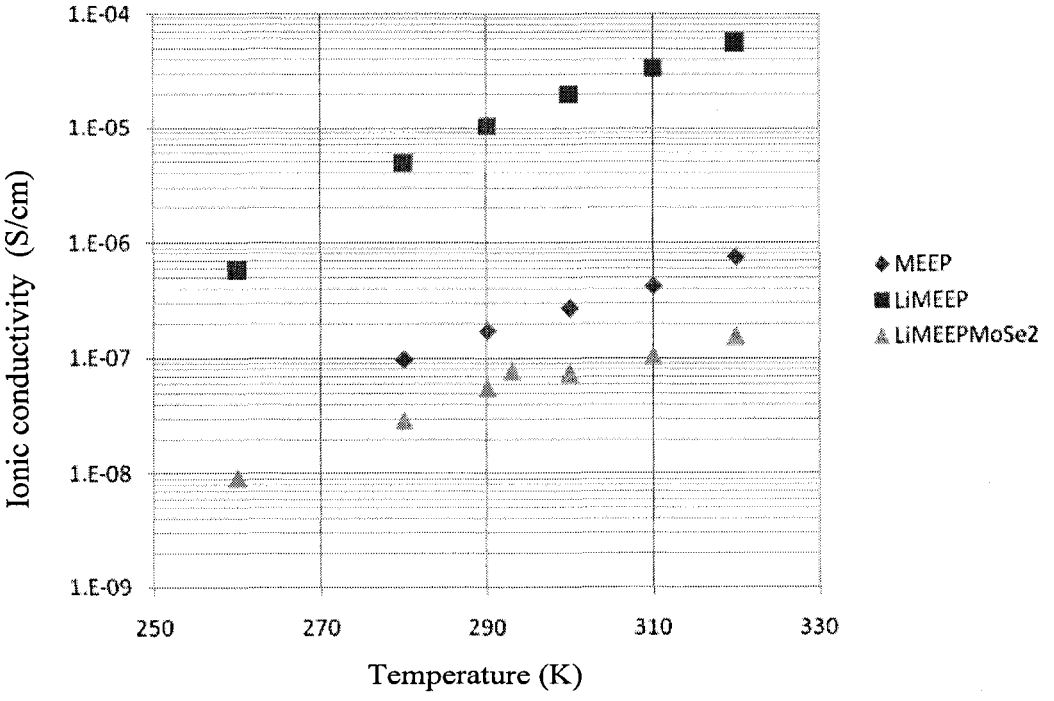

3.7 Results and Discussions on SPE/$MoSe_2$ system

In this chapter, solid polymer electrolytes have been successfully intercalated into $MoSe_2$ based on evidence from the XRD spectra. Compared with the SPE/MoS_2 system, similar interlayer expansion values were observed for the SPE/$MoSe_2$ system. However, SPE/$MoSe_2$ is more stable than SPE/MoS_2.[49, 51, 72] This might be due to the different sample purification for the two systems. To make sure that all of the unintercalated polymers were washed away, extra water was added during the filtration stage. Unintercalated polymers show lower decomposition temperatures. The decomposition temperatures (in air) of SPE/MoS_2 and SPE/$MoSe_2$ are summarized in Table 3.9. The different concentrations of polymers from the two systems are due to differences in sample preparations. In addition, the strong lone pair repulsion from 'Se' may hinder the intercalation of some polymers with low cross-section diameters, such as POMOE. High intensity XRD spectra were not achieved from POMOE/$MoSe_2$.

Table 3.9 Decomposition temperatures of SPE/MoS_2 and SPE/$MoSe_2$ intercalates (in air)

SPE/MoS_2	Decomposition temperatures (°C)	SPE/$MoSe_2$	Decomposition temperatures (°C)
$(PEO)_{0.92}/MoS_2$	225	$(PEO)_{1.23}/MoSe_2$	338
$(PVP)_{0.76}/MoS_2$	240	$(PVP)_{0.75}/MoSe_2$	312
$(MCel)_{0.26}/MoS_2$	210	$(MCel)_{0.56}/MoSe_2$.	237
$(POMOE)_{2.3}/MoS_2$	215	$(POMOE)_{0.13}/MoSe_2$	327
$(MEEP)_{0.33}/MoS_2$	185	$(MEEP)_{0.75}/MoSe_2$	229

The red shifts in IR spectra and the T_g shifts in DSC suggest that the ionic conductivity of the polymers have decreased after intercalation, due to the limitation of segmental motion of the SPES by the $MoSe_2$ host. However, both POMOE and MEEP entrapped by the $MoSe_2$ still retain fairly low glass transition temperatures, i.e. both of them are still flexible and are able to undergo segmental motion at low temperature (-35°C), which is key for lithium ion movement. The mechanical stability of the polymers should have been improved, in principle, due to the host-guest interaction. ($MoSe_2$ may work as a 'nanoscale lock' to prevent leaking problems caused by the mechanical instability of the polymer electrolytes.)

The ideal ionic conductivity has not been achieved for MEEP/$MoSe_2$ intercalates. Based on the mechanism of ionic conductivity,[30] an improvement is possible if longer chains of MEEP are achieved, *e.g,* through microwave-assisted polymer synthesis.[93] Part of the long chain extending out of the layers of the $MoSe_2$ will undergo freer segmental motion. In addition, the mole ratio between $(MEEP)_4LiOTf$ and $MoSe_2$ should be increased, because during the purification of the final product, part of the $(MEEP)_4LiOTf$ can be washed away and this has been confirmed by the IR spectra. (The peaks resulting from LiOTf disappeared or weakened in intensity after purification of $(MEEP)_4/MoSe_2$ and $(POMOE)_{25}LiOTf/MoSe_2$ intercalates.)

Chapter 4 Electronically conductive polymers and $MoSe_2$ system

Since solid polymer electrolytes have been intercalated into $MoSe_2$, electronically conductive polymers could also be inserted into the layered structure. The difference is that electronically conductive polymers such as polyaniline can not be dissolved in water. However, suspensions of polyaniline and substituted polyanilines in N-methylformamide (NMF) can be created. Therefore, NMF could be introduced as the solvent in these systems during the intercalation process. The resulting intercalates could be good cathode materials, similar to other systems.[21-24]

4.0 Materials

Polyaniline (PANI), poly(*N*-methyl aniline) (PMA), poly(ethylaniline) (PEA), poly(propylaniline) (PPA) were synthesised by Wade White.[24]

4.1 General methodology for synthesizing electronically conductive polymer/$MoSe_2$ intercalates and for preparing samples for electronic conductivity measurements

In a typical reaction, 30 mL of *N*-methylformamide (NMF) was added to 300 mg of $Li_{0.7}MoSe_2$ and the resulting suspension was sonicated for 4 hours. 1.5 equivalents of the polymer were dissolved in 25 mL NMF with the help of 4 hours of ultrasonication. The polymer suspension and 0.15 mL of 6 M H_2SO_4 were then added to the $MoSe_2$ single layers and the reaction mixture was allowed to stir at room temperature for 40 hours. The resultant black precipitate was purified by

centrifugation. It was then freeze-dried. The freeze-dried sample was pressed into a tablet and was then set in the sample holder (Figure 3.50) for conductivity measurements. The conductivity was measured by Dr. Douglas Dahn in the Department Physics at UPEI using the four-probe van der Pauw technique.

4.2 Results and discussion on electronically conductive polymer and electronically conductive polymer /$MoSe_2$ system

4.2.1 XRD studies for electronically conductive polymer /$MoSe_2$ system

Powder XRD pattern of poly(aniline) is shown in Figure 4.1. The broad peaks indicate that PANI is amorphous. PMA, PEA, and PPA are also amorphous as determined by XRD.[94]

Figure 4.1 XRD spectrum of PANI[94]

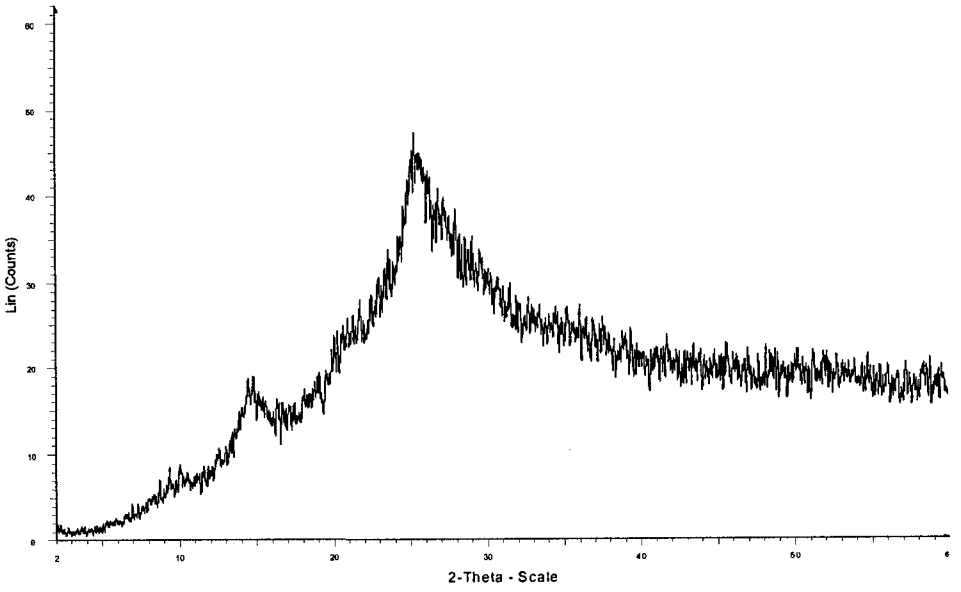

It is interesting to note that PANI, PMA, PEA, and PPA were inserted into MoS_2 by adding a colloidal suspension of the polymers in NMF to the dispersed layers in deionized water. However, attempts to use a NMF/H_2O solvent system did not work for $MoSe_2$ (Figure 4.2). Instead, a single solvent system (NMF) had to be used to prepare the intercalated products (Figure 4.3-4.6).

Figure 4.2 XRD spectrum of PANI/$MoSe_2$ prepared by using a water/NMF solvent mixture

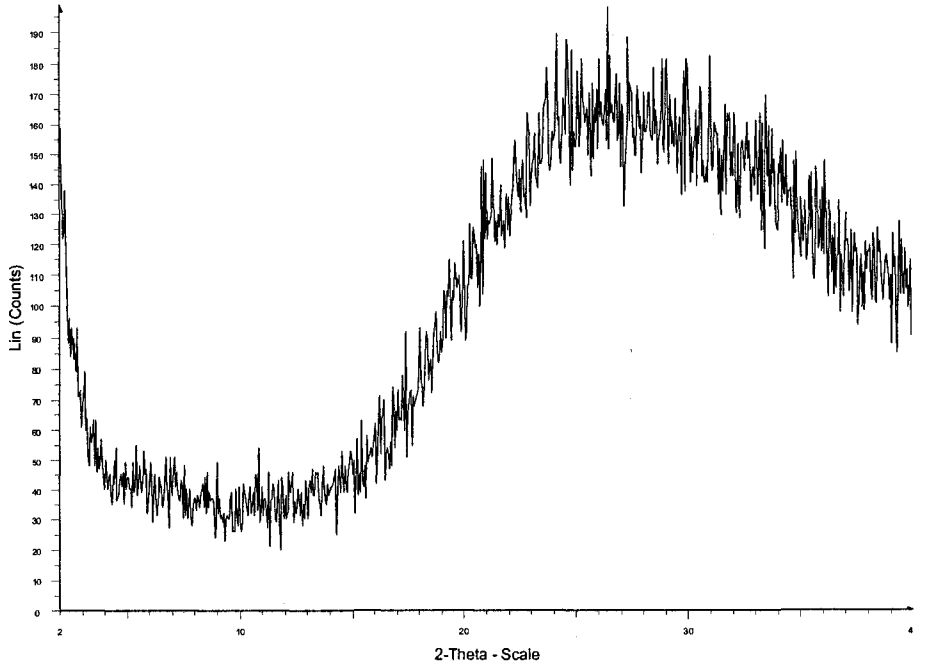

Figure 4.3 XRD spectrum of PANI/$MoSe_2$ intercalate (prepared in NMF solvent)

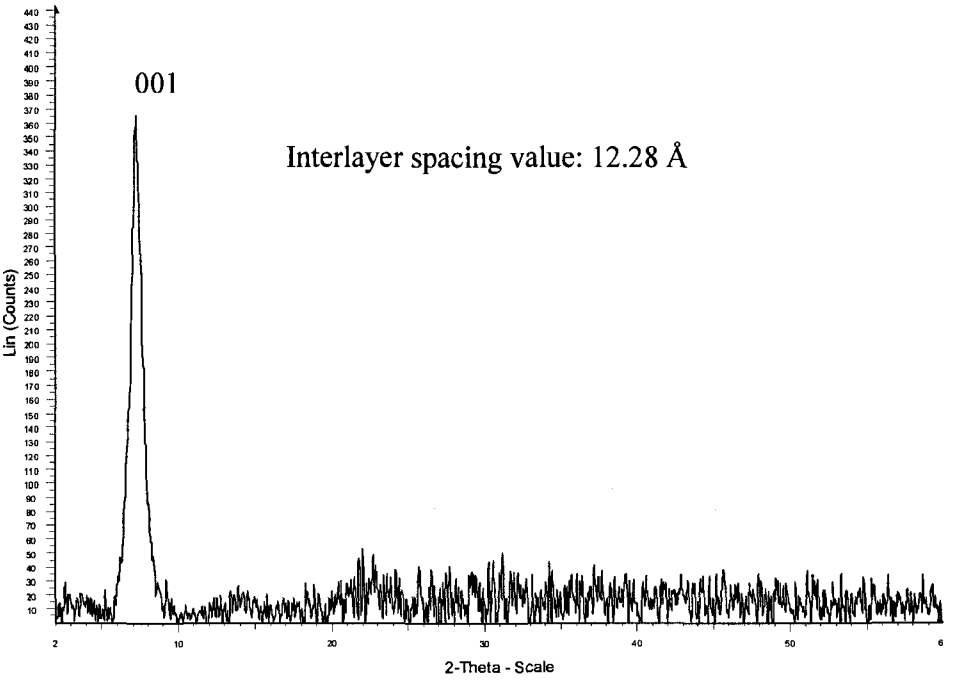

Figure 4.4 XRD spectrum of PMA/$MoSe_2$ intercalate (prepared in NMF solvent)

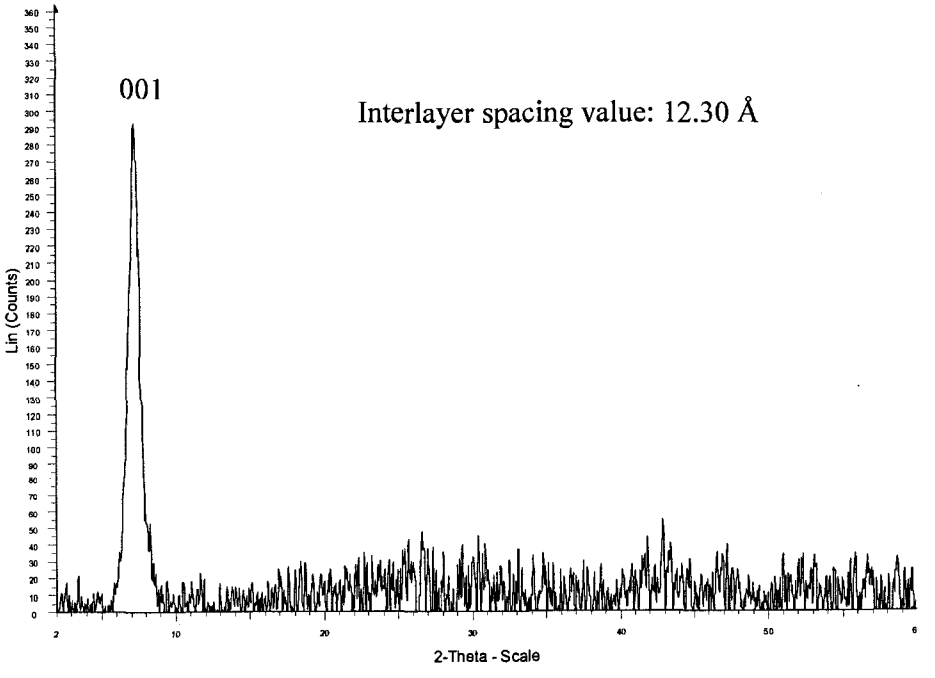

Figure 4.5 XRD spectrum of PEA/$MoSe_2$ intercalate (prepared in NMF solvent)

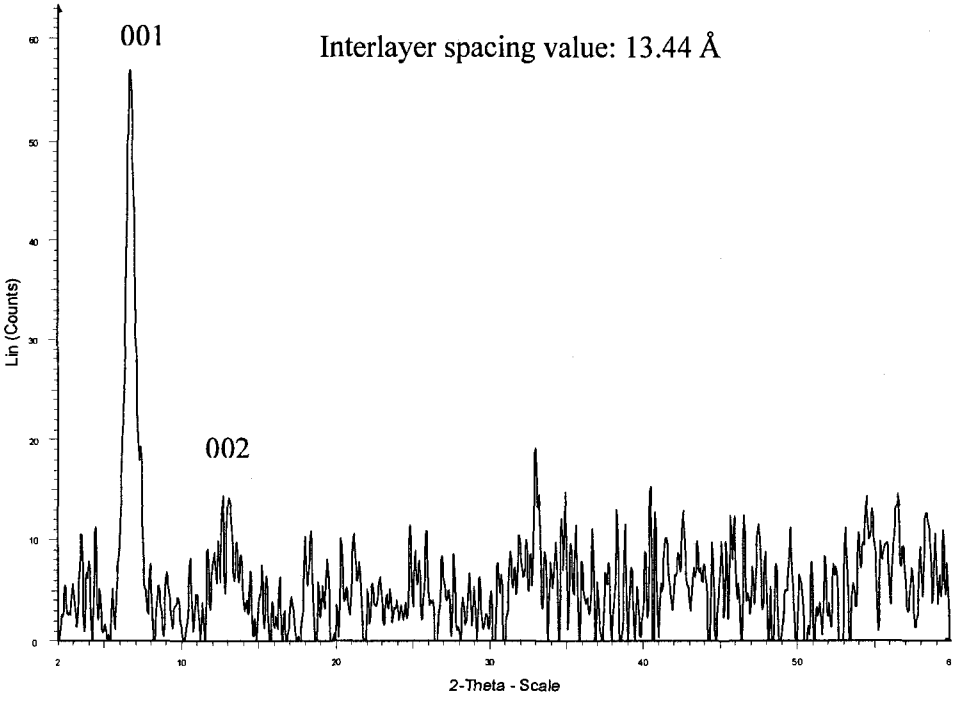

Figure 4.6 XRD spectrum of PPA/$MoSe_2$ intercalate (prepared in NMF solvent)

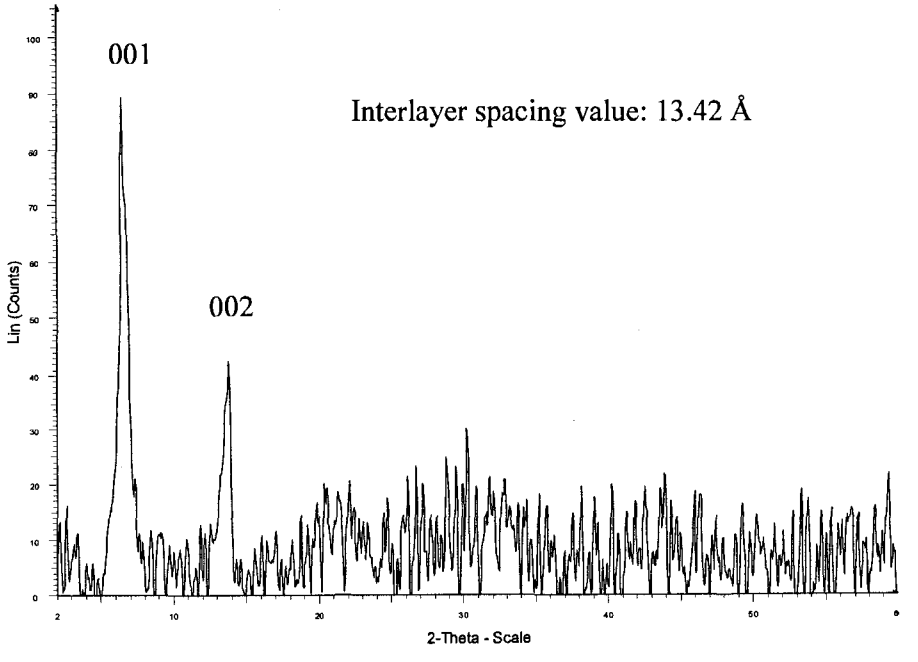

The data on electronically conductive polymer/$MoSe_2$ and electronically conductive polymer/MoS_2 are summarized in Table 4.1. In Table 4.1, the interlayer expansion values from the polymer/$MoSe_2$ system are larger than that from the polymer/MoS_2 system due to the different conformation of polymer between the layers. The computational cross-section diameters of PANI and PPA are 5 Å and 8 Å, respectively.[73] Therefore, based on the interlayer expansion values, the benzene and quinone rings of the polymers (at least part of them) could be perpendicular to the $MoSe_2$ layers while the arrangement of polymers between MoS_2 layers is parallel to the layers. The interlayer spacing values of PEA/$MoSe_2$ and PPA/$MoSe_2$ are about 1.1 Å larger than that of PANI/$MoSe_2$ and PMA/$MoSe_2$ due to the fact that ethyl and propyl substituted groups support the $MoSe_2$ layers. However, for electronically conductive polymer/MoS_2 system, only 0.2 Å of expansion was observed from PANI/MoS_2 to PPA/MoS_2 due to the parallel arrangement of the polymers. This is the other strong evidence for the perpendicular arrangements of the polymers between $MoSe_2$ layers. All of the intercalates in Table 4.1 demonstrate a monolayer insertion of the polymer. The crystallite size of the intercalates are smaller than pristine $MoSe_2$ (370 Å) or pristine MoS_2 (129 Å) due to the imperfect restacking of the host layers.[51]

Table 4.1 Summary of XRD data of electronically conductive polymer/$MoSe_2$ and electronically conductive polymer/MoS_2 intercalates [22, 24, 94]

Intercalate	Solvent system	Interlayer spacing (Å)	Interlayer expansion (Å)	Proposed arrangement	Crystallite size (Å)
PANI/$MoSe_2$	NMF[a]/NMF[b]	12.28	5.86	monolayer	88
PANI/MoS_2	NMF[a]/H_2O[b]	9.68	3.53	monolayer	75
PMA/$MoSe_2$	NMF[a]/NMF[b]	12.30	5.88	monolayer	78
PMA/MoS_2	NMF[a]/H_2O[b]	9.66	3.51	monolayer	80
PEA/$MoSe_2$	NMF[a]/NMF[b]	13.44	7.02	monolayer	88
PEA/MoS_2	NMF[a]/H_2O[b]	9.75	3.60	monolayer	90
PPA/$MoSe_2$	NMF[a]/NMF[b]	13.42	7.00	monolayer	109
PPA/MoS_2	NMF[a]/H_2O[b]	9.89	3.74	monolayer	67

[a]dispersing medium or solvent for guest species; [b]dispersing medium for $Li_{0.7}MoSe_2$ and $LiMoS_2$.

4.2.2 FT-IR studies on electronically conductive polymer /$MoSe_2$ systems

FT-IR spectra of PANI and PANI/$MoSe_2$ are shown in Figure 4.7 and Figure 4.8, respectively, and the main vibrations are summarized in Table 4.2.

Figure 4.7 FT-IR spectrum of PANI

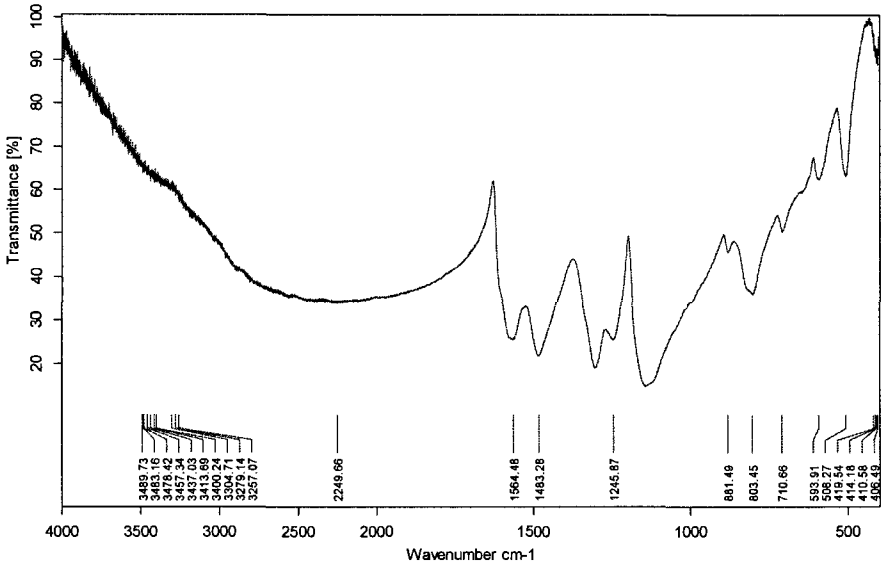

Figure 4.8 FT-IR spectrum of PANI/$MoSe_2$ intercalate

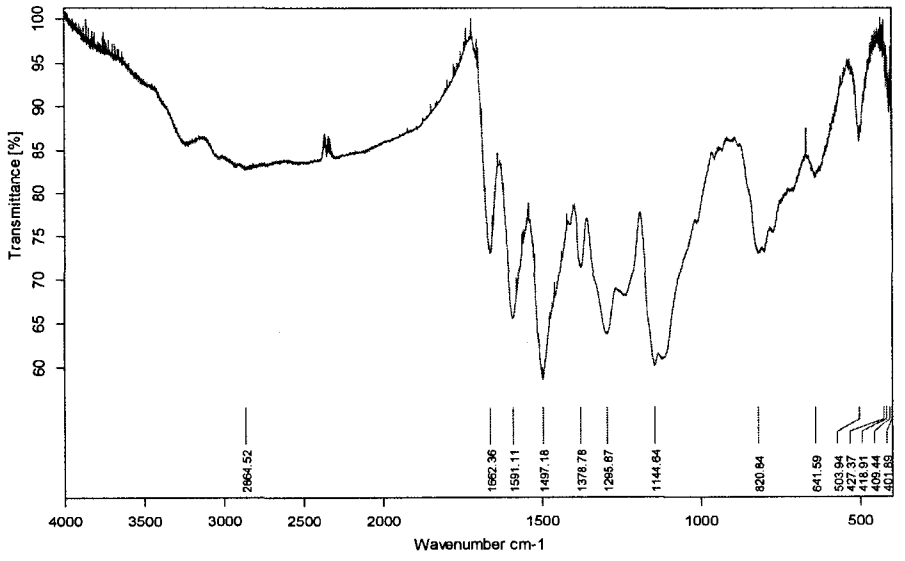

Several vibrarations in PANI/$MoSe_2$ shift to higher wavenumbers. For example, C=C stretching in quinone shifts from 1564 to1591 cm^{-1}, C=C stretching in benzene shifts from 1483 to 1497 cm^{-1} and C-N-C stretching shifts from 1280 cm^{-1} to 1296 cm^{-1}. This is probably due to the reduction of the p-doped polymer caused by the 1T-$MoSe_2$ layered host which is electron rich, and as a result, the force constant of some bonds in the polymer chain increases.

Table 4.2 Summary of Vibrations in FT-IR spectra of PANI and PANI/$MoSe_2$ intercalate[95-98]

Major bond/group	PANI	PANI/$MoSe_2$	Wavenumber shift
C=O stretching (NMF)		1662 cm^{-1}	
C=C stretching in quinone	1564 cm^{-1}	1591 cm^{-1}	+27 cm^{-1}
C=C stretching in benzene	1483 cm^{-1}	1497 cm^{-1}	+14 cm^{-1}
N-H stretching (NMF)		1379 cm^{-1}	
C-N-C stretching	1280 cm^{-1}	1296 cm^{-1}	+16 cm^{-1}
$C-N^+-C$ stretching	1246 cm^{-1}	1246 cm^{-1}	0
C-H bending in plane	1145 cm^{-1}	1145 cm^{-1}	0
C-H deformation	803 cm^{-1}	821 cm^{-1}	+18 cm^{-1}

FT-IR spectra of PMA and PMA/$MoSe_2$ are shown in Figure 4.9 and Figure 4.10, respectively, and the main vibrations are summarized in Table 4.3.

Figure 4.9 FT-IR spectrum of PMA

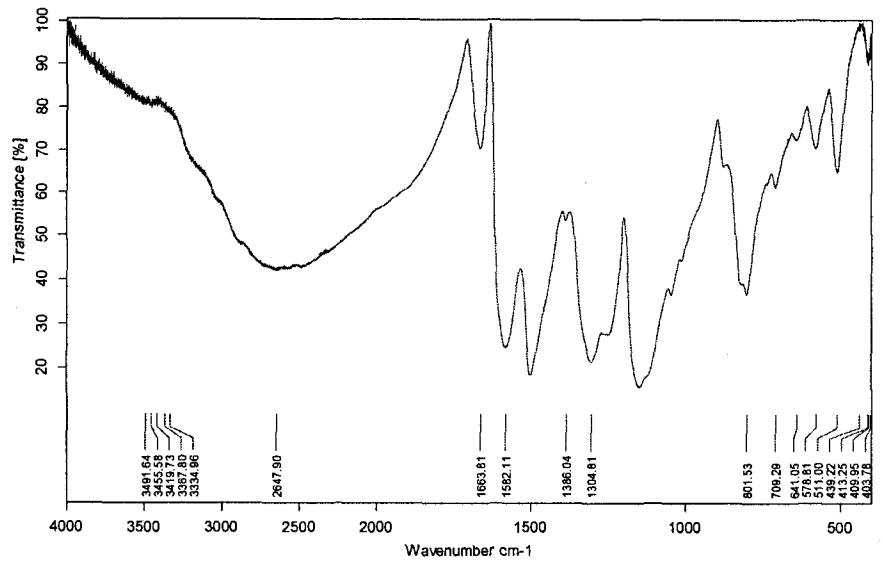

Figure 4.10 FT-IR spectrum of PMA/$MoSe_2$ intercalate

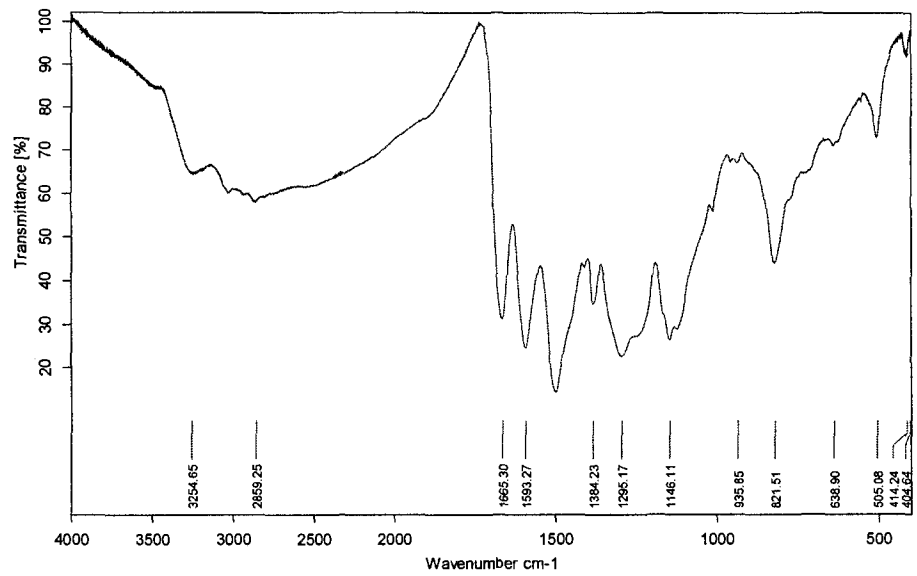

Similar to PANI/$MoSe_2$ system, several vibrations in the PMA/$MoSe_2$ intercalate shift to higher wave numbers compared with the pure polymer (Table 4.3). For example, C=C stretching in quinone shifts from 1582 to 1593 cm^{-1}, and C-H deformation shift from 801 to 822 cm^{-1}. These shifts in wave numbers are due to the reduction of the p-doped polymer by the $MoSe_2$ layers, resulting in an increase in the force constant of the bonds. However, C-N-C stretching decreases from 1305 cm^{-1} down to 1295 cm^{-1} due to the fact that methyl group connected with C-N-C is confined by the layered host.

Table 4.3 Summary of Vibrations in FT-IR spectra of PMA and PMA/$MoSe_2$ intercalate [95-98]

Major bond/group	PMA	PMA/$MoSe_2$	Wavenumber shift
C=O	1664 cm^{-1}	1666 cm^{-1}	+2 cm^{-1}
C=C stretching in quinone	1582 cm^{-1}	1593 cm^{-1}	+11 cm^{-1}
C=C stretching in benzene	1500 cm^{-1}	1498 cm^{-1}	+2 cm^{-1}
N-H stretching (NMF)		1384 cm^{-1}	
C-N-C stretching	1305 cm^{-1}	1295 cm^{-1}	-10 cm^{-1}
C-H bending in plane	1148 cm^{-1}	1146 cm^{-1}	-2 cm^{-1}
C-H deformation	801 cm^{-1}	822 cm^{-1}	+21 cm^{-1}

FT-IR spectrum of PEA and PEA/$MoSe_2$ intercalates are shown in Figure 4.11 and Figure 4.12 respectively, and the main vibrations are summarized in Table 4.4.

Figure 4.11 FT-IR spectrum of PEA

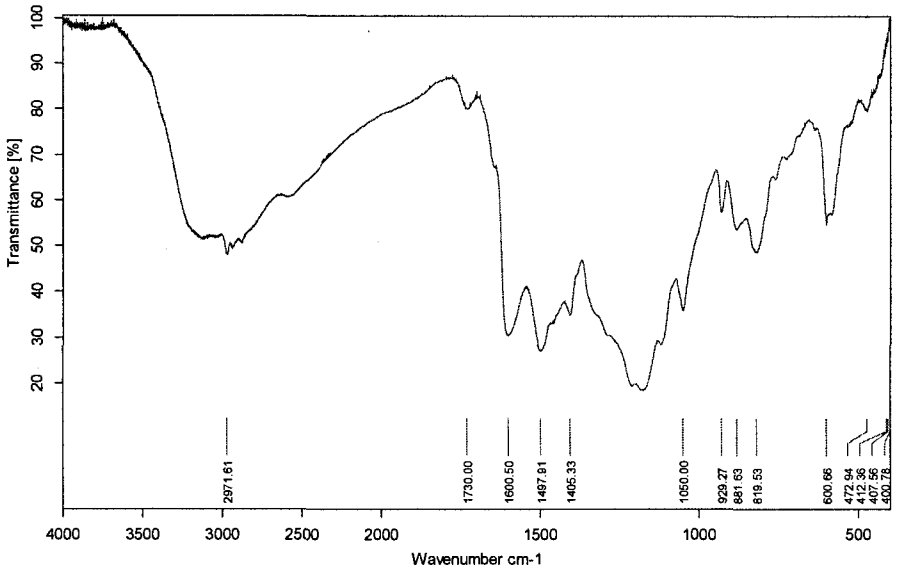

Figure 4.12 FT-IR spectrum of PEA/$MoSe_2$ System

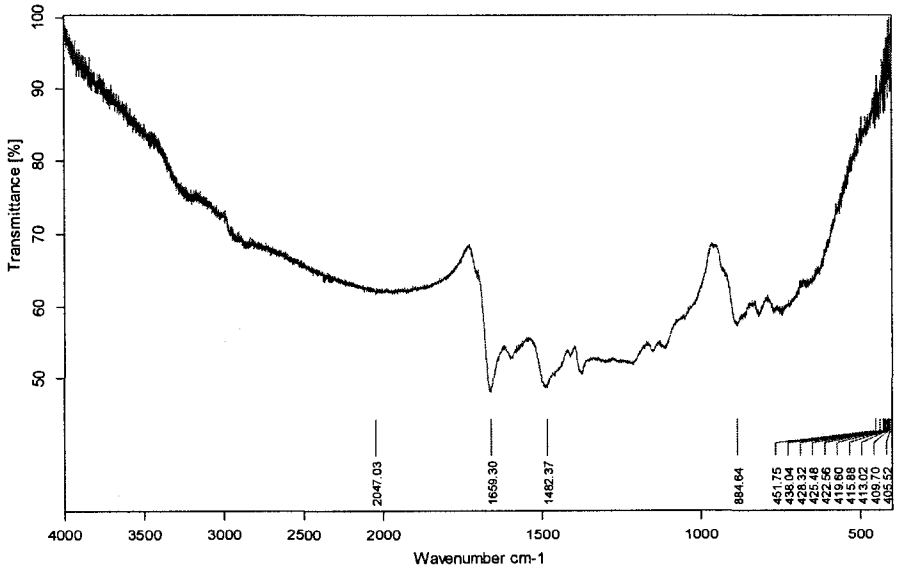

Unlike PANI/$MoSe_2$ and PMA/$MoSe_2$ systems, several wavenumbers of PEA/$MoSe_2$ shift to the lower wavenumbers and some vibrations disappeared (Table 4.4). For example, C=C stretching in quinone shifts from 1600 to 1591 cm^{-1}, and the C=C stretching in benzene shifts from 1498 to 1488 cm^{-1}. The C-N-C stretching disappears and this might be due to the ethyl group preventing the redox reaction between the host and guest and the layered host restricts the vibrations of the polymer bonds.[48]

Table 4.4 Summary of Vibrations in FT-IR spectra of PEA and PEA/$MoSe_2$ intercalate[95-98]

Major bond/group	PEA	PEA/$MoSe_2$	Wavenumber shift
C-H bend asymmetric	2972 cm^{-1}		
C=O stretching (NMF)		1659 cm^{-1}	
C=C stretching in quinone	1600 cm^{-1}	1591 cm^{-1}	-9 cm^{-1}
C=C stretching in benzene	1498 cm^{-1}	1488 cm^{-1}	-10 cm^{-1}
N-H stretch (NMF)		1376 cm^{-1}	
C-N-C stretching	1210 cm^{-1}		
C-H bending in plane	1050 cm^{-1}		
C-H deformation	819 cm^{-1}		

FT-IR spectrum of PPA and PPA/$MoSe_2$ are shown in Figure 4.13 and Figure 4.14 respectively, and the main vibrations are summarized in Table 4.5.

Figure 4.13 FT-IR spectrum of PPA

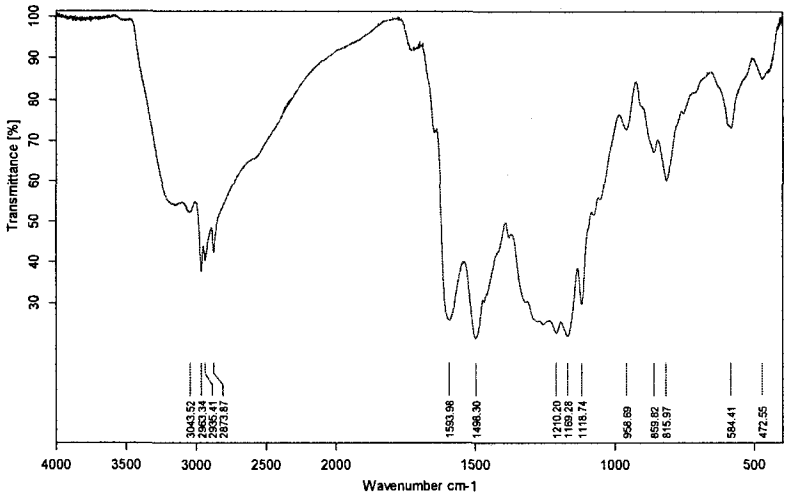

Figure 4.14 FT-IR spectrum of PPA/$MoSe_2$

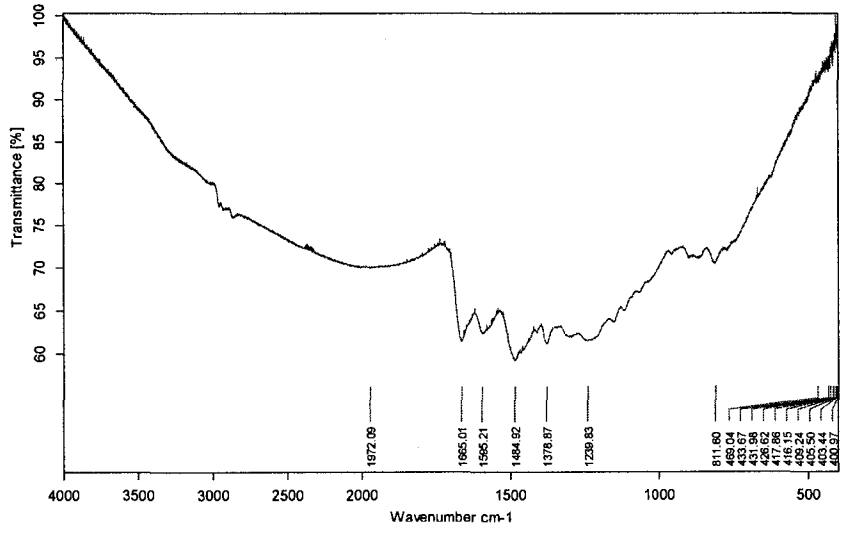

Similar to the PEA/$MoSe_2$ system, several wavenumbers of PPA/$MoSe_2$ shift to lower wavenumbers (Table 4.5). For example, C=C stretching in benzene shifts from 1498 to 1485 cm^{-1} and C-N-C stretching completely disappeared. This might be due to

the fact that the propyl group prevented a redox reaction between the host and guest and the layered host restricted the vibrations of the polymer.[48]

Table 4.5 Summary of Vibrations in FT-IR spectra of PPA and PPA/$MoSe_2$ intercalate[95-98]

Major bond/group	PPA	PPA/$MoSe_2$	Wavenumber shift
C-H bend asymmetric	2963 cm^{-1}		
C-H bend asymmetric	2874 cm^{-1}		
C=O stretching (NMF)		1665 cm^{-1}	
C=C stretching in quinone	1594 cm^{-1}	1595 cm^{-1}	+1 cm^{-1}
C=C stretching in benzene	1498 cm^{-1}	1485 cm^{-1}	-13 cm^{-1}
N-H stretch (NMF)		1379 cm^{-1}	
C-N-C stretching	1210 cm^{-1}		
C-H bending in plane	1118 cm^{-1}		
C-H deformation	815 cm^{-1}	811 cm^{-1}	-4 cm^{-1}

These data from IR are consistent with the proposed conformations of the polymers from XRD data. The perpendicular arrangement of polymers between the $MoSe_2$ layers creates opportunities for $MoSe_2$ layers to confine the vibrations of PEA and PPA more dramatically. The result is that several IR bands disappeared in the spectra of PEA/$MoSe_2$ and PPA/$MoSe_2$ intercalates.

4.2.3 Electronic conductivity of Polymer/$MoSe_2$ intercalates

The graph in Figure 4.15 shows resistivity data on electronically conductive polymer/$MoSe_2$ intercalates, as well as 2H-$MoSe_2$ and 'restacked $MoSe_2$' (1T form). These data can be converted to conductivity by taking the reciprocal. At 293K, the 2H-$MoSe_2$ is a semiconductor with a conductivity of 1 $x10^{-3}$ S/cm. The conductivity of metallic 1T-$MoSe_2$ is much higher than that of semi-conductive 2H-$MoSe_2$. At 300K, the conductivity of 1T-$MoSe_2$ is 5 $x10^{-2}$ S/cm which is close to that of 1T-MoS_2 (9 $x10^{-2}$ S/cm).[24] At 300K, the conductivity of PMA/$MoSe_2$ is 4 $x10^{-3}$ S/cm, and the conductivity of PMA is about 1 $x10^{-3}$ S/cm.[94] The conductivity of PMA/$MoSe_2$ nanocomposite is between that of PMA and 1T $MoSe_2$, and the temperature dependence is similar to that of 1T $MoSe_2$. However, the PANI/$MoSe_2$ intercalate had a fairly low conductivity value ($1x10^{-4}$ S/cm at 300K). This low value might be due to the sample preparation. For example, during the reaction, 1T-$MoSe_2$, which is metallic, might be able to reduce part of the p-doped polymers and the conductivity of the polymer was reduced. In addition, 1T-$MoSe_2$ can be converted back to the 2H form during the tablet preparation. For comparison, p-doped PANI has a conductivity of 10 S/cm at room temperature.[94] A later sample of PANI/$MoSe_2$ shows even lower conductivity (3 $x10^{-7}$ S/cm at room temperature). The low conductivity of the PANI/$MoSe_2$ and the relatively high conductivity of the PMA/$MoSe_2$ are consistent with their wave number shift in their IR spectra. The shift of C=C stretching between PANI/$MoSe_2$ and doped PANI is more than that between PMA/$MoSe_2$ and doped PMA. This suggests that the methyl group in PMA somewhat

prevented reduction of the p-doped polymer by the $MoSe_2$ layers. However, PPA/$MoSe_2$ and PEA/$MoSe_2$ intercalates had such low conductivities due to the conformations of the polymers and the side groups. The propyl and ethyl groups are not as conductive as the conjugated part, and they can separate the conjugated part from the layered host. Similar to PMA/$MoSe_2$ system, the wave number shifts in the IR spectra of PPA/$MoSe_2$ and PEA/$MoSe_2$ also suggest that the propyl and ethyl groups prevented reduction of the p-doped polymer by the $MoSe_2$ layers.

Figure 4.15 Electronic conductivity of 2H-$MoSe_2$, 1T-$MoSe_2$ and Polymer/$MoSe_2$ intercalates measured at various temperatures

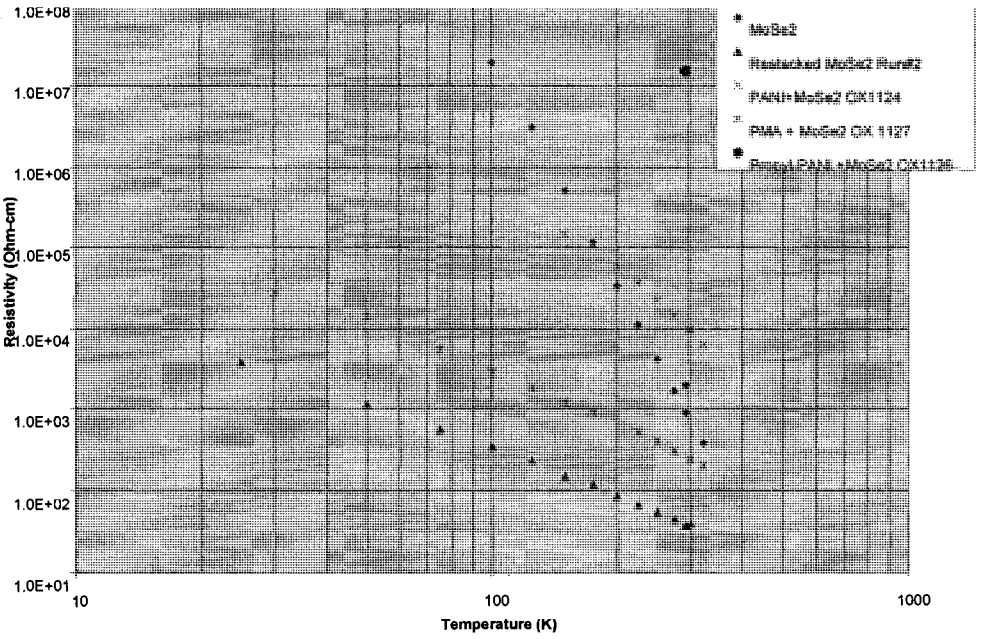

The room temperature electronic conductivity of doped polymers, polymer/$MoSe_2$ intercalates and polymer/MoS_2 intercalates are summarized in Table 3.6. In Table 3.6, only PMA/$MoSe_2$ has a higher conductivity compared with

PMA/MoS_2. The conductivity of PANI/MoS_2 is much higher than that of PANI/$MoSe_2$.This might be due to the fact that 1T-MoS_2 is a weaker reducing agent than 1T-$MoSe_2$, and that p-doped PANI is well preserved by the MoS_2 layers. When the methyl group protected the doped backbones of the polymer, the conductivity of PMA/$MoSe_2$ was observed to be close to that of PMA/MoS_2. For PEA/MoS_2 and PPA/MoS_2 intercalates, the side chains of the polymers with parallel arrangements extend along with the MoS_2 layers, so that they do not hinder the electron transfer when electrodes are applied to the sample. Therefore, PEA/MoS_2 and PPA/MoS_2 still show higher conductivities than doped PEA and PPA, respectively.

Table 4.6 Electronic conductivities of polymers, polymer/MoS_2 and polymer/$MoSe_2$ intercalates at room temperature [24]

Materials	Electronic Conductivities (S/cm)
PANI	1×10^{1}
PANI/MoS_2	3×10^{-1}
PANI/$MoSe_2$	1×10^{-4}
PMA	1×10^{-3}
PMA/MoS_2	2×10^{-3}
PMA/$MoSe_2$	4×10^{-3}
PEA	3×10^{-4}
PEA/MoS_2	1×10^{-3}
PEA/$MoSe_2$	0
PPA	1×10^{-4}
PPA/MoS_2	1×10^{-2}
PPA/$MoSe_2$	$<10^{-7}$

In this chapter, electronically conductive polymers have been successfully inserted into the $MoSe_2$ layered structure as evidenced by XRD. Based on the mechanism of the cathode materials the resulting sandwiched compound may be used as cathode materials due to the multiple advantages such as increased interspacing value that could result in an increase in cell capacity and an enhancement of the diffusion of lithium ions.[21]

Chapter 5 $MoSe_2$ and Small Molecules

In the previous chapters, it has been shown that by using the exfoliating and restacking properties of $Li_{0.7}MoSe_2$, a wide range of polymers can be inserted into $MoSe_2$. This technique is not limited to macromolecules. The intercalation capabilities of $MoSe_2$ were further explored by using small molecules as guest species. The chosen guests are glycine, ferrocene, and a macrocycle ligand. The resulting hybrid materials may possess improved ionic conductivity, electronic conductivity or catalytic activity.[54, 58, 99-100]

5.0 Materials:

Glycine (99%) was purchased from BDH Chemicals and used as received.

Ferrocene (98%) was purchased from Aldrich and used as received.

7,7,14,14-Tetramethyl-1,4,8,11-tetrazacyclotetradeca-4,11-diene (TTCD) (Figure 5.1) was synthesized by Dr. Haines' group at UPEI.

Figure 5.0 Structure of 7,7,14,14-Tetramethyl-1,4,8,11tetraaza-cyclotetradeca-4,11-diene (TTCD)

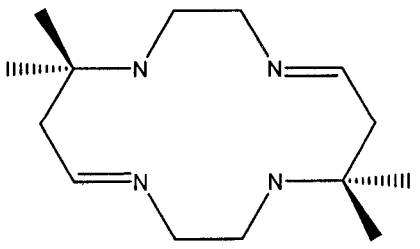

5.1 General methodology for synthesizing small molecule/$MoSe_2$ intercalates

$Li_{0.7}MoSe_2$ (100 mg) was charged into a 50 mL Erlenmeyer flask in the dry box. The sample was removed from the dry box, and deionized water (10 mL) was added to the $Li_{0.7}MoSe_2$. The mixture was sonicated for two hours. At the same time, glycine or the macrocycle is dissolved in deionized water, and ferrocene is dissolved in ether. The solutions of small molecules were then added to the $Li_{0.7}MoSe_2$ suspension, dropwise, with stirring. The resulting mixture was allowed to stir for 24 hours. The intercalates were purified by filtration or centrifugation. Part of the wet sample was cast on a glass substrate and dried in the fume hood for XRD analysis. The concentration of the small molecule solutions and the mole ratio between guests and host are illustrated in Table 5.1. The relatively high mole ratio of ferrocene to $MoSe_2$ was used to guarantee full intercalation reaction at the interface of the solvents.

Table 5.1 Summary of the solvent systems, concentration of the solutions and mole ratio between guest and host

Guest species	Solvent system	Concentration of guest solution	Mole ratio of guest/host
glycine	H_2O^a/H_2O^b	7.8mg/mL	2.7
ferrocene	H_2O^a/Ether^b	10.3mg/mL	10
TTCD	H_2O^a/H_2O^b	3.4mg/mL	0.2

[a]dispersing medium for $Li_{0.7}MoSe_2$; [b]dispersing medium or solvent for guest species

5.2 Results and Discussions

Powder X-ray diffraction (Figures 5.1-5.3) clearly shows that the intercalation compounds (glycine/$MoSe_2$, ferrocene/$MoSe_2$ and TTCD/$MoSe_2$) have been formed. The XRD data were summarized in Table 5.2. The interlayer expansion value of glycine/$MoSe_2$ is 5.63 Å, corresponding to a proposed bilayer insertion of the guest.[99] The computational cross section diameters of ferrocene and TTCD are about 5 Å and 6 Å, respectively.[73] The interlayer expansion of ferrocene/$MoSe_2$ and TTCD/$MoSe_2$ are about 6 Å, corresponding to a monolayer insertion. The crystallite sizes of ferrocene/$MoSe_2$ and macrocycle/$MoSe_2$ intercalates are much larger than that of the glycine/$MoSe_2$ intercalate due to the more orderly restacking in ferrocene/$MoSe_2$ and TTCD/$MoSe_2$ systems.[51] (The average crystallite size of virgin $MoSe_2$ was found to be 370 Å). The attractions between the positive charged transition metal centers and the electron-rich groups of ferrocene and TTCD may help the system restack more properly.

Figure 5.1 XRD spectrum of glycine/$MoSe_2$ (mole ratio 2.7:1)

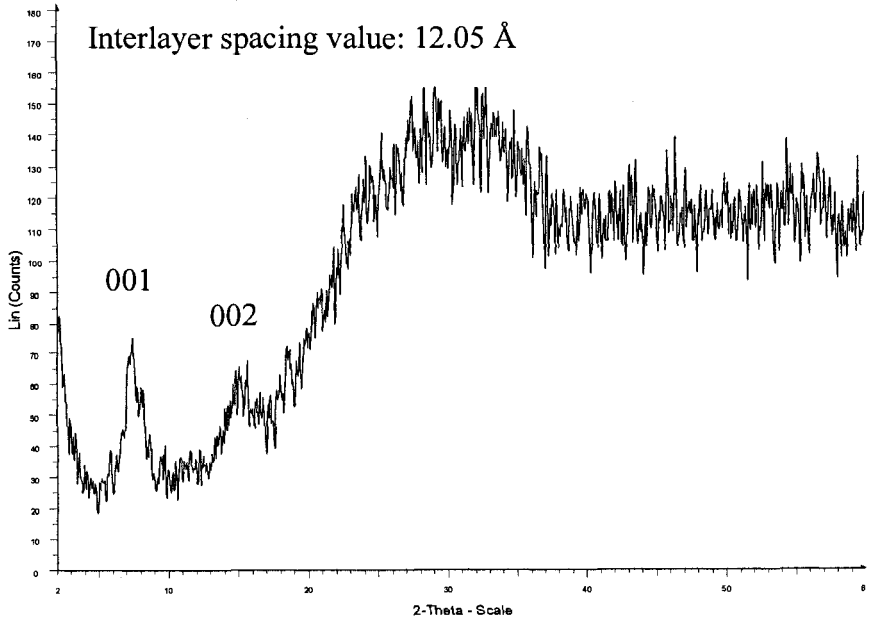

Figure 5.2 XRD spectrum of ferrocene/$MoSe_2$ (mole ratio 10:1)

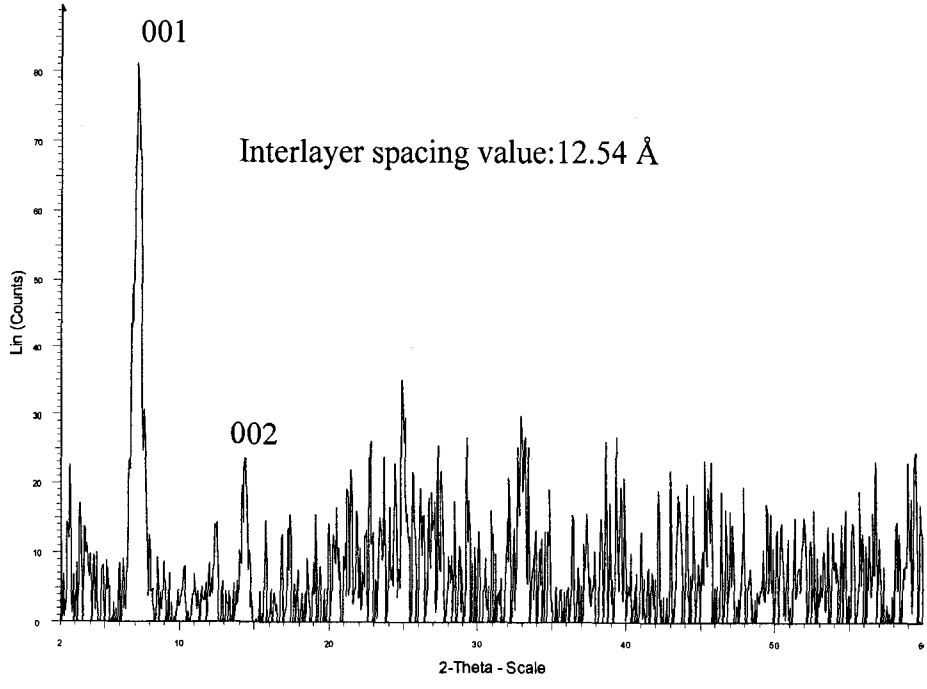

Figure 5.3 XRD spectrum of TTCD/$MoSe_2$ intercalate (mole ratio 0.2:1)

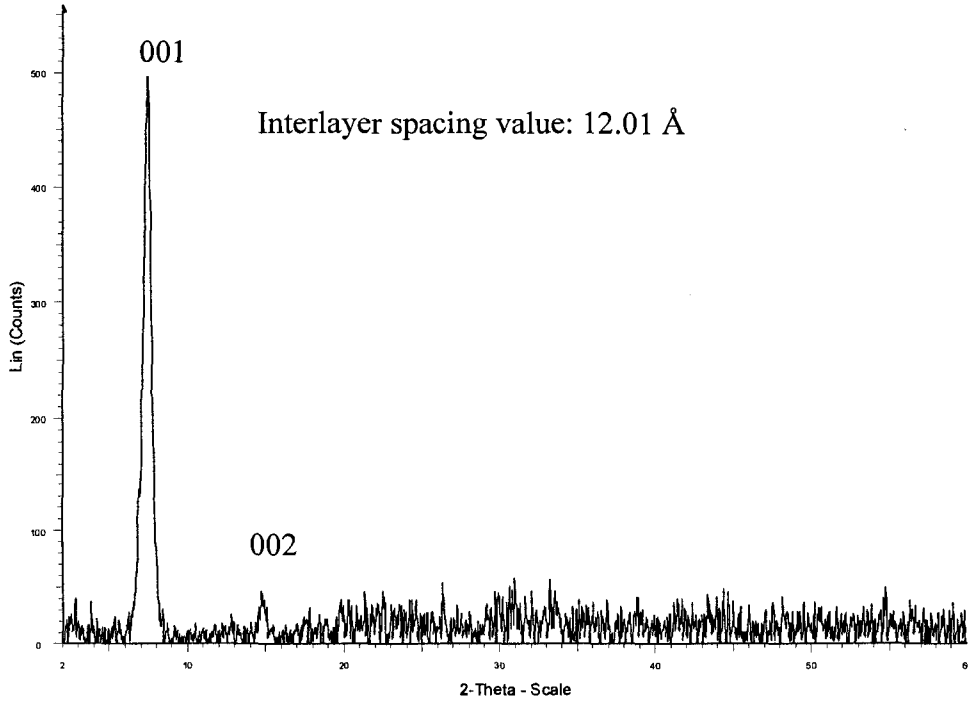

Table 5.2 Summary of the XRD data from small molecule/$MoSe_2$ intercalates

Guest species	Interlayer spacing (Å)	Interlayer expansion(Å)	Proposed arrangement	Crystallite size (Å)
Glycine	12.05	5.63	bilayer	69
Ferrocene	12.54	6.12	monolayer	246
TTCD	12.01	5.59	monolayer	236

Similar work has been done for MoS_2 and other systems. In glycine/$VOPO_4$ the interlayer expansion value was found to be 2.46 Å, which corresponds to a single layer insertion of the guest with the alkyl chain axis perpendicular to the layers.[99] Therefore, based on the larger interlayer spacing value (5.63 Å) measured from glycine/$MoSe_2$ intercalate, it appears that a bilayer of glycine was inserted into the $MoSe_2$ layers. An interlayer expansion value observed from the Cp_2Co^+/MoS_2 system is about 5.15 Å[54] which is close to ferrocene/$MoSe_2$. Similar structural macrocycles have been intercalated into the MoS_2 system.[58] The interlayer expansion values are smaller than TTCB/$MoSe_2$ system due to the different arrangement of the guest species between layers. In the MoS_2 system, arrangement of the macrocycles between MoS_2 layers is lamellar due to the fact that interlayer expansion values observed are close to the values of their thickness and are smaller than their computational cross section diameters.[73] The crystallite size of TTCB/$MoSe_2$ intercalate is larger than that observed in macrocycle/MoS_2 system due to the smaller crystallite size of pristine MoS_2.[58]

The conductivity or catalytic activity of the sandwiched compounds synthesized in this chapter will be confirmed by further characterization.

Chapter 6 Conclusions and Future work

The 2H-$MoSe_2$ layered structure has been successfully exfoliated. The resulting material undergoes a phase transition from the 2H-form to the 1T-form, which showed a dramatic increase in electronic conductivity. When heat was introduced, the 1T-form turned back to the 2H-form, and the activation energy (84 kJ/mol) for this conversion was determined by DSC. Compared with the activation energy of WS_2 and MoS_2, the higher activation energy of $MoSe_2$ suggests that 1T metallic form of $MoSe_2$ is more stable.[68] The mole ratio between Li and $MoSe_2$ in the lithiated phase (Li_xMoSe_2) was measured by titration method and the stoichiometry was calculated to be $Li_{0.7}MoSe_2$. The amorphous 'restacked $MoSe_2$' could be a material with improved promise for HDS catalysis and a cathode material with enhanced performance. Compared with the crystalline restacked MoS_2, the increased surface area of amorphous 'restacked $MoSe_2$' will enhance its activity as an HDS catalyst and the diffusion of lithium ions in this cathode material could also be improved dramatically. It could also be an improved smoke material for military purpose.[55] The stronger lone pair repulsions along the C axis of the anisotropic $MoSe_2$ are strong enough to prevent the dispersed $MoSe_2$ particles to restack and keep the function of smoke for military purpose. All these points suggest that $MoSe_2$ may be a superior material to MoS_2 for these applications.

Guest species such as solid polymer electrolytes, electronically conductive polymers, and small molecules have been successfully inserted into the $MoSe_2$ layered

host by the exfoliation and restacking properties of $Li_{0.7}MoSe_2$, and the resulting products showed smaller crystallite size compared with pristine $MoSe_2$, as measured by XRD.

The stoichiometry of the solid polymer electrolytes/$MoSe_2$ nanocomposites were determined by TGA. The results indicate that a large amount of polymer has been intercalated into the $MoSe_2$ layered structure.

FT-IR studies showed that the $MoSe_2$ layered host limits the vibrations from the bonds of the inserted polymer guests, and may reduce the positively doped electronically conductive polymers. These results can also help to understand the conformations of polymer between the layers of the host.

DSC studies revealed that the T_g of POMOE and MEEP shift to higher temperature when they were entrapped by $MoSe_2$. These polymers entrapped by the $MoSe_2$ still retain fairly low glass transition temperatures, *i.e.* both of them are still flexible and are able to undergo segmental motion necessary for ionic conduction at low temperatures. In addition, the mechanical stability of the polymers should have been improved, in principle, due to the host-guest interaction. This will be analyzed *via* dynamic mechanical analysis in the future.

Ionic conductivity increased when MEEP was complexed with LiOTf in the ratio: $(MEEP)_4LiOTf$. However, the conductivity value of the $(MEEP)_4LiOTf/MoSe_2$ nanocomposite was too low to be qualified as an electrolyte. In the future, the microwave assisted polymer synthesis will be carried out to achieve higher molecular weight MEEP and higher yields. The increased mole ratio between $(MEEP)_4LiOTf$

and $MoSe_2$ will be explored and the ionic conductivities of the resulting materials will be measured. The ionic conductivity of $(POMOE)_{25}LiOTf/MoSe_2$ intercalate with a higher mole ratio of $(POMOE)_{25}LiOTf$ to $MoSe_2$ should also be explored.

The electronic conductivity of $PMA/MoSe_2$ intercalate showed good results. However, $PANI/MoSe_2$, $PEA/MoSe_2$ and $PPA/MoSe_2$ showed very low conductivity values. Improvements in the sample preparation, such as planting the nanocomposites directly on a stainless plate in the direction parallel to the layers may enhance the conductivity dramatically due to the anisotropic properties of $MoSe_2$.[32, 55-57] In the future, an n-doped polymer/$MoSe_2$ composite should be synthesized and the conductivity should be measured as well. Therefore, the loss of conductivity caused by the redox reaction between p-doped polymer and the $MoSe_2$ can be prevented.

Small molecules such as glycine, ferrocene, and TTCD have been inserted into the $MoSe_2$ layered host. The host guest interaction, the electronic conductivity and catalytic activity of small molecules/$MoSe_2$ intercalates should be studied in the future.

List of references

1. Powell, A. V. *Phys. Chem.* **1993,** *90,* 177.

2. Atwood, E. J. L.; Davies, J. E. D.; Macnicol, D. D. *Academic Press London,* **1984,** *1,* 249.

3. Chippindale, A. M.; Dickens, P.G.; Powell, A.V. *Progr. Solid State Chem.* **1991,** *21,* 133.

4. Dickens, P. G.; Chippindale, A. M.; *'Proton Conductors'*, Ed. Colomban, P. *Cambridge University Press*, **1992,** 101.

5. Schollhorn, R. *Angew. Chem.***1980,** *19,* 983.

6. James, A.C.W.P.; Goodenough, J.B.; Clayden, N.J. *J. Solid State Chem.* **1988,** *77,* 356.

7. Delmas, C.; Saadoune, I. *Solid State Ionics,* **1992,** *370,* 53.

8. Dickens, P.G. Pye, M. F. *'Intercalation Chemistry',* Ed. Whittingham, M.S.; Jacobson, A. J. *Academic Press, New York,* **1982,** *16,* 539.

9. Whittingham, M. S. *Progr. Solid State Chem.***1978,** *12,* 41.,

10. Rouxel, J. *'Intercalated Layered Materials',* Ed. Levy, F.; Reidel, D. *Dordrecht,* **1979,** 201.

11. Corbett, J.D.; *'Intercalation Chemistry',* Ed. Whittingham, M.S.; Jacobson, A.J.; *Academic Press New York.* **1982,** 361.

12. Jacoboson, A. J.; Johnson, J. W.; Brody, J. F.; Scanlon, J.C.; Lewandowski, J.T. *Inorg. Chem.* **1985,** *24,* 1782.

13. Brec, R. *Solid State Ionics,* **1986,** *22,* 3.

14. Fragnaud, P.; Brec, R.; Prouzet, E.; Deniard, P. *Muter. Res. Bull,* **1993,** *28,* 337.

15. Schollhorn, R.; Steffen, R.; Wagner, K. *Angew. Chem.* **1983,** *22,* 555.

16. O'Hare, D.; Bruce, D. W. *'Inorganic Materials',* Ed. Bruce, D. W.; O'Hare, D. *Wiley, Chichester,* **1992,** *4,* 165.

17. Jacobson, A. J. *'Solid State Chemistry: Compounds',* Ed. Cheetham, A. K.; Day, P. *Clarendon Press, Oxford,* **1992,** *6,* 182.

18. Yang, D.; Westreich, P.; Frindt, R.F. *Nanostructured Materials*, **1999**, *12*, 456.

19. Marshall, B. *Howstuffworks,* **2006.**

20. Whittingham, M. S. *Chem. Rev.* **2004,** *104*, 4271.

21. Kerr, T. A.; Wu, H.; Nazar, L. F. *Chem. Mater.* **1996,** *8,* 2005

22. Kanatzidis, M.G.; Bissessur, R.; DeGroot, D. C.; Schindler, J. L.; Kannewurf, C. R. *Chem. Mater.* **1993,** *5*, 595.

23. Liu, Y.-J.; Kanatzidis, M. G. *Inorg. Chem.* **1993,** *32,* 2989.

24. Bissessur, R.; White, W. *Materials Chemistry and Physics* **2006,** *99,* 214.

25. MacDiarmid, A. G. *Angew. Chem. Int. Ed.* **2001,** *40, 2581.*

26. Suga, T.; Pu, Y.-J.; Kasatori, S.; Nishide, H. *Macromolecules* **2007,** *40,* 3167.

27. Novak, P.; Muller, K.; Santhanam, K. S. V.; Haas, O. *Chem. Rev.* **1997,** *97*, 20

28. *"Information for the public", Nobelprize.org.* **2000.**

29. Schon, J. H.; Dodabalapur, A.; Bao, Z.; Kloc, C.; Schenker, O.; Batlogg, B.; *Nature,* **2001,** *410,* 189.

30. Allcock, H. R.; Lampe, F. W.; Mark, J. E. *Contemporary Polymer Chemistry.* **2003,** *3rd, Ed.*

31. Bredas, J. L.; Street, G. B. *Acc. Chem. Res.* **1985,** *18,* 309.

32. Chan. C. K.; *Peng.* H.; Liu. G.; Mcilwrath. K.; Zhang. X. F.; Huggins. R. A.; Cui. Y. *Nature Nanotechnology* **2008,** *3,* 31.

33. Boukamp, B. A.; Lesh, G. C.; Huggins, R. A. *J. Electrochem. Soc.* **1981,** *128,* 725.

34. Shodai, T.; Okada, S.; Tobishima, S.; Yamaki. J. *Solid State Ionics* **1996,** *86,* 785.

35. Poizot, P.; Laruelle, S.; Grugeon, S.; Dupont, L.; Tarascon, J. M. *Nature.* **2000,** *407, 496.*

36. Scully, F. S. *UPEI, Chemistry Department, Master's Thesis* **2007.**

37. Meyer, H. W. *Adv. Mater.* **1998,** *10,* 6, 439.

38. Bissessur, R.; Scully, F. S. *Solid State Ionics,* **2007,** *178,* 877.

39. Nicholas, C. V.; Wilson, D. J., Booth, C. *British Polymer Journal* **1998,** *20,* 289.

40. Xu, W.; Belieres, J.-P.; Angell, C. A. *Chem. Mater.* **2001,** *13,* 575.

41. Allcock, H. R.; Austin, P. E.; Neenan, T. X.; Sisko, J. T.; Blonsky, P. M.; Shriver, D. F. *Macromolecules* **1986,** *19,* 1508.

42. Scully, F. S. *UPEI, Chemistry Department, Honour's Thesis* **2005**

43. Croce, F.; Appetecchi, G. B.; Persi, L.; Scrosati, B. *Nature* **1998,** *394,* 456.

44. Yang, Q.-Z.; Zhang, C.-G.; Sun, D.-J. *Chemistry* **2002,** *65,* w57.

45. Enomoto, H.; Lerner, M. M. *Journal of Physics and Chemistry of Solids* **2004,** *65,* 587

46. Lemmon, J. P.; Lerner, M. M. *Solid State Communications* **1995,** *94,* 533.

47. Tsai, H.-L.; Schindler, J. L.; Kannewurf, C. R.; Kanatzidis, M. G. *Chem. Mater.* **1997,** *9,* 875.

48. Xu, B.-H,; Lin, B-Z.; Sun, D-Y.; Ding, C. *Electrochimica Acta,* **2007,** *52* 3028.

49. Bissessur, R.; Gallant, D.; Brüning, R. *Materials Chemistry and Physics,* **2003,** *82,* 316.

50. Bissessur, R.; Gallant, D.; Brüning, R. *Journal of Materials Science Letters,* **2003,** *22,* 429.

51. Bissessur, R.; Gallant, D.; Brüning, R. *Solid State Ionics,* **2003,** *158,* 205

52. Bissessur, R.; Schipper, D. *Materials Letters,* **2008,** *62,*1638.

53. Kochubey, D. I.; Rogov, V. A.; Babenko, V. P. *React. Kinet. Catal. Lett.* **2007,** *90,* 167.

54. Dungey, K. E.; Curtis, M. D.; Penner-Hahn, J. E. *Journal of Catalysis,* **1998,** *175,* 129.

55. Spence, D'A. E. *University of Maryland, Chemistry Department, Master's Thesis,* **2003.**

56. Kertesz, M.; Hoffmann, R.; *J. Am. Chem. Soc.* **1984,** *106,* 3453.

57. Morales, J.; Santos, J.; Tirado, J. L. *Solid State Ionics,* **1996,** *83,* 57.

58. Bissessur, R.; Haines, R. I.; Brüning, R. *J. Mater. Chem.* **2003,** *13,* 44

59. Wypych, F.; Weber, T.; Prins, R. *Chem. Mater.* **1998,** *10,* 723.

60. Gordon, R. A.; Yang, D.; Crozier, E. D.; Jiang, D. T.; Frindt, R. F. *Physical Review B,* **2002,** *65,* 125407.

61. Westreich, P. *McGill University, Department of Physics, Master's Thesis*, **1996.**

62. Schneemeyer, L. F.; Sienko, M. J. *Inorg. Chem,* **1980,** *19,*789.

63. Böker, T.; Severin, R.; Müller, A. Janowitz, C.; Manzke, R. *Physical Review B,* **2001,** *64,* 235305

64. Sienicki, W. *Mater. Chem. and Phys.* **2001,** *68,* 119.

65. Lemmon, J. P.; Wu, J.; Oriakhi, C.; Lerner, M. M. *Electrochim. Acta*, **1995**, *40*, 2245.

66. Bissessur, R.; Wagner, B. D.; Brüning, R. *J. Mater. Sci.* **2004**, *39*, 119

67. Joensen, P.; Crozier, E. D.; Alberding, N.; Frindt, R. F. *J. Phys. C: Solid State Phys.* **1987,** *20,* 4043.

68. Tsai, H.-L.; Heising, J.; Schindler, J. L.; Kannewurf, C. R.; Kanatzidis, M. G. *Chem. Mater.* **1997,** *9,* 879.

69. Wypych, F.; Schollhorn, R. *J. Chem. Soc, Chem. Commun.* **1992,** 1386.

70. *Annual Book of ASTM Standards* **1979**, *E-698*, 601.

71. Unpublished work at Dr. Rabin Bissessur's lab, UPEI.

72. Bissessur, R.; Kanatzidis, M. G.; Schindler, J. L.; Kannewurf, C. R. *J.Chem. Soc., Chemical Communications.* **1993**, *20,* 1582.

73. *Titan, wavefunction, Inc.; Schrödinger, Inc.* **1999.**

74. Shen, G.-M.; Chen, C.-C.; Tsiang, R. *Journal of Polymer Science, Part A, Polymer Chemistry,* **2001,** *39,* 2625.

75. Thatcher, J.-H.; Thanapprapasr, K.; Nagae, S,-I.; Mai, S.-M.; Booth, C.; Owen, J.-H. *J. Mater. Chem.* **1994,** *4,* 591.

76. Pan, G.-Q.; Li, H.-L.; Gao, Y. *Journal of Applied Polymer Science,* **2004,** *93,* 577.

77. Nekoomanesh, M.; Booth, C. *Iranian Journal of Polymer Science & Technology,* **1992,** *1,* 36.

78. Colley, R. A.; Mai, S.-M.; Booth, C.; Budd, P. M.; Balderson, S. *J. Mater. Chem.,* **1999,** *9,* 1661.

79. Papke, B. L.; Ratner, M. A.; Schriver, D. F. *J. Phys. Chem. Solids* **1981,** *42,* 493.

80. Wieczorek, D.; Raducha, D.; Zalewska, A.; Stevens, J. R. *J. Phys. Chem. B* **1998,** *102,* 8725.

81. Liu, D.-F.; Luo, R.; Nie, J.; Guan, W.-C. *Materials Science and Engineering B.* **2005,** *119,* 99.

82. Nicholas, C. V.; Wilson, D. J.; Booth, C. *British polymer journal,* **1988**, *20,* 289.

83. Poel, G. V.; Mathot, V. B. F. *Thermochimica Acta* **2007,** *461,* 107.

84. Allcock, H. R. Chang, Y.; Welna, D. T. *Solid State Ionics.* **2006,** *177,* 569.

85. Chen-Yang, Y. W., Hwang, J. J.; Huang, A. Y. *Macromolecules* **2000,** *33,* 1237.

86. Orme, C. J.; Klaehn, J. R.; Harrup, M. K.; Luther, T. A.; Peterson, E. S.; Stewart, F. F. *Journal of Membrane Science* **2006,** *280,* 175.

87. Nazri, G.; MacArthur, D. M.; Ogara, J. F. *Chemistry of Materials* **1989,** *1,* 370.

88. Chen, C. H.; Meester, B.; van der Put, P. J. J. M.; Schoonman, J. *Chem. Vap. Deposition* **1998**, *4,* No. 1

89. Nazar, L. F.; W, H.; Poewr, P. *J. Mater. Chem.* **1995,** *5,* 1985.

90. Allcock, H. R.; Ravikiran, R.; O'Connor, S. J. M. *Macromolecules* **1997**, *30,* 3184.

91. Krishnamoorti, R.; Vaia, R. A.; Giannelis, E. P. *Chem. Mater.* **1996,** *8,* 1728.

92. Hutchinson, J. C.; Bissessur, R.; Shriver, D. F. *Chem. Mater.* **1996,** 8, 1597.

93. Kappe, O.; Stadler, A. *Microwaves in Organic and Medicinal Chemistry, Wiley-VCH* **2005.**

94. White, W. *UPEI Chemistry Department, Honour's Thesis* **2004.**

95. Ghanbari, K.; Mousavi, M. F.; Shamsipur, M. *Electrochimica Acta* **2006,** *52,* 1514.

96. Yang, C.; Chen, C.; Zeng, Y. *Spectrochimica Acta Part A* **2007,** *66,* 37.

97. Lei, X.; Su, Z. *Materials Letters* **2007,** *61,* 1158.

98. Bissessur, R.; MacDonald, J. *Materials Chemistry and Physics* **2007,** *106,* 256.

99. Zima, V.; Benes, L.; Melanova, K. *Solid State Ionics* **1998,** *106,* 285.

100. Hibino, T. *Chem. Mater.* **2004,** *16,* 5482.